Influences of Surface Spectral Emissivity and Cloud Longwave Scattering on Climate Simulations

by

Yi-Hsuan Chen

A dissertation submitted in partial fulfillment
of the requirements for the degree of
Doctor of Philosophy
(Climate and Space Sciences and Engineering)
in The University of Michigan
2020

Doctoral Committee:

Associate Professor Xianglei Huang, Chair
Assistant Professor Ángel F. Adames-Corraliza
Associate Professor Mark G. Flanner
Professor Christopher J. Poulsen

Yi-Hsuan Chen

yihsuan@umich.edu

ORCID iD: 0000-0003-2018-8728

To my family, and everyone who has supported me along my research journey.

獻給我的家人，以及研究路上所有支持過我的人

ACKOWLEDGEMENTS

My PhD thesis is all about climate model simulations. Without the help of high-performance computing resources, this thesis would not be possible. I would like to acknowledge the computational resources and services provided by Advanced Research Computing at the University of Michigan, Ann Arbor, the high-performance computing support from Cheyenne (doi:10.5065/D6RX99HX) provided by NCAR's Computational and Information Systems Laboratory, sponsored by the National Science Foundation, and the National Energy Research Scientific Computing Center (NERSC), a U.S. Department of Energy Office of Science User Facility operated under Contract No. DE-AC02-05CH11231.

My PhD journey has a lot of ups and downs. I would say, the times of downs are much more than the times of ups. Finishing PhD is tough. As an international student, in addition to facing the challenges of research, dealing with the challenges of language, culture, and daily matters is not easy. Fortunately, I have plowed through all the challenges, completed my PhD thesis, and now I am writing the acknowledgment. Without the help of many people, I would not be able to complete my thesis and get to the final stage of my PhD journey.

I first would like to thank my adviser, Prof. Xianglei Huang. I first met him in Academia Sinica, Taiwan, when I was working as a research assistant. He visited there and knew I will apply for a PhD. He told me to send him an email when I submit my application, and he will take a look at my application materials. Fortunately, he gave me

an offer. I applied for 10+ PhD programs and only got this offer. Without him, I would not start my PhD journey. I am very grateful for him to give me this opportunity. During my PhD study, he has shown me the role models of a serious scientist, a dedicated teacher, and a supportive mentor. I am particularly grateful that he is willing to spend time on all his students and me, although he is super super busy. Since my first semester, we have had an individual meeting every week. Sometimes I feel guilty to occupy his time for my silly questions and slow research progress.

I would like to thank my committee members, Prof. Mark Flanner, Prof. Ángel F. Adames-Corraliza, and Prof. Chris Poulsen. Thanks for their time to review my research work and provide me invaluable feedback. Also, I would like to thank my collaborators, Prof. Ping Yang and Dr. Chia-Pang Kuo.

I would like to thank my research group members: Fang, Hongze, Lu, Zack, Colten, Chongxing, Yan, Xiuhong, and Xianwen. I would like to give a particular thank to Xiuhong, for her support on modifying the surface emissivity in climate models. Also, I would like to thank my friends in CLaSP, in the Taiwanese Student Organization, in the Mosaic Church, and at the UM. Without the companion of these awesome people, my PhD journey and life in Ann Arbor would be dry and boring.

I would like to thank the CLaSP staff and IT group. Without their help. I couldn't go anywhere.

I would like to thank the UM for providing considerable resources for students, like seminars, workshops, courses, social events, sports, concerts, you name it!

Last but not least, I would like to thank my parents, my sisters, and all my relatives. It is a privilege to born and grow up in a family that cares and supports

education. It is a privilege to have a healthy body to do almost whatever I want. It is a privilege to study abroad at the prestigious and wonderful UM. Many things I don't deserve; they are from generous and unconditional supports from others.

Yi-Hsuan Chen

陳毅軒

11/07/2019

TABLE OF CONTENTS

LIST OF FIGURES

LIST OF TABLES

ABSTRACT

Longwave (LW) radiation plays a critical role in the Earth's climate system. It carries energy from the Earth to space, thereby balancing the global-averaged net solar radiation at the top of the atmosphere. It also redistributes energy within the atmosphere, and between the atmosphere and the surface. Due to its importance, a correct and faithful representation of the LW radiation processes in climate models is crucial for understanding the climate system and projecting future climate. Because comprehensive LW radiation calculations are computationally expensive, many approximations are made to accelerate these calculations. Two common approximations are blackbody surface and non-scattering clouds. At least twenty years ago, researchers argued the validity of these approximations, but these arguments have received relatively little attention until recently.

This dissertation, along with other recent studies, investigates the impact of surface spectral emissivity and ice cloud LW scattering on simulated climate. Specifically, this dissertation implements surface spectral emissivity, a two/four-stream LW radiative transfer solver, and a state-of-the-art ice cloud LW optical scheme into the Community Earth System Model version 1.1.1 (CESM1.1.1) and the DoE Energy Exascale Earth System Model (E3SM). Using the modified version of the CESM1.1.1, this dissertation investigates:

(1) The surface emissivity effect over the Sahara and Sahel. The surface emissivity in these regions can be as low as 0.6-0.7 over the infrared window band while close to

unity in other bands, but such spectral dependence has been ignored in climate models. The inclusion of realistic surface emissivity over the Sahara and Sahel, compared to the blackbody surface, increases the surface air temperature over these regions and produces more convective rainfall, especially in the Sahara. The precipitation south of the Sahel is also increased, indicating that the changes of surface emissivity can influence the local climate and beyond.

(2) The ice cloud LW scattering effect on polar climate. Cloud LW scattering is usually neglected in climate models. The traditional rationale is that this scattering is negligible compared to strong LW absorption by clouds and greenhouse gases. This rationale, however, is not valid in the polar regions, in which the atmospheric absorption is weak due to the small amount of water vapor, implying that cloud LW scattering is not negligible anymore. Using CESM with a slab-ocean model, the scattering effect increases the Arctic (Antarctic) winter surface temperature by around 1.4K (1.4K). Interestingly, this effect becomes much weaker, only 0.1K (0.4K), when the sea surface temperatures and sea ice are prescribed. These results highlight the importance of the cloud LW scattering effect in the polar regions and the importance of surface-atmosphere coupling when this effect is considered.

(3) The combined effect of surface emissivity and ice cloud LW scattering on polar climate. When a non-blackbody surface is combined with scattering clouds, multiple scattering between the surface and clouds can occur and retain additional energy in the Earth. The CESM simulations show that these two effects are linearly additive in the polar regions.

This dissertation also shows that the modified E3SM, compared to the standard E3SM, reduces the prominent surface warm bias during the Arctic winter by half, mainly because of the new ice cloud optical scheme. The influences on other fields are minimal.

Altogether, this dissertation demonstrates the importance of surface spectral emissivity and cloud LW scattering on the simulated climate, particularly over the polar regions.

Chapter 1

Introduction

1.1 Longwave radiation treatments in climate models

Longwave (LW) radiation, also known as terrestrial radiation, usually refers to the electromagnetic radiation emitted from the Earth's surface and atmosphere. Because the earth-atmosphere system typically exhibits temperature in the range of 200-320K, the LW radiation mainly lies in the infrared (IR) portion of the electromagnetic spectrum. The LW radiation plays a major role in redistributing energy within the atmosphere and between the atmosphere and the Earth's surface. It also carries energy from the earth-atmosphere system to space, thereby balancing the solar radiation absorbed by the Earth and atmosphere over a sufficient long-term average. The LW radiation hence plays a crucial role in the Earth's climate system. A thorough understanding of the LW radiation processes is essential to understand and predict the Earth's climate.

General circulation models (GCMs), which represent physical processes in the atmosphere, ocean, land surface, and other components in the Earth's climate system, are essential tools for understanding the Earth's climate and making future climate projections. Because the LW radiation is of central importance in the Earth's climate system, all GCMs entail LW radiation schemes to represent relevant physical processes and calculate the exchange of LW radiation energy between the Earth's surface and the atmosphere, the LW radiative heating rate in the atmosphere, and the outgoing LW

radiation (OLR) at the top of the atmosphere (TOA). Virtually all LW radiation schemes consist of three parts: surface, atmosphere, and radiative transfer solver. The surface part determines the upward LW flux at the surface, which represents the amount of LW energy transferred from the surface to the atmosphere. The atmospheric part determines the LW optical properties of gasous species (water vapor, carbon dioxide, ozone, and other trace gases) and suspended particles in the atmosphere (aerosol and clouds). Then the surface upward LW flux and the atmospheric LW properties are fed to the radiative transfer solver to calculate the LW fluxes at all levels from the surface to the atmosphere, and the corresponding LW radiative heating rate at each level.

Because GCM simulations are computationally expensive, the LW radiation schemes usually make as many approximations as possible to accelerate the LW radiation calculations. For instance, gas species have millions of absorption lines across the LW spectrum. Instead of calculating the transmittance of each gasous species at every wavelength over the entire LW spectrum, which is extremely time-consuming, many LW schemes adopted correlated-k methods to calculate the band-averaged transmittance (e.g. Chou et al. 2001; Fu and Liou 1992; Mlawer et al. 1997). The surface is usually assumed as blackbody or graybody in the GCMs without considering the spectral variation of emissivity (Chen et al. 2014). Finally, because the scattering effects of aerosol and cloud particles are secondary compared to their absorption and emission effects, the LW radiative transfer solver usually neglects scattering, i.e. only considers the absorption and emission of these condensed particles.

Some of these approximations in the LW schemes are frequently validated but some are not. Absorption coefficients of gas molecules used in the correlated-k

methods are usually checked and, if needed, updated with the latest HITRAN database (Rothman et al. 1998; Gordon et al. 2017), which is arguably the most comprehensive compilation of spectroscopic parameters of gaseous media. The clear-sky radiation (i.e. gases only, no aerosols and clouds) calculated from the LW schemes is constantly compared with those from the line-by-line radiative transfer model, which is widely deemed as benchmark ground truth. The comparison usually shows excellent agreements, with flux difference within 1 Wm^{-2} in the entire atmosphere and heating rate differences within 0.1 K/day in the troposphere and 0.3 K/day in the stratosphere (e.g. Mlawer et al. 1997). As a result, clear-sky radiation calculation is usually deemed to be the most robust parameterization scheme in the GCMs (Held, 2005). In contrast, the approximations made in the surface and cloud LW properties receive little attention. The main theme of this dissertation is to examine the validity of these approximations in the coupled GCMs and to quantify the influences of these approximations on the simulated climate. Specifically, this dissertation examines two particular topics: surface spectral emissivity and ice cloud LW scattering, which will be further elaborated in the following sections.

1.2 Surface spectral emissivity

Every object emits radiation in all wavelengths. The radiance at a certain wavelength is determined by the temperature of the object and its emissivity, that is,

$$I_\lambda = \varepsilon_\lambda * B_\lambda(T) \quad (1.1)$$

where I_λ is the radiance, ε_λ is the emissivity, $B_\lambda(T)$ is Planck's function at the temperature T. The subscript λ denotes a specific wavelength. Eq (1.1) shows that the radiance is proportional to Planck's function and spectral emissivity, ε_λ. ε_λ depends on the object's intrinsic property and state (such as composition, surface wetness, etc.) and geometric settings (such as viewing angle, surface roughness, etc.). In most cases, if not all, ε_λ ranges from zero to unity. When ε_λ equals unity, the object acts as a blackbody at the wavelength λ.

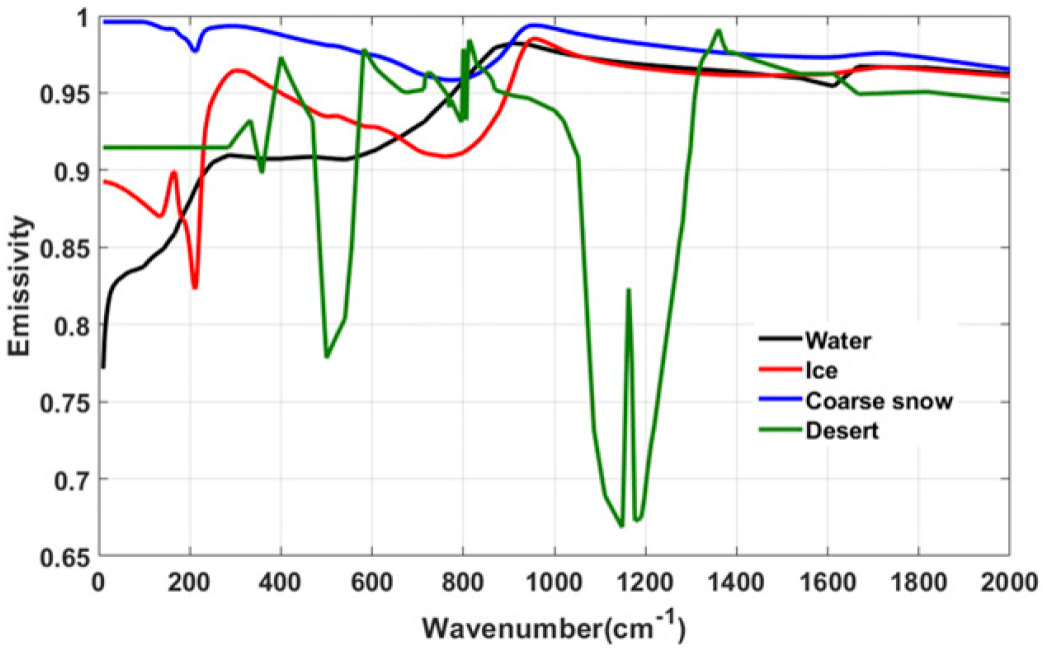

Fig. 1.1. The spectral emissivities of water, ice, coarse snow, and desert. This figure is adapted from Huang et al. (2018).

As far as surface emissivity is concerned, it is well known that the surface emissivity depends on surface type, wavelengths, and viewing angle (Baldridge et al. 2009; Z. Li et al. 2013; Huang et al. 2016). Figure 1.1 shows surface spectral emissivity at 53^o viewing zenith angle for water, ice, coarse snow, and desert, based on the dataset developed by Huang et al. (2016). It can be seen that desert emissivity is as low as 0.68 in the mid-infrared window band (800-1200 cm^{-1}) while near 0.95 in the mid-IR water vapor band (i.e. 1400-2000 cm^{-1}), whereas coarse snow emissivity is about 0.98 over the entire LW spectrum.

The surface spectral emissivity is a fundamental quantity in the calculation of surface upward LW flux at different wavelengths, that is, the amount of LW energy transferred from the surface to the atmosphere. The surface upward LW flux consists of two terms: surface emission and the reflection of the downward LW flux at the surface. Mathematically,

$$F_{\lambda,sfc}^{\uparrow} = \varepsilon_\lambda \pi B_\lambda(T) + (1-\varepsilon_\lambda) F_{\lambda,sfc}^{\downarrow} \quad (1.2)$$

where $F_{\lambda,sfc}^{\uparrow}$ is surface upward LW flux at wavelength λ, $F_{\lambda,sfc}^{\downarrow}$ is surface downward LW flux at λ, other symbols are as defined in Eq (1.1).

The surface spectral emissivity appears in both the surface emission term, $\varepsilon_\lambda \pi B_\lambda(T)$, and the reflection term, $(1-\varepsilon_\lambda) F_{\lambda,sfc}^{\downarrow}$. However, most GCMs do not take this spectral dependence of surface emissivity into account. Instead, all surface types are assumed to be blackbody or graybody in the LW radiation scheme (Chen et al. 2014). This assumption is reasonable in certain circumstances: for example, as long as $\pi B_\lambda(T)$ is comparable to $F_{\lambda,sfc}^{\downarrow}$, the exact value of ε_λ does not affect $F_{\lambda,sfc}^{\uparrow}$ because $\varepsilon_\lambda \pi B_\lambda(T) + (1-\varepsilon_\lambda) F_{\lambda,sfc}^{\downarrow} \approx \varepsilon_\lambda \pi B_\lambda(T) + (1-\varepsilon_\lambda) \pi B_\lambda(T) = \pi B_\lambda(T)$. In other words, for this case the

$F^{\uparrow}_{\lambda,sfc}$ is close to blackbody emission at the surface temperature, regardless of the value of ε_λ. These circumstances can occur in the far-IR band over the tropical ocean, where the abundant water vapor near the surface implies strong far-IR emission to the surface and the effective emission temperature is close to the ocean surface temperature, resulting in comparable magnitudes of the $F^{\downarrow}_{\lambda,sfc}$ and $\pi B_\lambda(T)$. In circumstances that $F^{\downarrow}_{\lambda,sfc}$ is not comparable to $\pi B_\lambda(T)$ and the surface cannot be well approximated as blackbody or graybody, realistic surface spectral emissivity must be taken into account otherwise the surface upward LW flux can be biased. These circumstances can occur in (1) the atmospheric window band (800-1200 cm^{-1}) over desert region, where desert emissivity can be as low as 0.68 (Fig 1.1) and the downward LW flux at the surface in this band can be much smaller than the surface emission because the atmosphere is relatively transparent in this band and clouds are infrequent over desert; (2) the far-IR band (0-600 cm^{-1}) over high-latitude regions, where the ice surface emissivity can be as low as 0.85 (Fig 1.1) and the atmosphere is cold and dry, resulting in a much less downward far-IR flux at the surface than the blackbody emission at the surface temperature; (3) the far-IR band over high-altitude regions such as Tibetan Plateau, where the atmosphere is also cold and dry and the ice surface is not uncommon.

Despite that the surface emissivity can affect surface upward LW flux and potentially simulated climate in the GCMs, only a few studies have investigated this issue (e.g. Zhou et al. 2003; 2007; 2008; Feldman et al. 2014; Huang et al. 2018; Wu et al. 2019). Given that GCMs usually set too large surface broadband emissivity values for bare soil compared to satellite retrievals (0.96 versus 0.83-0.96; Zhou et al. 2003; Ogawa et al. 2004), Zhou et al. (2003) carried out GCM sensitivity simulations that

varied surface emissivity from 0.84 to 0.96 over the Sahara and Arabian Peninsula, and then examined to what extent these changes of surface emissivity affect the simulated climate. They found that a decrease of soil emissivity by 0.1 would increase the ground temperature by about 1.1^{o}C. This is because the decrease in soil emissivity reduces the amount of surface emission, keeping more energy at the surface and consequently, increasing the ground temperature. Their subsequent studies (Zhou et al. 2007; 2008) further examined how the changes in surface emissivity affect diurnal temperature range in the Sahel. They found that a reduction in surface emissivity by 0.1 (equivalent to the surface type changed from vegetation to bare soil) would reduce the diurnal temperature range by 1K, which is mainly due to the increase in nighttime temperature through increased soil heating and through reduced surface emission.

A missing component in aforementioned studies is that they changed the desert surface broadband emissivity but did not consider the strong spectral dependence of desert emissivity, as shown in Fig. 1.1. Huang et al. (2018) incorporated treatments of surface spectral emissivity into a GCM and their simulation results showed that the surface temperature and precipitation over the Sahara and Sahel are sensitive to the surface spectral emissivity. Since Huang et al. (2018) focused on the high-latitude climate simulations, especially the interactive radiation coupling between the atmosphere and ocean in the polar regions, they did not explore in full depth the mechanisms of how the surface spectral emissivity affects the simulated climate over the Sahara and Sahel. Chapter 2 examines the impact of the inclusion of surface spectral emissivity over the Sahara and Sahel on the simulated regional climate, especially the surface temperature and precipitation.

1.3 Cloud longwave scattering

Cloud particles can interact with LW radiation via absorption, scattering, and emission. The relative importance of these interactions depends on the phase, size, and shape of cloud particles as well as LW radiation wavelength. For example, around 10 μm wavelength, a column ice crystal with maximum dimension of 15 μm has single scattering albedo of around 0.3 (Yang et al. 2013), in which absorption and emission are more important than scattering, whereas around 20 μm wavelength, the single-scattering albedo for the same ice crystal is about 0.8, in which scattering is more important. Generally speaking, as far as broadband LW radiation is concerned, absorption and emission are primary interactions between clouds and LW radiation while scattering is secondary, because the imaginary parts of the index of refraction for water and ice are sufficiently large over the majority of the infrared spectrum.

Clouds can alter the amount of LW energy received by the surface and the atmosphere. Compared to clear-sky conditions, the presence of clouds can reduce the OLR by absorbing LW radiation from the Earth's surface and from the atmosphere below the cloud layer, and emitting infrared radiation at normally colder cloud-top temperature with respect to the surface. Also, the presence of clouds can enhance the emission in the atmospheric window band (800-1200 cm^{-1}), increasing the downward broadband LW flux at the surface. Quantitatively, in terms of global-average, clouds decrease the OLR by 28 Wm^{-2} and increase surface downward LW flux by 28 Wm^{-2} (Wild et al. 2019). Cloud LW scattering effect is in line with the absorption and emission effects but the magnitude is much smaller. The cloud LW scattering effect has been estimated to reduce the global-averaged OLR by approximately 3 Wm^{-2} (Costsa and

Shine, 2006; Kuo et al. 2017) and increase the surface downward LW flux by 1.2 Wm^{-2} (Kuo et al. 2017).

Although cloud LW scattering in general is secondary compared to cloud absorption and emission, several studies have suggested that this scattering effect should be included in the LW radiation schemes in order to fully represent the interactions between clouds and LW radiation. To do so, some methods have been proposed while keeping computational efficiency, such as multiple-stream approximation (Toon et al. 1989; Edwards and Slingo 1996; Fu et al. 1997), cloud optical thickness scaling method (Chou et al. 1999), and perturbation method (J. Li and Fu 2000; J. Li 2002). Even though these methods have been proposed for more than 20 years, only a few out of dozens of GCMs have included the cloud LW scattering effect (Kuo et al. 2020), which might be due to lack of interests or concerns of computational cost.

Some recent studies have incorporated cloud LW scattering into the GCMs and investigated to what extent this scattering effect influences the simulated climate. Zhao et al. (2018) found that the inclusion of cloud LW scattering reduces annual global mean OLR by 2.6 Wm^{-2}, leading to a warmer atmosphere and changes in Hadley circulation. Consistent with the finding of Zhao et al. (2018), Wu et al. (2019) showed that the inclusion of cloud LW scattering strengthens the Hadley circulation and shifts the intertropical convergence zone (ITCZ) northward because of the increased temperature gradient toward the polar regions. Although these studies demonstrated that the cloud LW scattering effect can affect tropical climate, from the physical perspective, the scattering effect can be particularly important in the polar regions because (1) ice clouds

which have strong scattering capability frequently exist over the course of the year; (2) small water vapor amount in the polar regions allows the LW radiation scattered by clouds to reach the surface or the TOA without being absorbed by the atmosphere. Given that the ice cloud LW scattering effect can play a role in the LW radiation processes over the polar regions and this effect has not been well quantified, Chapter 3 describes the influence of ice cloud LW scattering on the simulated climate in the polar regions.

1.4 The combined effect of surface emissivity and cloud LW scattering

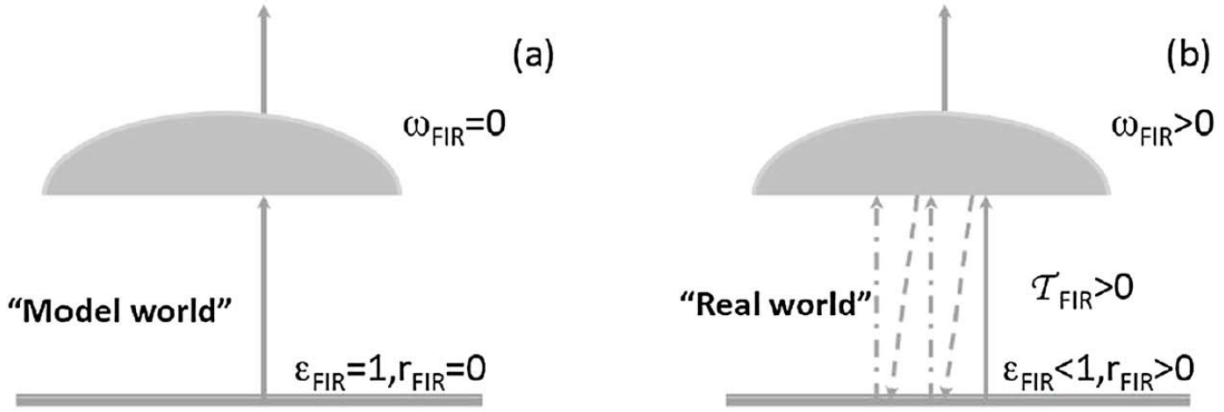

Fig. 1.2. (a) A schematic figure shows the blackbody surface and non-scattering clouds in the far-IR regions (denoted by subscript "FIR"), which are common assumptions in current GCMs. Upward arrow denotes far-IR photons emitted by the surface and transmitted through the cloud. $\mathcal{T}$ is transmittance, ω is the single-scattering albedo of cloud, ε is the surface emissivity, and r is the surface reflectivity. (b) A schematic figure shows that in reality, these far-IR photons can be reflected between cloud and surface multiple times and absorbed in the course of such scattering. This figure is adapted from Chen et al. (2014).

In the high-latitude regions, previous studies show that the inclusion of surface spectral emissivity in the GCMs leads to an increase the surface temperature by around 1 K (Feldman et al. 2014; Huang et al. 2018). Chapter 3 investigates the ice cloud LW scattering effect in these regions. The combined effect of surface emissivity and ice

cloud LW scattering is worth further studying. As sketched in Fig. 1.2, when the surface is not blackbody and clouds can scatter LW radiation, multiple reflection of LW radiation between the surface and clouds can occur and retain more energy in the Earth system than the case of blackbody surface and non-scattering clouds, i.e. no multiple reflection between the surface and clouds. Using offline radiative transfer model calculations over the Antarctic plateau, Chen et al. (2014) showed that the combined effect of surface emissivity and cloud LW scattering in the far-IR band can reduce the monthly-mean OLR by 0.72 to 1.47 Wm^{-2} in this band, with comparable contributions from each effect. This combined effect, to our best knowledge, has not been quantified in the high-latitude regions using climate model simulations. Chapter 4 intends to quantify this combined effect as well as the relative contribution of each effect.

1.5 Implementation of surface emissivity and cloud LW scattering into the Energy Exascale Earth System Model (E3SM)

Chapters 2 to 4 describe the implementation of surface spectral emissivity and ice cloud LW treatments into the CESM, and examine their impacts on climate simulations. To expand the scope and investigate the impacts of these treatments in other GCMs, Chapter 5 describes similar implementations in another state-of-the-art Earth system model, the Energy Exascale Earth System Model (E3SM), funded by the U.S Department of Energy. The E3SM particularly focuses on water cycle and cryosphere, of which the high-latitude regions play an important role. The implementation of surface spectral emissivity and ice cloud LW scattering can improve the representation of LW radiation processes in the high-latitude regions, potentially

addressing biases in the standard E3SM. Chapter 5 also discusses the impact of the surface emissivity and ice cloud treatments on the simulated climate in the E3SM.

References

Baldridge, A. M., S. J. Hook, C. I. Grove, and G. Rivera, 2009: The ASTER Spectral Library version 2.0. Remote Sens. Environ., 113, 711–715, https://doi.org/10.1016/j.rse.2008.11.007.

Charney, J., W. J. Quirk, S. Chow, and J. Kornfield, 1977: A Comparative Study of the Effects of Albedo Change on Drought in Semi–Arid Regions. J. Atmos. Sci., 34, 1366–1385, doi:10.1175/1520-0469(1977)034<1366:ACSOTE>2.0.CO;2.

Chen, X., X. L. Huang, and M. G. Flanner, 2014: Sensitivity of modeled far-IR radiation budgets in polar continents to treatments of snow surface and ice cloud radiative properties. Geophys. Res. Lett., 41, 6530–6537, doi:10.1002/2014GL061216.

Chou, M.-D., M. J. Suarez, X. Z. Liang, and M.M.-H. Yan, 2001: A thermal infrared radiation parameterization for atmospheric studies. NASA Tech. Rep. Series on Global Modeling and Data Assimilation, NASA/TM-2001-104606, Vol. 19, 56 pp.

Costa, S. M. S., and K. P. Shine, 2006: An estimate of the global impact of multiple scattering by clouds on outgoing long-wave radiation. Q. J. R. Meteorol. Soc., 132, 885–895, doi:10.1256/qj.05.169.

Edwards, J. M., and A. Slingo, 1996: Studies with a flexible new radiation code. I: Choosing a configuration for a large-scale model. Q. J. R. Meteorol. Soc., 122, 689–719, doi:10.1256/smsqj.53106.

Feldman, D. R., W. D. Collins, R. Pincus, X. Huang, and X. Chen, 2014: Far-infrared surface emissivity and climate. Proc. Natl. Acad. Sci. U. S. A., 111, 16297–16302, doi:10.1073/pnas.1413640111.

Fu, Q., and K. N. Liou, 1992: On the Correlated k -Distribution Method for Radiative Transfer in Nonhomogeneous Atmospheres. J. Atmos. Sci., 49, 2139–2156, doi:10.1175/1520-0469(1992)049<2139:OTCDMF>2.0.CO;2.

Fu, Q., K. N. Liou, M. C. Cribb, T. P. Charlock, and A. Grossman, 1997: Multiple Scattering Parameterization in Thermal Infrared Radiative Transfer. J. Atmos. Sci., 54, 2799–2812, doi:10.1175/1520-0469(1997)054<2799:MSPITI>2.0.CO;2.

Gordon, I. E., and Coauthors, 2017: The HITRAN2016 molecular spectroscopic database. J. Quant. Spectrosc. Radiat. Transf., 203, 3–69, doi:10.1016/j.jqsrt.2017.06.038.

Held, I. M., 2005: The gap between simulation and understanding in climate modeling. Bull. Am. Meteorol. Soc., 86, 1609–1614, doi:10.1175/BAMS-86-11-1609.
Huang, X. L., X. Chen, D. K. Zhou, and X. Liu, 2016: An Observationally Based Global Band-by-Band Surface Emissivity Dataset for Climate and Weather Simulations. J. Atmos. Sci., 73, 3541–3555, doi:10.1175/JAS-D-15-0355.1.

Huang, X. L., X. Chen, M. Flanner, P. Yang, D. R. Feldman, and C. Kuo, 2018: Improved Representation of Surface Spectral Emissivity in a Global Climate Model and Its Impact on Simulated Climate. J. Clim., 31, 3711–3727, doi:10.1175/JCLI-D-17-0125.1.

Kuo, C.-P., P. Yang, X. Huang, Y.-H. Chen, and G. Liu, 2020: Assessing the accuracy and efficiency of longwave radiative transfer models involving scattering effect with cloud optical property parameterizations. J. Quant. Spectrosc. Radiat. Transf., 240, 106683, doi:10.1016/j.jqsrt.2019.106683.

Li, J., 2002: Accounting for Unresolved Clouds in a 1D Infrared Radiative Transfer Model. Part I: Solution for Radiative Transfer, Including Cloud Scattering and Overlap. J. Atmos. Sci., 59, 3302–3320, doi:10.1175/1520-0469(2002)059<3302:afucia>2.0.co;2.

Li, J., and Q. Fu, 2000: Absorption approximation with scattering effect for infrared radiation. J. Atmos. Sci., 57, 2905–2914, doi:10.1175/1520-0469(2000)057<2905:AAWSEF>2.0.CO;2.

Li, Z. L., H. Wu, N. Wang, S. Qiu, J. A. Sobrino, Z. Wan, B. H. Tang, and G. Yan, 2013: Land surface emissivity retrieval from satellite data. Int. J. Remote Sens., 34, 3084–3127, doi:10.1080/01431161.2012.716540.

Mlawer, E. J., S. J. Taubman, P. D. Brown, M. J. Iacono, and S. a. Clough, 1997: Radiative transfer for inhomogeneous atmospheres: RRTM, a validated correlated-k model for the longwave. J. Geophys. Res. Atmos., 102, 16663–16682, doi:10.1029/97JD00237. http://doi.wiley.com/10.1029/97JD00237.

Rothman, L. S., and Coauthors, 1998: THE HITRAN MOLECULAR SPECTROSCOPIC DATABASE AND HAWKS (HITRAN ATMOSPHERIC WORKSTATION): 1996 EDITION. J. Quant. Spectrosc. Radiat. Transf., 60, 665–710, doi:10.1016/S0022-4073(98)00078-8.

Taylor, C. M., E. F. Lambin, N. Stephenne, R. J. Harding, and R. L. H. Essery, 2002: The Influence of Land Use Change on Climate in the Sahel. J. Clim., 15, 3615–3629, doi:10.1175/1520-0442(2002)015<3615:TIOLUC>2.0.CO;2.

Toon, O. B., C. P. McKay, T. P. Ackerman, and K. Santhanam, 1989: Rapid calculation of radiative heating rates and photodissociation rates in inhomogeneous multiple scattering atmospheres. J. Geophys. Res., 94, 287–301, doi:10.1029/JD094iD13p16287.

Wild, M., M. Z. Hakuba, D. Folini, P. Dörig-Ott, C. Schär, S. Kato, and C. N. Long, 2019: The cloud-free global energy balance and inferred cloud radiative effects: an assessment based on direct observations and climate models. Clim. Dyn., 52, 4787–4812, doi:10.1007/s00382-018-4413-y.

Yang, P., L. Bi, B. a. Baum, K.-N. Liou, G. W. Kattawar, M. I. Mishchenko, and B. Cole, 2013: Spectrally Consistent Scattering, Absorption, and Polarization Properties of Atmospheric Ice Crystals at Wavelengths from 0.2 to 100 μ m. J. Atmos. Sci., 70, 330–347, doi:10.1175/JAS-D-12-039.1.

Wu, K., J. Li, J. Cole, X. Huang, K. von Salzen, and F. Zhang, 2019: Accounting for Several Infrared Radiation Processes in Climate Models. J. Clim., 32, 4601–4620, doi:10.1175/JCLI-D-18-0648.1.

Zhao, W., Y. Peng, B. Wang, and J. Li, 2018: Cloud longwave scattering effect and its impact on climate simulation. Atmosphere (Basel)., 9, 1–20, doi:10.3390/atmos9040153.

Zhou, L., R. E. Dickinson, Y. Tian, M. Jin, K. Ogawa, H. Yu, and T. Schmugge, 2003: A sensitivity study of climate and energy balance simulations with use of satellite-derived emissivity data over Northern Africa and the Arabian Peninsula. J. Geophys. Res. Atmos., 108, n/a-n/a, doi:10.1029/2003JD004083.

Zhou, L., R. E. Dickinson, Y. Tian, R. S. Vose, and Y. Dai, 2007: Impact of vegetation removal and soil aridation on diurnal temperature range in a semiarid region: Application to the Sahel. Proc. Natl. Acad. Sci., 104, 17937–17942, doi:10.1073/pnas.0700290104.

Zhou, L., R. Dickinson, P. Dirmeyer, H. Chen, Y. Dai, and Y. Tian, 2008: Asymmetric response of maximum and minimum temperatures to soil emissivity change over the Northern African Sahel in a GCM. Geophys. Res. Lett., 35, 1–6, doi:10.1029/2007GL032953.

Chapter 2

The Effects of Surface Longwave Spectral Emissivity on Atmospheric Circulation and Convection over the Sahara and Sahel

The material of this chapter was published in

Chen, Y.-H., X. L. Huang, X. H. Chen, and M. Flanner, 2019: The Effects of Surface Longwave Spectral Emissivity on Atmospheric Circulation and Convection over the Sahara and Sahel. *J. Clim.*, **32**, 4873-4890.

2.1 Introduction

Africa is the world's second most populous continent and one of the most vulnerable continents with regard to climate change. The Fifth Assessment Report of the Intergovernmental Panel on Climate Change (IPCC AR5) suggests that by the end of the twenty-first century, the mean annual surface temperature of Africa is likely to rise over 28^{o}C and precipitation patterns are likely to change too (IPCC 2013; Sylla et al. 2016; Monerie et al. 2017). These changes can have profound socioeconomic impacts, especially for the Sahara and Sahel. In the late twentieth century a sustained Sahel drought severely affected ecosystem services, in the form of declines in forest area and food production (Epule et al. 2014). In terms of future precipitation changes in the Sahara and Sahel, the magnitude and even the sign of these changes remain uncertain (Druyan 2011; Sylla et al. 2016; Monerie et al. 2017).

The climate research community has invested considerable efforts in the last two decades to understand the physical mechanisms that can affect climate variations in the Sahara and Sahel and the surrounding regions. Previous studies suggest that a number of factors can affect the weather and climate in the Sahara and Sahel, such as decadal to multidecadal variability of sea surface temperatures in different ocean basins (Giannini et al. 2003; Mohino et al. 2011; Fontaine et al. 2011; Rodríguez-Fonseca et al. 2015), aerosol and its indirect effects on clouds (Rotstayn and Lohmann 2002; Huang et al. 2019), increases of greenhouse gases (Held et al. 2005; Biasutti 2013, and references therein), Arctic sea ice variability (Smith et al. 2017; Monerie et al. 2019), and surface type changes (Charney et al. 1977). The first and second West African Monsoon Modeling and Evaluation Project Experiment (WAMME I and WAMME II; Xue et al. 2010; Xue et al. 2016) used multimodel experiments to assess the contributions of different factors to the climatology of West African monsoon as well as the Sahel drought. The WAMME II ensemble model results demonstrated that SST forcing is a major contributor to the Sahel drought, but the impact of land use and land cover change on the Sahel drought is also of first-order magnitude. As shown by Charney et al. (1977) and other subsequent studies (Sud and Fennessy 1982; Xue and Shukla 1993; Taylor et al. 2002), desertification can increase surface albedo, which causes the surface to absorb less solar energy and leads to a decrease in surface temperature and in sensible heat flux. These changes would then weaken convective activities and decrease convective rainfall, thus constituting a positive feedback mechanism. In all previous studies, the role played by the surface longwave (LW) spectral emissivity has been entirely ignored. Surface emissivity can vary with surface type and spectral

wavelengths, as shown in Fig. 2.1a, which presents surface spectral emissivity for desert, grass, and deciduous forest, based on the dataset developed in Huang et al. (2016). This suggests that changes of surface type can indeed change the surface spectral emissivity. From this perspective, the changes in surface emissivity can potentially alter surface energy processes and affect regional atmospheric circulation, in a manner similar to the changes in surface albedo depicted in Charney et al. (1977).

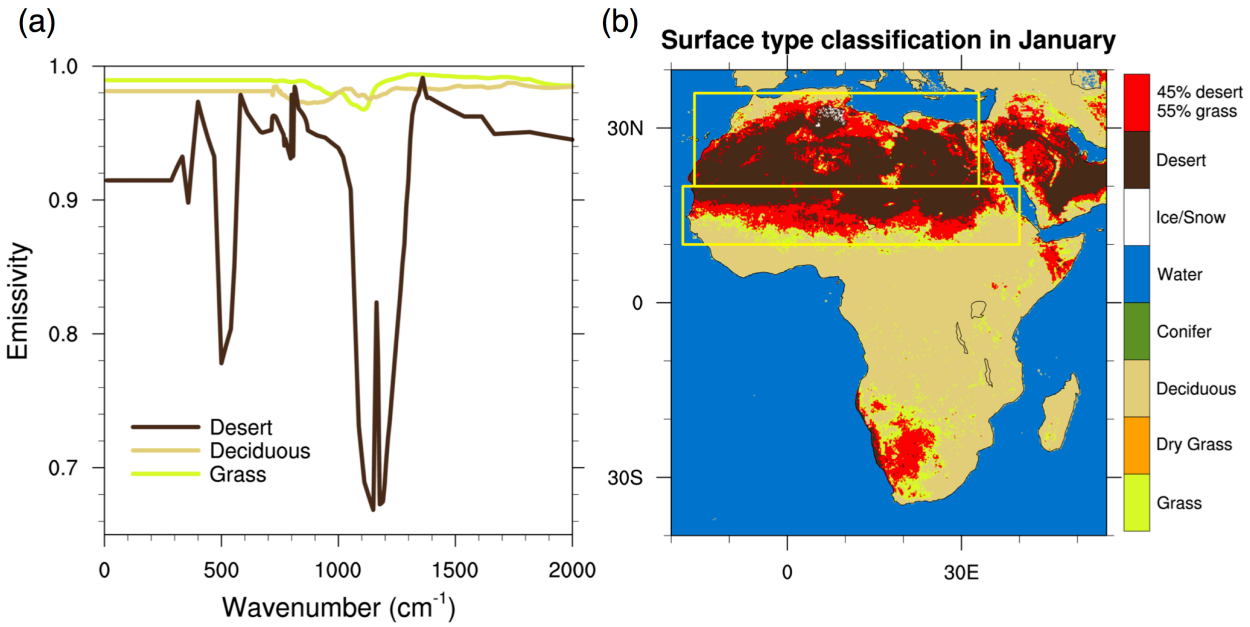

Fig. 2.1. (a) The LW spectral emissivity of desert (black), deciduous forest (light brown), and grass (light green) from 10 to 2000 cm^{-1} with a 1 cm^{-1} spectral resolution. Further details of such surface spectral emissivity can be found in Huang et al. (2016). (b) The surface type classification of Africa in January is based on Huang et al. (2016). The upper rectangle defines the Sahara in this study (20°–36°N, 16°W–33°E) and the lower rectangle defines the Sahel (10°–20°N, 18°W–40°E).

Figure 2.1a also shows that, while both grass and deciduous forest can be well approximated as a graybody with an emissivity about 0.98 over the entire LW spectrum, desert surface emissivity exhibits a strong spectral dependence. Desert emissivity can be as low as 0.7 in the mid-infrared window band, a band featured with little gaseous absorption and emission in the atmosphere. However, most general circulation models (GCMs) do not take this spectral dependence of surface emissivity into account and,

instead, assume that all surface types are blackbody in the radiation scheme used in the atmospheric module (Chen et al. 2014). Surface upward LW flux is the lower boundary condition for solving the LW radiative transfer in the atmosphere. Given the nature of gaseous absorption and emission, the LW radiative transfer in the atmosphere is highly spectrally dependent. Therefore, the lower boundary condition must include an accurate spectral partitioning of the broadband upward LW flux. Otherwise, the entire atmospheric LW radiative transfer solution begins from an incorrect boundary condition. Such need of correct spectral partitioning of the broadband upward LW flux at the surface warrants the inclusion of spectrally resolved surface emissivity in the radiation scheme of the GCMs. Since the desert has such strong spectral dependence in surface emissivity and is the dominant surface type in the Sahara and Sahel (Fig. 2.1b), this blackbody assumption in GCMs needs to be re-examined.

Using a realistic surface spectral emissivity dataset and the atmospheric profiles from the ECMWF ERA-Interim reanalysis (Dee et al. 2011), Huang et al. (2016) estimated that such emissivity difference with respect to the blackbody surface assumption can reduce the outgoing long- wave radiation (OLR) by as much as 10 W m^{-2} in the Sahara and Sahel. The influence of surface emissivity on climate model simulation was further assessed in Huang et al. (2018), in which they incorporated treatments of surface spectral emissivity into the Community Earth System Model (CESM). Their simulations showed that, compared to the standard CESM simulation, the inclusion of surface spectral emissivity can significantly affect the climatology of high-latitude surface temperature and sea ice fraction. They also showed that the simulated surface temperature and precipitation over the Sahara and Sahel is sensitive

to the surface spectral emissivity. Since Huang et al. (2018) focused on the high-latitude climate simulation, especially the interactive radiation coupling between the atmosphere and ocean in the polar regions, they did not explore in full depth the mechanisms of how the surface spectral emissivity affects the simulated climate over the Sahara and Sahel. This study is to particularly examine the impact of the inclusion of surface spectral emissivity over the Sahara and Sahel on the simulated regional climate, especially the surface temperature and precipitation.

The remainder of this paper is organized as follows. Section 2 describes the modified version of CESM used in this study and the design of simulation experiments. Section 3 presents the numeric results and physical interpretations. Conclusions and further discussions are then given in section 4.

2.2 Method and simulation experiment design

2.2.1 The modified version of CESM with the treatments of surface spectral emissivity

Surface spectral emissivity used in this study is taken from Huang et al. (2016), in which a hybrid approach was used to develop a global surface emissivity dataset suitable for the use in weather and climate models. Because few measurements of surface emissivity are available in the far-IR, Huang et al. (2016) employed first-principle calculations to compute the surface spectral emissivities over the entire LW spectrum for several surface types, such as water, ice, and sand with assumed shapes and sizes. Because of the diversity of vegetation types and the practical difficulty measuring index of refraction of each type of vegetation, the surface spectral emissivity

of vegetation was taken from Advanced Spaceborne Thermal Emission and Reflection Radiometer (ASTER) Spectral Library version 2.0 (Wilber et al. 1999; Baldridge et al. 2009), namely grass, dry grass, conifer forest, and deciduous forest. Since the ASTER only measured mid-IR emissivity, the far-IR emissivities of these vegetation types were assumed to be constant and equal to the measured emissivities at the longest mid-IR wavelength, that is, 14 μm (714 cm^{-1}). In total 11 surface types were defined in Huang et al. (2016). The spectral emissivities of these 11 surface types were then regressed against the Moderate Resolution Imaging Spectroradiometer (MODIS) retrieved surface mid-IR emissivity at eight discrete spectral points to determine the surface type and corresponding surface spectral emissivity at every 0.05° × 0.05° grid. Then the surface spectral emissivity was averaged onto 0.5° × 0.5° grids and validated against the mid-IR surface spectral emissivity retrievals from the Infrared Atmospheric Sounding Interferometer (IASI; Zhou et al. 2011). As shown in Huang et al. (2016), the spectral emissivity dataset had a good agreement with the IASI mid-IR retrievals. The root-mean-square difference of band-averaged emissivity over the entire globe was ~0.01. The largest differences were ~±0.05, occurring over deserts and plateau areas where complicated desert compositions or plateau topography hindered a good agreement between the IASI retrievals and the dataset developed in Huang et al. (2016). More details about the validation of the emissivity dataset can be found in Huang et al. (2016).

Huang et al. (2018) incorporated the aforementioned surface spectral emissivity dataset into the CESM version 1.1.1 (Hurrell et al. 2013). The surface spectral emissivity was averaged onto the bandwidths used by the LW radiation scheme in

CESM 1.1.1, the RRTMG_LW (Mlawer et al. 1997), and the band-by-band surface emissivity was then used in the atmospheric radiative transfer calculation. Note that the broadband upward LW flux at the surface ($F_{sfc}^{\uparrow}$) in the atmospheric model is provided from the surface models of CESM. These surface models assume the surface to be either a blackbody or a graybody with no spectral dependence, and calculate $F_{sfc}^{\uparrow}$ under such assumption. However, surface is always assumed to be blackbody in the atmospheric model of the standard CESM. To ensure the conservation of energy between the atmospheric and surface models, the CESM defines surface radiative skin temperature as $T_{skin} = \left(F_{sfc}^{\uparrow}/\sigma\right)^{1/4}$ where σ is the Stefan-Boltzmann constant, and uses T_{skin} with blackbody assumption in the RRTMG_LW. Huang et al. (2018) incorporated surface spectral emissivity into the RRTMG_LW but not into any surface models in the CESM. To ensure the consistency of $F_{sfc}^{\uparrow}$ across the different model components, T_{skin} was redefined as

$$F_{sfc}^{\uparrow} = \sum_i F_i^{\uparrow} = \sum_i \varepsilon_i \, \pi \int_{\Delta v_i} B_v \, (T_{skin}) dv + \sum_i (1 - \varepsilon_i) \, F_{i\_sfc}^{\downarrow} \qquad (1)$$

where $B_v(T_{skin})$ is Planck's function at the temperature of T_{skin}, Δv_i is the bandwidth of the *i-th* band in the RRTMG_LW, ε_i is the band-averaged surface emissivity of the *i-th* band, $F_i^{\uparrow}$ is the surface upward flux of the *i–th* band, and $F_{i\_sfc}^{\downarrow}$ is the downward flux of the *i-th* band at the surface as computed by the RRTMG_LW. The physical interpretation of Eq (1) is that both surface emission ($\sum_i \varepsilon_i \, \pi \int_{\Delta v_i} B_v \, (T_{skin}) dv$) and reflection of downward flux at the surface ($\sum_i (1 - \varepsilon_i) \, F_{i\_sfc}^{\downarrow}$) contribute to $F_{sfc}^{\uparrow}$. This interpretation will be used later for explaining the simulation results. Eq (1) was solved iteratively for T_{skin}. In other words,

compared to the standard CESM, such modification redistributed the broadband $F_{sfc}^{\uparrow}$ computed by the surface models into the RRTMG_LW spectral bands according to Eq (1), which adopted more realistic surface spectral emissivity than the blackbody assumption used in the atmospheric model of the standard CESM. This study adopts the same modified version of CESM as in Huang et al. (2018). Further details about this modification and its verification can be found in Huang et al. (2018).

2.2.2 Simulation experiment designs

Since the focus here is to study the impact of surface spectral emissivity in the Sahara and Sahel on the simulated climate, we carry out two sets of parallel CESM simulations. The first set uses the standard CESM (i.e., assuming blackbody surface everywhere in the atmospheric model) and is termed the "CTL" run. The other set uses the modified version of CESM and is termed the "NEW" run. The NEW run assumes blackbody everywhere except for the Sahara (20°–36°N, 16°W–33°E) and the Sahel (10°–20°N, 18°W–40°E), where the surface emissivities of each calendar month are prescribed according to the dataset developed by Huang et al. (2016). Thus, the only difference between the CTL and NEW runs is the surface emissivity specifications over the Sahara and Sahel. Figure 2.2 shows band-averaged surface emissivity in four RRTMG_LW bands for January. Similar patterns are seen in the surface emissivity maps of other calendar months as well (not shown here). Consistent with what is shown in Fig. 2.1, surface emissivity in the Sahara and Sahel over the band of 1080–1180 cm^{-1} is significantly lower than unity and can be as low as 0.6 (Fig. 2.2c).

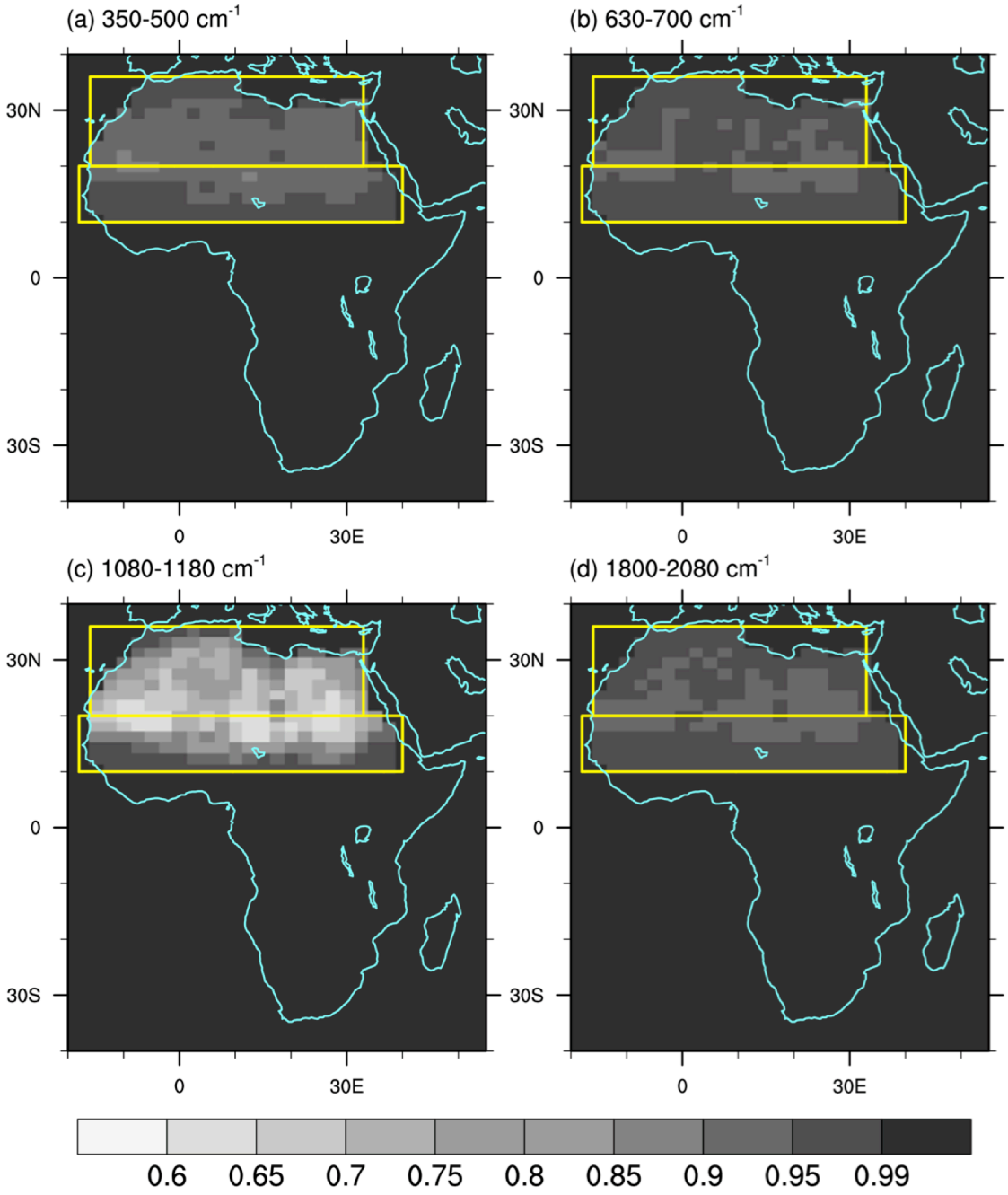

Fig. 2.2. Surface emissivity in the Sahara and Sahel for four RRTMG_LW bands: (a) 350–500 cm^{-1} (a band in the far IR); (b) 630–700 cm^{-1} (a band in the center of the CO_2 mid-IR band); (c) 1080–1180 cm^{-1} (a mid-IR window band); and (d) 1800–2080 cm^{-1} (a band in the tail of the H_2O 6.3-μm band). January results are shown here. Other months have similar surface emissivity features in the Sahara and Sahel. The two yellow rectangles define the Sahara and Sahel, respectively. The emissivity data are based on Huang et al. (2016).

Both CTL and NEW simulations are carried out using CESM 1.1.1. These simulations use the “F_2000” component set, in which the Community Atmosphere Model (CAM) is coupled with the Community Land Model (CLM) while sea surface temperatures and sea ice extent are prescribed with climatological monthly values (Hurrell et al. 2008). The vegetation area and density are also prescribed in the CLM with monthly values at the year of 2000. Trace gases and aerosols in the atmosphere are prescribed at the level of year 2000. Solar forcing is also prescribed without year-to-year variation. Both CTL and NEW simulations are carried out for 35 years and the output from the last 30 years is used in the following analysis. The horizontal resolution of these simulations is 1.9° latitude by 2.5° longitude and the number of vertical levels in CAM is 26.

2.3 Results and discussion

Simulated climate over the Sahara and Sahel will be discussed first, followed by the simulated regional climate beyond the Sahara and Sahel.

2.3.1 The Sahara and Sahel

2.3.1.1 Differences in surface energy budget and near-surface meteorological variables

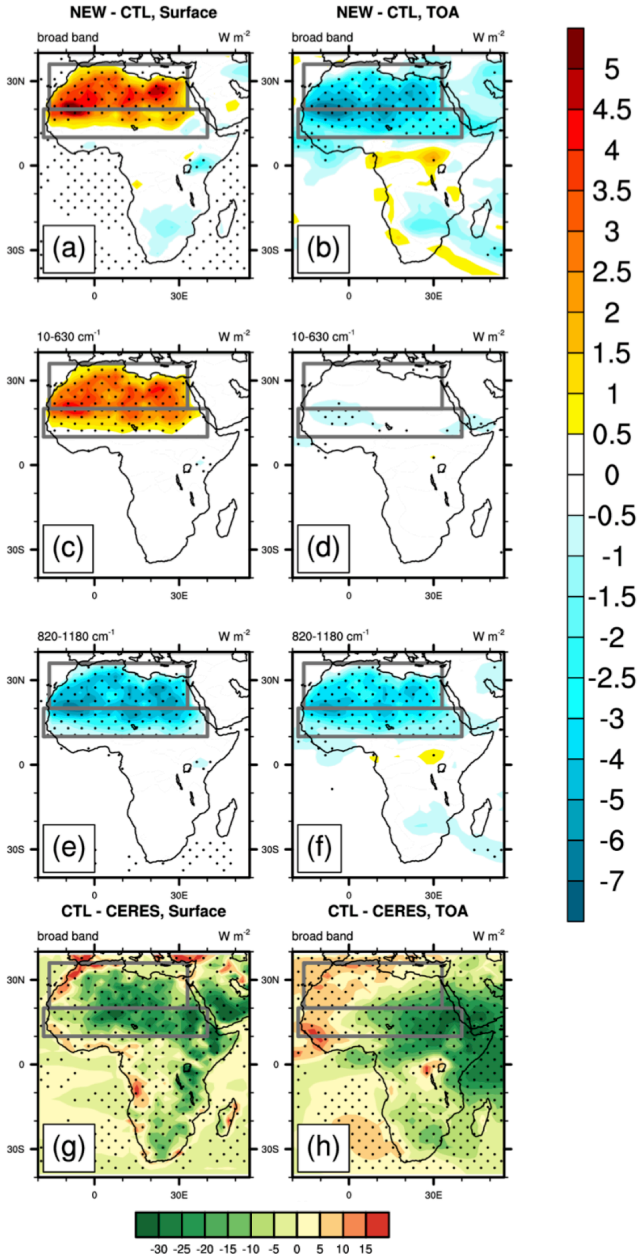

Fig. 2.3. (a),(b) The upward LW broadband flux differences between the NEW and CTL runs at the surface and at the TOA, respectively. (c),(d) As in (a),(b), but for the far IR (10–630 cm^{-1}). (e),(f) As in (a),(b), but for the window band (820–1180 cm^{-1}). Dotted area indicates that the differences pass the Student's *t* test with a 5% significance level. The two gray rectangles define the Sahara and Sahel. (g),(h) The upward LW broadband flux differences between the CTL run and the CERES climatology at the surface and at the TOA, respectively.

The top three rows of Fig. 2.3 show the 30-yr mean differences between the NEW and CTL runs in the upward LW flux at the surface (Figs. 2.3a,c,e) and at the TOA (i.e., OLR; Figs. 2.3b,d,f). The statistics are also summarized in Table 2.1. The surface upward LW broadband flux from the NEW run is larger than that from the CTL run over all Sahara grids and a dominant part of the Sahel (Fig. 2.3a). For the broadband OLR, however, the NEW run simulates a smaller OLR over all grids in the Sahara and Sahel than that from the CTL run (Fig. 2.3b). The different responses between the surface upward flux and the OLR can be understood as the LW broadband flux is decomposed to each RRTMG_LW band. From Fig. 2.3c, it becomes clear that the increase of surface upward LW flux from the CTL run to the NEW run originates from the far-IR H_2O rotational band (~10–630 cm^{-1}) as well as H_2O v2 band (~1300–1900 cm^{-1}; not shown). The contribution from the H_2O v2 band is much smaller than that from the far-IR band because the total flux of the H_2O v2 band is smaller than the far-IR band by several factors. Such changes of surface upward flux in these bands, however, have little impact on the OLR due to strong absorption and emission of H_2O in the atmosphere, as shown in Fig. 2.3d. In contrast, over the mid-IR window band (in the RRTMG_LW bandwidth, 820–1180 cm^{-1}), a decrease in the surface upward flux from the CTL run to the NEW run is seen and such decrease is also seen at the TOA (Figs. 2.3e,f). This is because atmospheric absorption is limited in the window band. Figure 2.3 clearly shows that the decrease of the broadband OLR in the NEW run is a result of the reduced outgoing longwave flux in the window band, with little contributions from other spectral bands.

The contrast between the far-IR and window bands in the surface upward flux shown in Fig. 2.3c and 2.3e can be understood in terms of surface emission and reflection of downward flux: these two terms consist of surface upward LW flux and are shown at the far right side of Eq (1). The band-averaged surface emission in the *i-th* band is determined by surface temperature and surface emissivity ε_i, and the reflection flux is determined by the downward LW flux at the surface and the reflectivity, which is (1-ε_i). Over the Sahara and Sahel, the ε_i of the window band in the NEW run is much lower than that in the CTL run (Fig. 2.2c). As a result, even though the near-surface temperature increases from the CTL run to the NEW run (Fig. 2.4 and to be discussed later), the smaller ε_i in the NEW run reduces surface emission in the window band compared to the CTL run. Such reduction cannot be compensated by the increase in the reflection of downward flux, because (1) the clear-sky atmosphere has little absorption and emission over the window band and (2) the cloud occurrence is also limited over the Sahara and Sahel. These two facts result in a relatively small downward flux in the window band from the atmosphere. As a result, from the CTL run to the NEW run, the decrease in surface emission dominates over the increase in surface reflection and leads to a decrease in the total surface upward flux in the window band (Fig. 2.3e). In contrast, although the ε_i of the far-IR band in the NEW run is smaller than that in the CTL run (Fig. 2.2a) and also leads to a reduction in surface emission in this band, such reduction is largely compensated by the increase of reflected downward flux. This is because water vapor has strong emission and absorption in the far-IR band, the downward flux at surface $F_{i\_sfc}^{\downarrow}$ is nearly as large as the surface blackbody emission in the same band (i.e. $\pi \int_{\Delta v_i} B_v\,(T_{skin}) dv$ in Eq. 1). As a result, the increase in surface

temperature dominates over the changes in surface emissivity and leads to an increase in surface upward flux in the far-IR band (Fig. 2.3c). These changes of surface upward LW flux in the far-IR and window bands affect the OLR differently. The changes in the surface upward LW flux in the far-IR band have little effect on the OLR because of the strong atmospheric absorption and emission (Fig. 2.3d), while the changes in the window band largely influence the OLR because of weak atmospheric absorption and emission (Fig. 2.3f). Therefore, the reduction of surface upward flux in window band dominates, leading to a decrease in the broadband OLR (Fig. 2.3b). Figure 2.3 also indicates that, if a climate model does not take surface spectral emissivity over the Sahara and Sahel into account, its OLR will have an incorrect band-by-band partitioning with excessive flux from the window band.

Figures 2.3g and 2.3h show differences in TOA and surface LW flux climatology between the CTL run and observations from CERES-EBAF edition 4.0 (Clouds and the Earth's Radiant Energy System–Energy Balanced and Filled; Loeb et al. 2018, Kato et al. 2018). Compared to the CERES surface upward LW flux, the CTL run has large negative biases over the vast majority of the Sahara and Sahel. The inclusion of surface spectral emissivity in the NEW run thus can partially help reduce such biases. As for the OLR, the CTL run has positive (negative) bias in the western (eastern) part of the Sahara and Sahel. Therefore, the inclusion of surface spectral emissivity reduces the positive bias in the west part of the Sahara and Sahel but increases the negative bias in the east part of it.

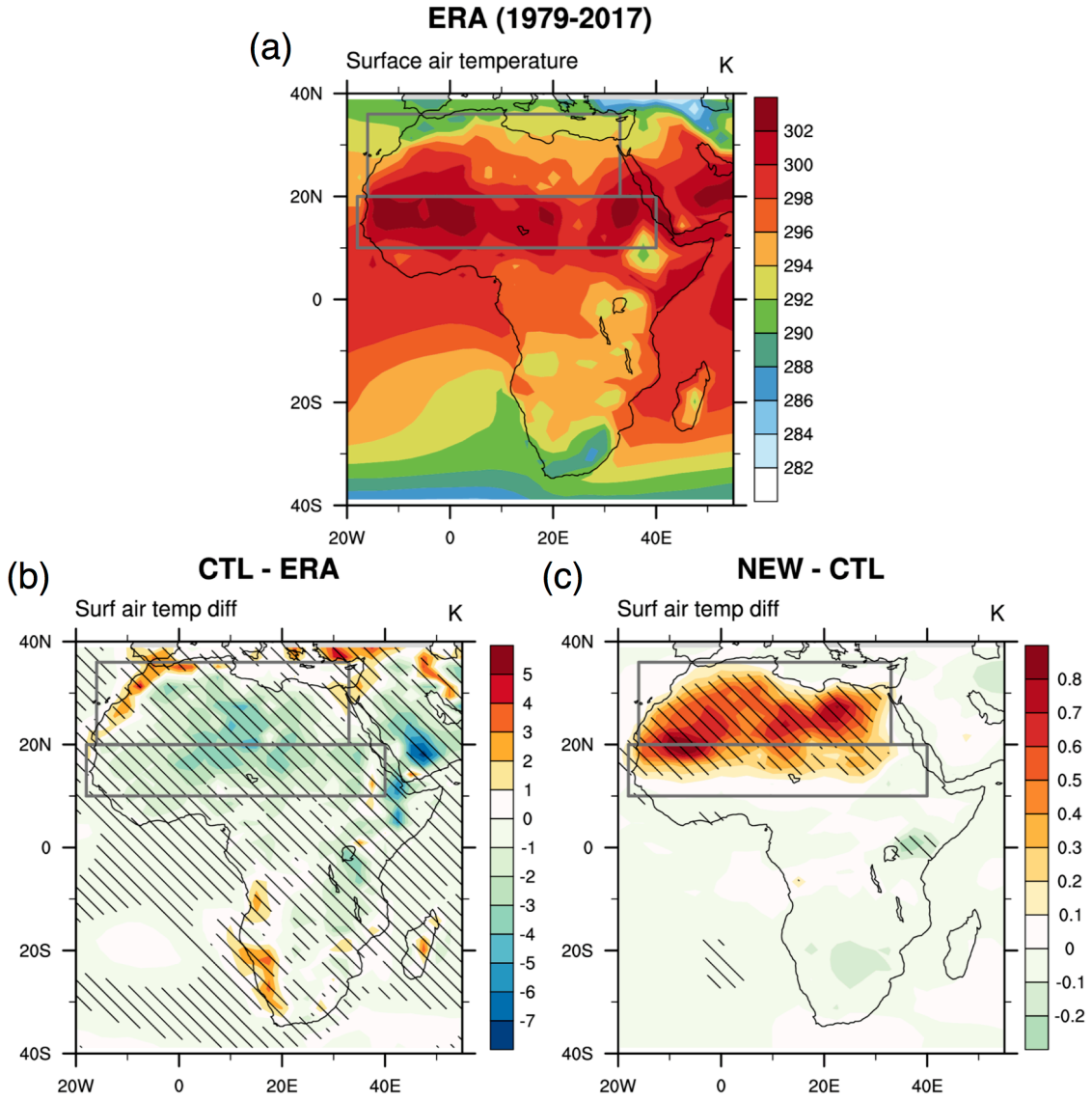

Fig. 2.4. (a) The long-term mean surface air temperature (SAT) based on ERA-Interim reanalysis from 1979 to 2017. (b) The climatological mean difference of SAT between the CTL run and ERA-Interim. (c) The climatological mean difference of SAT between the NEW and CTL runs. The slashed area indicates that differences pass the Student's *t* test at 5% significance level. The two gray rectangles define the Sahara and Sahel.

Figure 2.4 shows surface air temperature (SAT) climatology from the ECMWF ERA-Interim reanalysis, the difference between the CTL run and ERA-Interim, and the difference between the NEW and CTL runs. The CTL run has colder SAT than ERA-Interim over the vast majority of the Sahara and Sahel, which is consistent with negative

biases in the surface upward LW flux shown in Fig. 2.3g. The SAT in the NEW run is higher than that in the CTL run by up to 0.8 K in the Sahara and Sahel, and such difference is statistically significant for the majority of the grid points (Fig. 2.4c). This shows that the inclusion of surface spectral emissivity helps reduce the cold biases of the simulated SAT in the standard CESM.

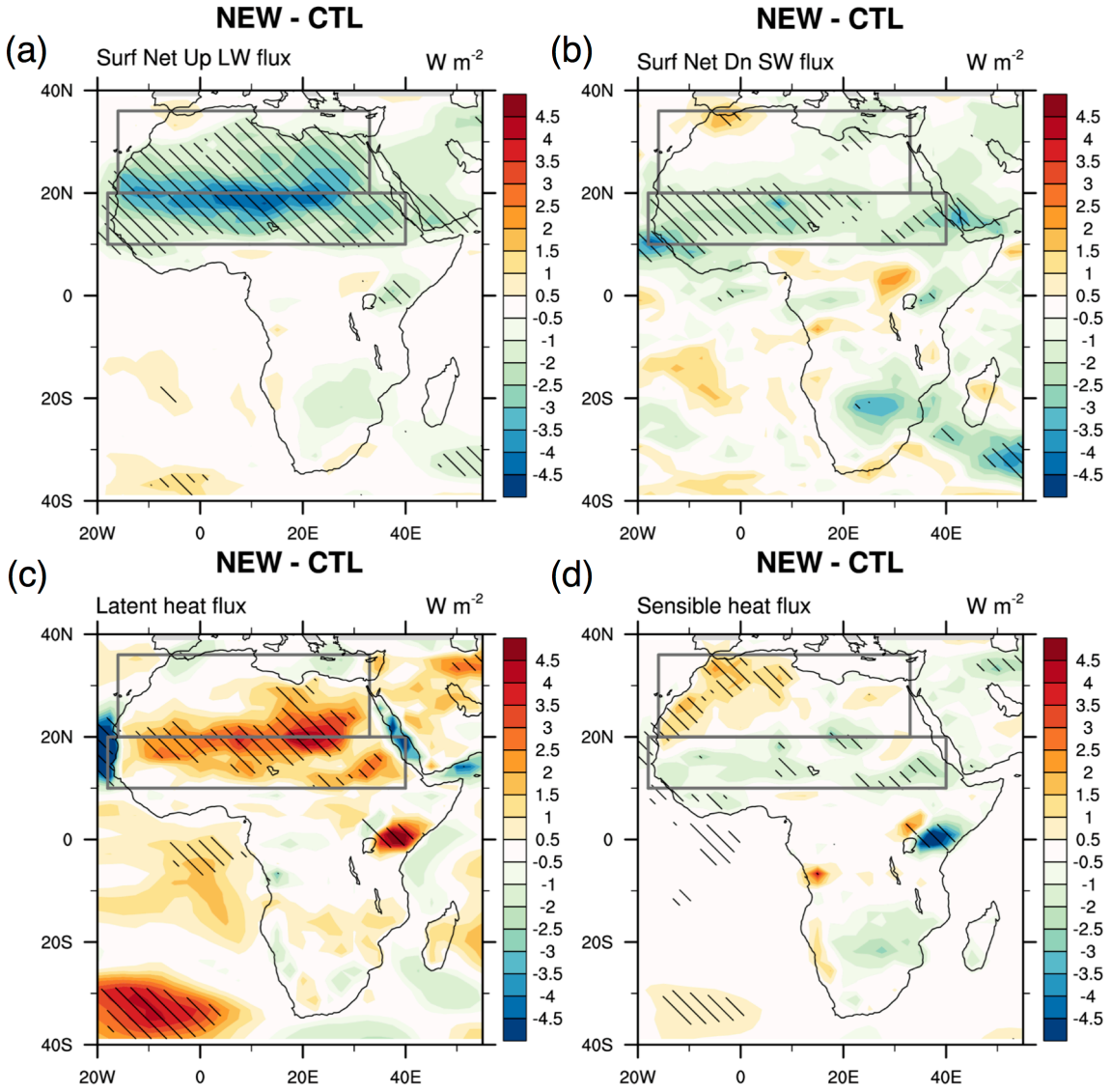

Fig. 2.5. Differences in surface energy budgets between the NEW and CTL runs. (a) Surface net LW flux (upward positive). (b) Surface net SW flux (downward positive). (c) Latent heat flux. (d) Sensible heat flux. The latent heat and sensible heat fluxes are defined as positive out of the surface. All results are based on 30-yr climatologies and slash area indicates 5% significance level. The two gray rectangles define the Sahara and Sahel.

The NEW–CTL differences in surface energy budget terms are shown in Fig. 2.5. Four terms in surface energy budget are examined here, namely net upward LW flux, net downward shortwave (SW) flux, latent heat flux, and sensible heat flux (defined as positive upward). Although the NEW run has a larger surface upward LW flux over the Sahara and Sahel than the CTL run (Fig. 2.3a), the net upward LW flux decreases in the NEW run from the CTL run (Fig. 2.5a). This suggests that the downward LW flux increases in the NEW run and such increases outweigh the increase of surface upward LW flux. The decrease in surface net LW flux is largely compensated by an increase in latent heat flux (Fig. 2.5c) while the contributions from the sensible heat flux and net downward SW flux are secondary (Figs. 2.5b,d). The total difference in net surface energy balance is only 0.1 W m^{-2} over the entire Sahara and Sahel (Table 2.1). An increase of latent heat flux implies increased evaporation. A further look of the NEW–CTL difference in the planetary boundary layer can explain the increase in downward LW flux at the surface in the NEW run.

Figures 2.6a and 2.6b show the differences between the NEW and CTL runs in temperature and in humidity at 900 hPa, respectively. Differences in regionally averaged temperature and humidity profiles are shown in Figs. 2.6c and 6d, respectively. In the Sahara, the NEW run has a slightly warmer boundary layer (up to 0.5 K) than the CTL run. The temperature difference between the NEW and CTL run monotonically decreases from the boundary layer to 500 hPa and then oscillates around zero. In the Sahel, the temperature difference is much smaller. In contrast, the humidity differences are unanimously positive for both the Sahara and Sahel and are statistically significant for all tropospheric levels in the Sahel and for the majority of upper and

middle tropospheric levels in the Sahara (Fig. 2.6d). The NEW − CTL difference in 900-hPa specific humidity is 0.18 g kg^{-1} for the Sahel and 0.12 g kg^{-1} for the Sahara, respectively. As discussed later, these wetter and hotter boundary layers in the NEW run can contribute to differences in the precipitation.

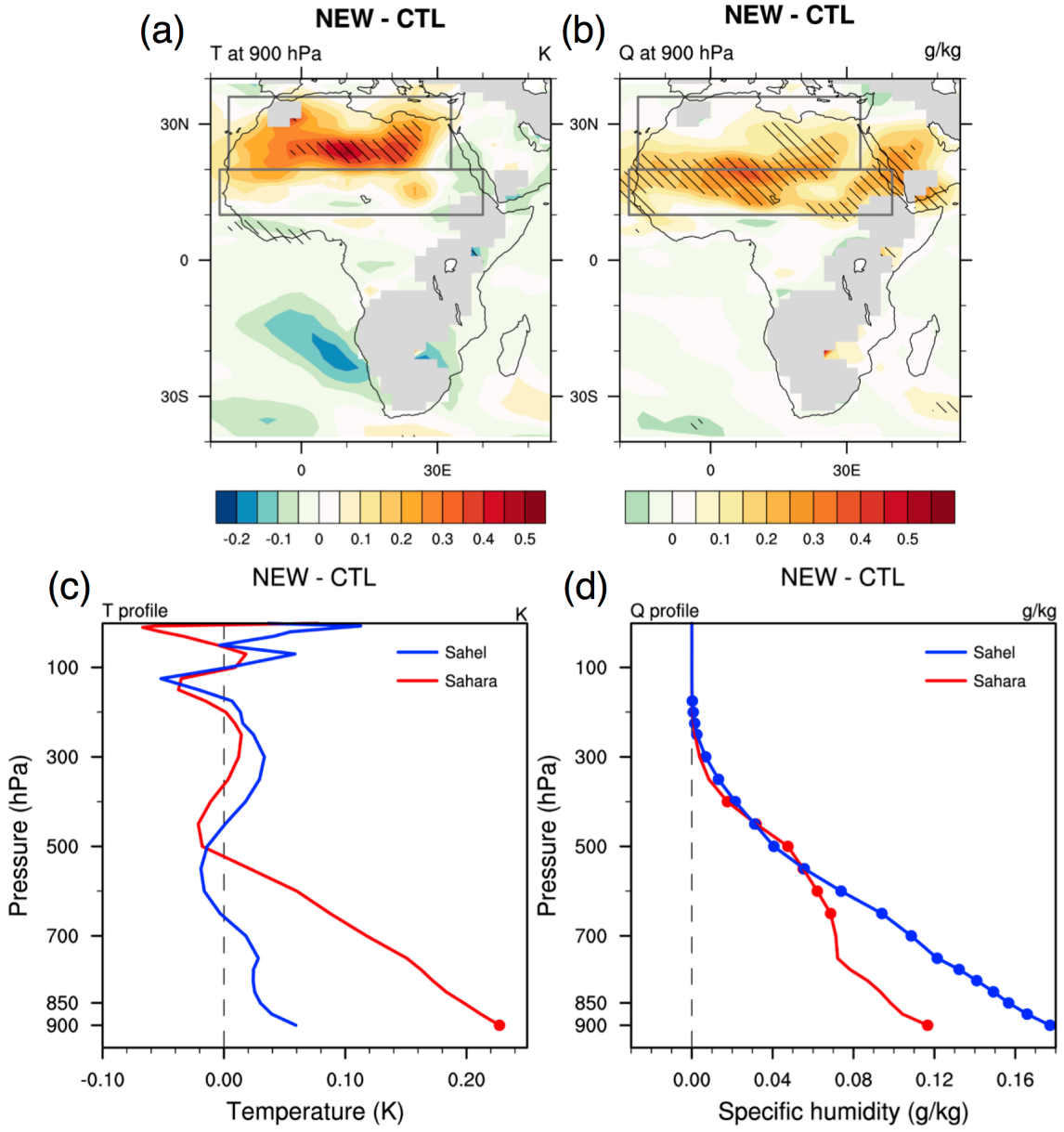

Fig. 2.6. (a) The long-term temperature difference at 900 hPa between the NEW and CTL runs. (b) As in (a), but for the specific humidity at 900 hPa. Slashed area indicates 5% significance level. The two rectangles define the Sahara and Sahel. (c) The temperature difference from 900 hPa to the TOA between the NEW and CTL runs averaged over the Sahara (red) and Sahel (blue). (d) As in (c), but for the specific humidity. Dots indicate the levels where the differences pass the Student's *t* test at 5% significance level.

Table 2.1. Simulated energy budget and other key meteorological variables averaged over the Sahara and Sahel from the CTL run and the corresponding differences between the NEW and CTL runs. All results are based on the 30-yr average using the simulations from year 6 to year 35.

	CTL	NEW − CTL difference (mean ± standard error)
	Surface energy budget	
LW flux↑ ($W m^{-2}$; broadband)	450.60	1.90 ± 0.39
LW flux↑ ($W m^{-2}$; far-IR band, 10–630 cm^{-1})	180.07	1.98 ± 0.09
LW flux↑ ($W m^{-2}$; window band, 820–1180 cm^{-1})	109.93	−3.12 ± 0.11
LW flux↓($W m^{-2}$; all sky)	356.59	4.23 ± 0.50
LW flux↓ ($W m^{-2}$; clear sky)	349.91	4.02 ± 0.44
LW net↑ ($W m^{-2}$)	94.01	−2.34 ± 0.50
SW flux↑ ($W m^{-2}$)	76.32	−0.71 ± 0.28
SW flux↓ ($W m^{-2}$; all sky)	243.15	−1.82 ± 0.65
SW flux↓ ($W m^{-2}$; clear sky)	272.14	−0.34 ± 0.14
SW net↓ ($W m^{-2}$)	166.83	−1.10 ± 0.37
Latent heat flux ($W m^{-2}$)	24.67	1.33 ± 0.50
Sensible heat flux ($W m^{-2}$)	47.85	−0.20 ± 0.37
Surface net↓ flux ($W m^{-2}$)	0.30	0.10 ± 0.04
	TOA energy budget	
LW flux↑ ($W m^{-2}$; broadband)	268.25	−3.27 ± 0.52
LW flux↑ ($W m^{-2}$; far-IR band, 10–630 cm^{-1})	115.01	−0.31 ± 0.15
LW flux↑ ($W m^{-2}$; window band, 820–1180 cm^{-1})	83.74	−2.47 ± 0.22
SW flux net↓($W m^{-2}$)	266.15	−0.78 ± 0.25
	Others	
Surface air temperature (K)	297.34	0.32 ± 0.06
Temperature at 900 hPa (K)	294.53	0.14 ± 0.08
Specific humidity at 900 hPa ($g kg^{-1}$)	6.81	0.15 ± 0.06
Net column radiative cooling rate ($W m^{-2}$)	74.92	−1.26 ± 0.23
Vertical velocity at 500 hPa ($hPa day^{-1}$)	13.74	−0.58 ± 0.48
Convective precipitation rate ($mm day^{-1}$)	0.75	0.05 ± 0.03
Stratiform precipitation rate ($mm day^{-1}$)	0.22	0.02 ± 0.01

Table 2.1 summarizes the NEW–CTL differences for the energy budget terms and other key climate variables, averaged over the Sahara and Sahel. The differences shown in Figs. 2.4–2.6 can be used to help understand the surface energy budget differences in Table 2.1. Both simulations can be deemed as attaining energy balance at the surface in the Sahara and Sahel: the net surface downward heat flux is 0.30 W m^{-2} in the CTL run and 0.40 W m^{-2} in the NEW run. The NEW run has a larger surface upward LW broadband flux by 1.90 W m^{-2}. The downward LW flux at the surface in the

NEW run is increased by 4.23 W m^{-2}, which is primarily due to a warmer and wetter boundary layer in the NEW run that emits more IR radiation downward. As a result, the net upward LW flux at the surface is reduced by 2.34 W m^{-2}. Note that simulated clouds in these two runs contribute little to the increase of downward LW flux at the surface because the NEW–CTL difference in all-sky downward LW flux at the surface is almost the same as the difference in clear-sky downward LW flux at the surface (4.23 vs 4.02 W m^{-2}). On the other hand, the net SW downward flux is reduced by 1.10 W m^{-2} and such reduction is largely caused by the differences in clouds because the NEW–CTL differences in clear-sky downward SW flux at surface is only reduced by 0.34 W m^{-2} (The change in simulated cloud fields will be elaborated on in the next subsection). Combining the LW and SW flux together, the net upward radiative flux at the surface is reduced by 1.24 W m^{-2} from the CTL run to the NEW run. As a compensation, the upward latent heat flux is increased by 1.33 W m^{-2}, implying more evaporation in the NEW run, which is consistent with the warmer boundary layer shown in Fig. 2.6. The slightly warmer boundary layer in the NEW run is also consistent with a reduction of sensible heat flux by 0.2 W m^{-2}.

2.3.1.2 Differences in precipitation and cloud amount

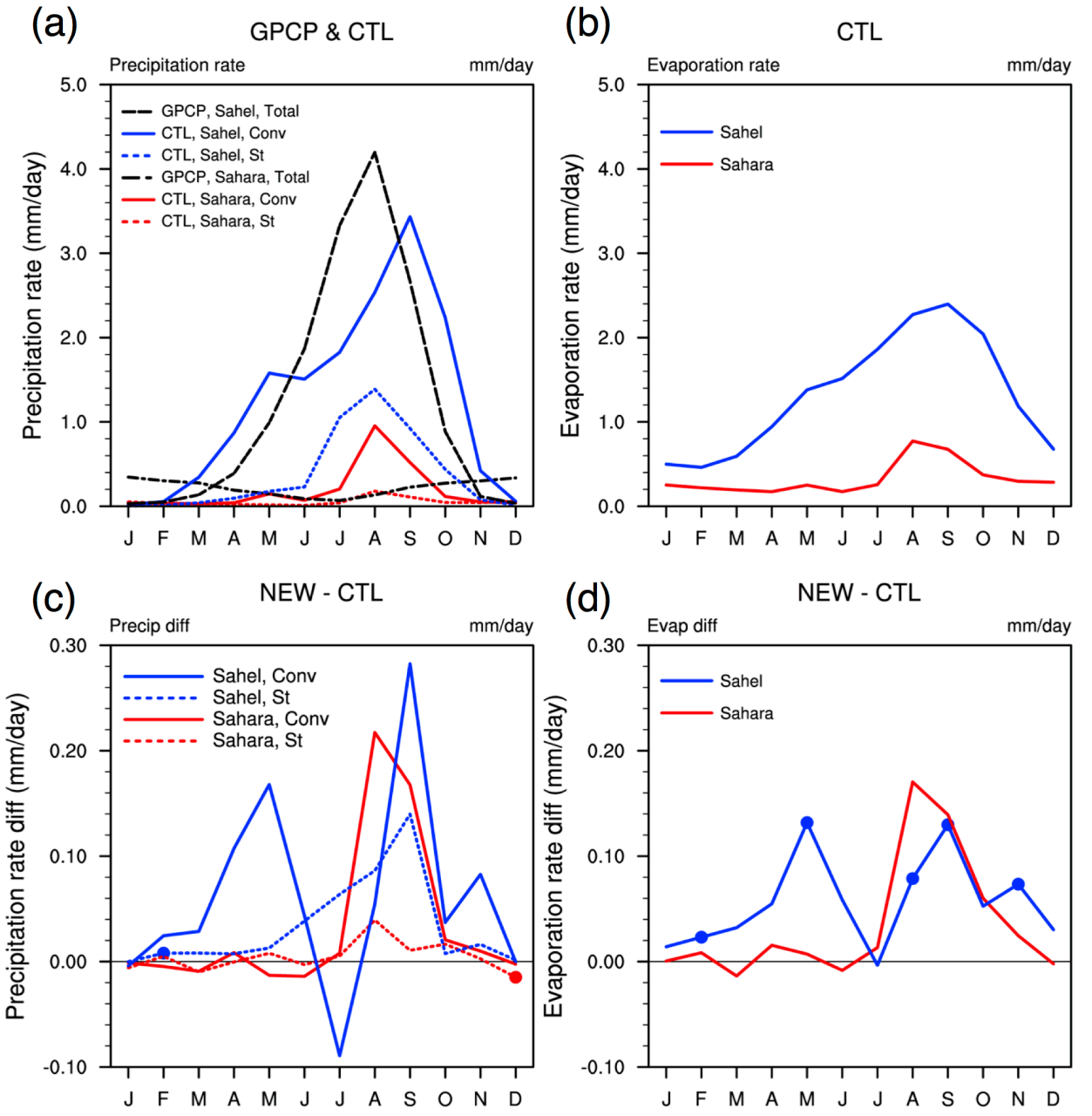

Fig. 2.7. (a) The mean seasonal cycle of precipitation over the Sahara and Sahel from GPCP observations (black lines) and from the CTL run. The convective and stratiform precipitations from the CTL run are plotted separately. (b) The mean seasonal cycle of evaporation rate as simulated by the CTL run for the Sahara (red) and Sahel (blue). (c) As in (a), but for the differences between the NEW and CTL runs. (d) As in (b), but for the difference between the NEW and CTL runs. Evaporation rate is converted from latent heat flux. Dots in (c) and (d) indicate 5% significance level.

Figure 2.7a shows the seasonal cycle of precipitation in the Sahara and in the Sahel from the CTL run and the Global Precipitation Climatology Project version 2.3 (GPCP; Adler et al. 2003). Compared to the GPCP, the CTL run can capture the seasonal cycle of precipitation in the Sahel reasonably well, but in the Sahara it exhibits excessive rain from July to September. Figure 2.7a also shows that in both regions the convective precipitation dominates over the stratiform precipitation in the CTL run. Simulated seasonal cycle of latent heat flux (Fig. 2.7b; shown in terms of evaporation rate in mm day^{-1}) clearly shows that the unrealistic rainfall in July–September in the Sahara is related to the latent heat flux.

Figure 2.7c shows the NEW–CTL difference in precipitation rate as a function of calendar month, for convective and stratiform rainfall. In the Sahara, an increased precipitation can be seen from July to September, especially in August. Moreover, such precipitation increase is virtually all due to the increase in convective rainfall, with the largest value happening in August (0.22 mm day^{-1}, or ~23% increase from the August climatology of the CTL run). In the Sahel, the difference in precipitation occurs in both rainy and dry seasons and is also dominated by convective rainfall change. Unlike in the Sahara, the difference in stratiform precipitation is nonnegligible, especially in the rainy season. The convective precipitation difference in the Sahel has two distinct peaks: one in May (0.17 mm day^{-1}; 11% increase) and the other in September (0.28 mm day^{-1}; 8% increase). Thus, the percentage change of precipitation due to inclusion of surface spectral emissivity is much larger in the Sahara than in the Sahel. Figure 2.7d shows the monthly-mean difference of latent heat fluxes between the NEW and CTL runs for the Sahara and Sahel, respectively. The monthly variations of such latent heat flux

differences are well correlated with the corresponding precipitation differences in Fig. 2.7c. Moreover, the latent heat flux difference in the Sahara can explain almost all of the precipitation difference in the same region (Fig. 2.7c vs Fig. 2.7d) but it is not the same for the Sahel. This implies that the precipitation changes in the Sahara are almost entirely due to enhanced local evaporation but in the Sahel moisture flux from other regions must have contributed significantly to rainfall difference. Together with temperature and humidity differences shown in Figs. 2.4 and 2.6, this suggests that using more realistic surface spectral emissivity for the Sahara and Sahel in the CESM leads to more evaporation and more favorable atmospheric conditions for convection, resulting in more convective precipitation. Such precipitation increase is particularly notable during the boreal summer in the Sahara, exacerbating the wet bias over the Sahara in the standard CESM.

Figure 2.8 shows the seasonal cycle of simulated cloud fraction by the CTL run and the difference between the NEW and CTL runs, for both the Sahara and Sahel. As expected, clouds are infrequent over the Sahara throughout the entire year (Fig. 2.8a), with the monthly-mean cloud fraction at each layer consistently less than 10%. Comparing the NEW run with the CTL run, there is an increase in cloud fraction up to 2% in the NEW run throughout the troposphere in August and September over the Sahara, consistent with the peak of precipitation increase shown in Fig. 2.7c. Over the Sahel, high clouds dominate almost every month while middle and low clouds only occur frequently during the rainy season from July to September (Fig. 2.8b). Positive cloud amount differences between the NEW and CTL runs are seen in virtually all tropospheric layers in the Sahel (Fig. 2.8d), especially the low-level clouds in May and

September, which are statistically significant at 5% level, consistent with the large increase of precipitation in these 2 months (Fig. 2.7c).

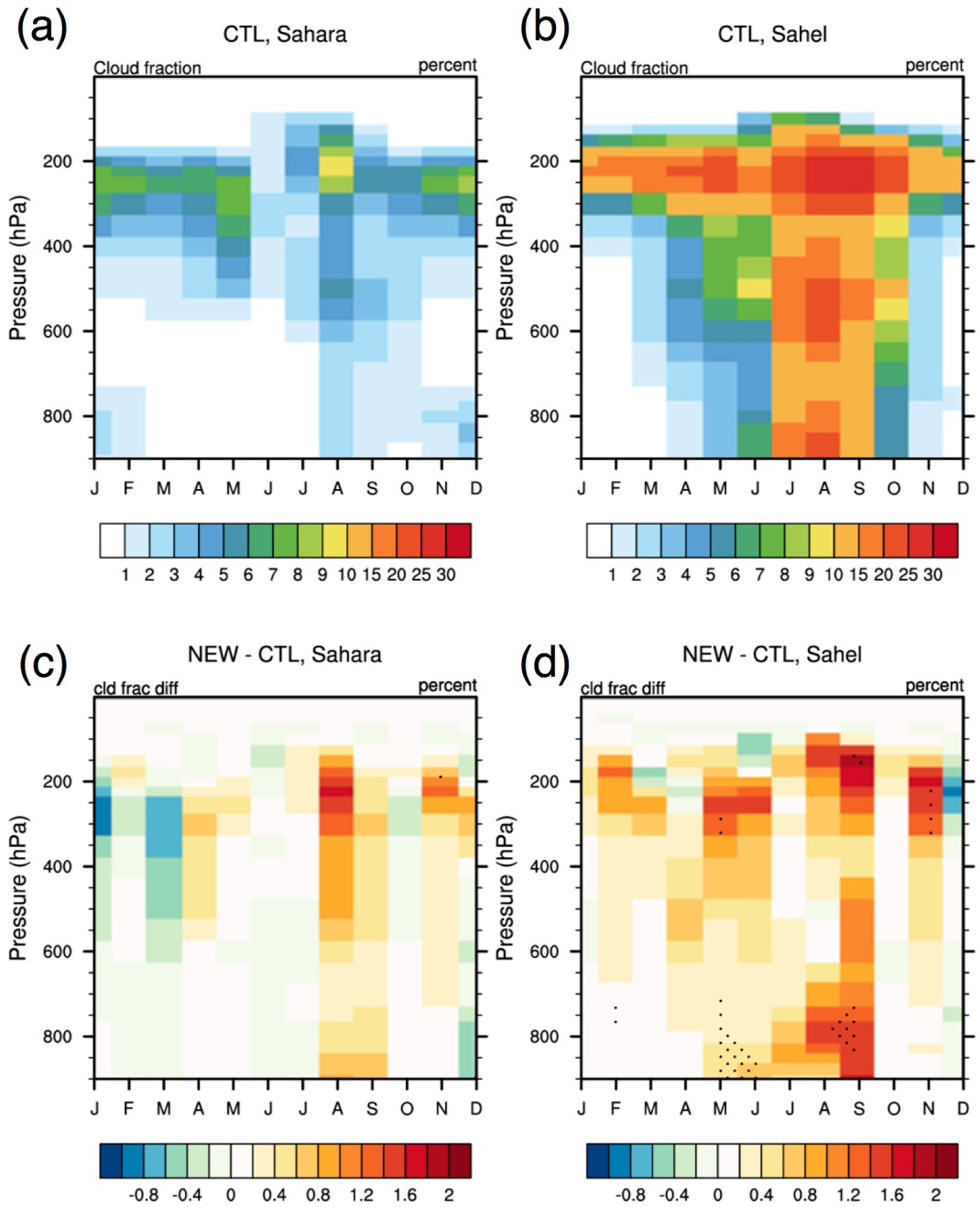

Fig. 2.8. (a) Mean seasonal cycle of simulated cloud fraction in each vertical layer by the CTL run for the Sahara. (b) As in (a), but for the Sahel. (c) As in (a), but for the difference between the NEW and CTL runs. (d) As in (c), but for the difference in the Sahel. Black dots indicate 5% significance level.

Figures 2.7 and 2.8 suggest that the cloud fraction changes between the NEW and CTL runs vary with season and are well correlated with the precipitation changes and latent heat flux changes. Although not all differences shown in the two figures pass the Student's *t* test at 5% significance level, together with Figs. 2.4 and 2.6 they delineate a consistent response to the inclusion of surface spectral emissivity in the Sahara and Sahel: the surface air temperature is higher in the NEW run than in the CTL run and the boundary layer becomes warmer and more humid. These lead to more evaporation from the surface and accordingly more convective precipitation. Figure 2.7 also indicates that the change in the Sahel precipitation is not solely due to convective rainfall and cannot be explained by local evaporation changes alone, indicating changes of moisture convergence and thus possible change of regional circulation due to the inclusion of surface spectral emissivity. This motivates us to look at regional changes beyond the Sahara and Sahel.

2.3.2 Regional changes beyond the Sahara and Sahel

This subsection examines how the inclusion of realistic surface spectral emissivity in the Sahara and Sahel affects simulated climate in adjacent areas. Figure 2.9 shows the GPCP observed mean precipitation and Fig. 2.10 shows the vertical velocity at 500 hPa (ω_{500}) climatology based on the ECMWF ERA-Interim reanalysis. Also shown in these two figures are the difference between the CTL run and the observations as well as the difference between the NEW and CTL runs. The CTL run overestimates the precipitation over the majority of the African continent (Fig. 2.9b). But for the west part of the Sahel and its south coast (i.e., part of the African ITCZ in the boreal summer) the CTL run underestimates precipitation by 1–2 mm day^{-1}. The NEW run can reduce such negative bias in precipitation by ~0.3 mm day^{-1} and the difference from the CTL run is statistically significant (Fig. 2.9c). Over the same regions, Fig. 2.10c shows statistically significant negative difference in ω_{500} between the NEW and CTL runs, suggesting more ascending motions in the NEW run and thus supporting the rain rate difference shown in Fig. 2.9c. Such improved precipitation simulation is in contrast to the exacerbation of positive precipitation bias in the east part of the Sahara and the majority of the Sahel (Figs. 2.9b,c), as discussed in the previous subsection. The differences in ω_{500} over the Sahara and north part of the Sahel, although positive, are not statistically significant, likely owing to the large year-to-year fluctuation of vertical velocity. These results indicate that changing the surface spectral emissivity over the Sahara and Sahel can lead to statistically significant changes in precipitation and ω_{500} over the adjacent regions, especially south to the Sahel. Such changes can partially address the dry biases in the CTL run with respect to the observations.

Meanwhile, the wet bias in the Sahara and Sahel is amplified as a result of more realistic representation of surface emissivity, suggesting that some compensating biases in the standard CESM are masked by unrealistic representation of surface spectral emissivity.

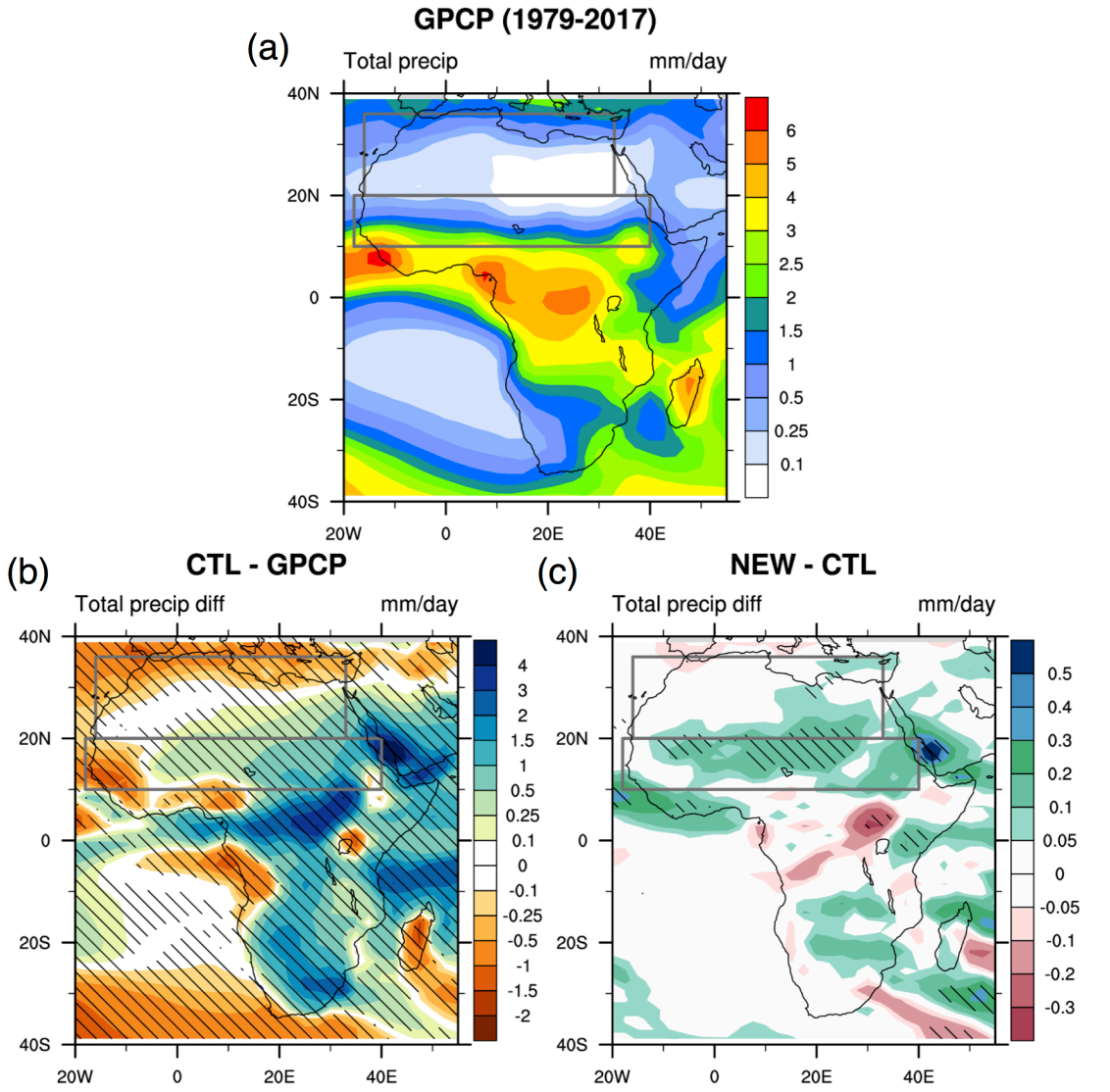

Fig. 2.9. (a) Observed mean precipitation based on the GPCP climatology from 1979 to 2017. (b) The difference of long-term mean precipitation rate between the CTL run and GPCP. (c) As in (b), but for the differences between the NEW and CTL runs. The slashed area indicates 5% significance level. The two gray rectangles define the Sahara and Sahel.

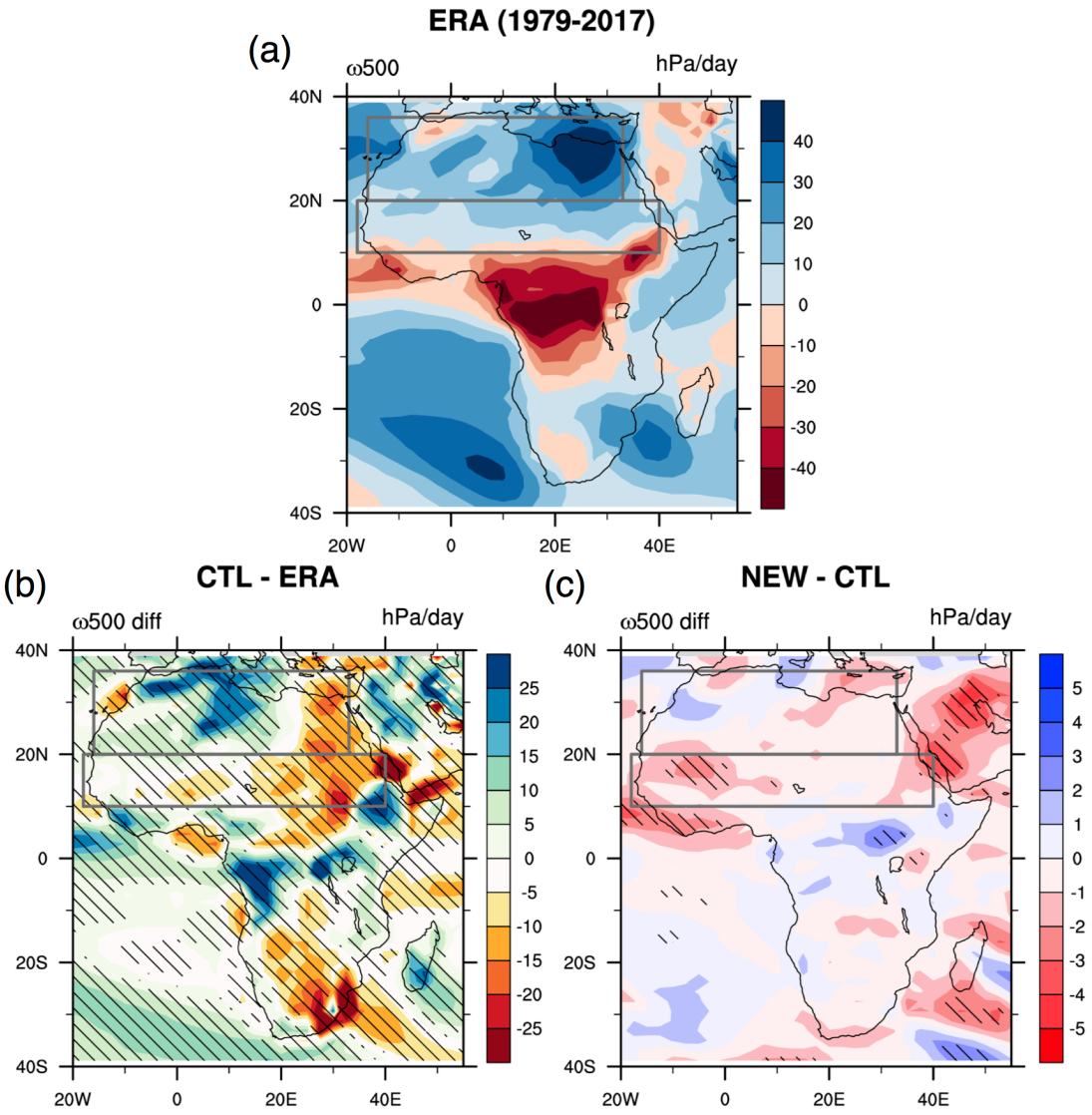

Fig. 2.10. As in Fig. 2.4, but for vertical velocity at 500 hPa.

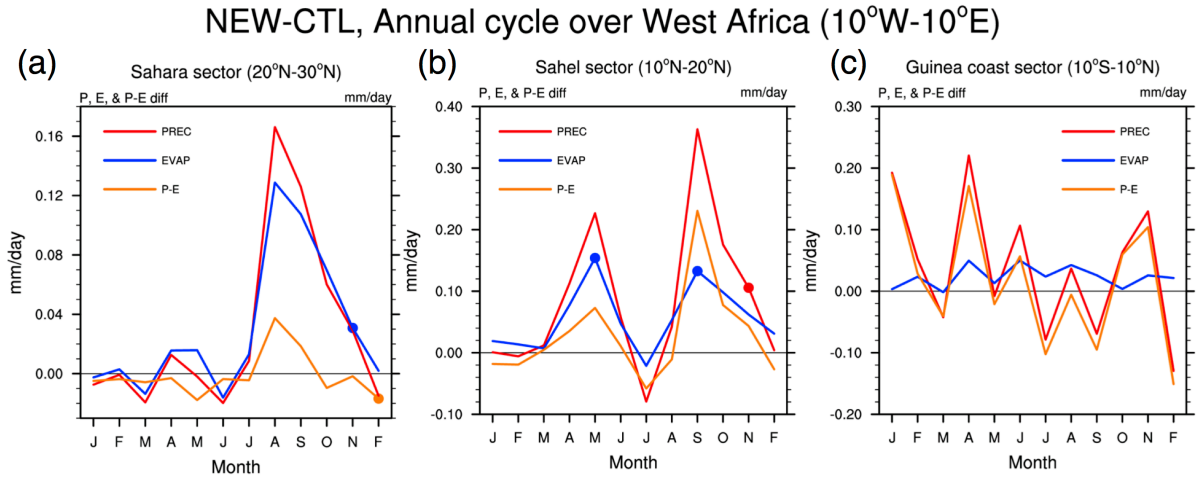

Fig. 2.11. (a) Mean seasonal cycles of the differences between the NEW and CTL runs in precipitation rate (red), evaporation rate (blue), and in precipitation minus evaporation rate ($P - E$; orange). All are averaged over the Sahara sector of West Africa (20°–30°N, 10°W–10°E). (b) As in (a), but for the Sahel sector (10°–20°N, 10°W–10°E). (c) As in (a), but for the Gulf of Guinea and the coastal region north of it (10°S–10°N, 10°W–10°E). Dots on the plots indicate 5% significance level.

Figure 2.9c also indicates that the NEW run has larger annual mean precipitation than the CTL run over most of West Africa (10°W–10°E), from the coastal region north of the Gulf of Guinea to the lower boundary of the Sahara around 20°N. The choice of 10°W–10°E is to be consistent with geographical regions defined in previous studies about West Africa (e.g., Nicholson and Grist 2003; Thorncroft et al. 2011). Precipitation in West Africa is strongly associated with local evaporation as well as moisture transport from outside regions (Gong and Eltahir 1996; Nieto et al. 2006; Thorncroft et al. 2011). Thus, we further examine the individual contributions from local evaporation and moisture transport to such precipitation changes over different sectors within West Africa. Figure 2.11 shows the mean seasonal cycles of NEW–CTL differences in precipitation rate, evaporation rate as converted from latent heat flux, and precipitation minus evaporation rate ($P - E$, a proxy of moisture flux convergence) for three sectors in West Africa, namely the Sahara sector (20°–30°N), the Sahel sector (10°–20°N), and

the Guinea coast sector (including Gulf of Guinea and the coastal region north of it; 10°S–10°N). The precipitation rate increases over the Sahara sector and is mainly due to the increase in local evaporation rate (Fig. 2.11a), consistent with the changes in precipitation and latent heat flux over the entire Sahara (Figs. 2.7c,d). Difference in the moisture flux convergence, as represented by difference in $P - E$, contributes little to the precipitation difference. The Sahara is a region featuring large-scale subsidence (Fig. 2.10a) of Hadley circulation and thus low-level circulation is dominated by divergence instead of convergence, which can help explain the dominance of local evaporation for such simulated precipitation differences. For the Sahel sector in West Africa (Fig. 2.11b), differences in evaporation and moisture flux convergence contribute almost equally to the difference in precipitation in April and May. From July to September when the ITCZ moves northward to the Sahel sector, the difference in moisture flux convergence is more responsible for the change in precipitation than the difference in local evaporation. Such findings are consistent with previous studies that use regional climate models to examine Sahel precipitation (e.g., Noble et al. 2014, 2017). For the Guinea coast sector where surface emissivity is not changed from the CTL to the NEW runs, differences in precipitation closely track the differences in moisture flux convergence for all calendar months, with negligible contributions from local evaporation. The fact that the dominant contributor to the precipitation difference transits from local evaporation in the Sahara sector to moisture convergence in the coast of the Gulf of Guinea clearly demonstrates that the change of surface spectral emissivity in the Sahara and Sahel can affect precipitation in adjacent regions via changes of moisture flux convergence to such regions.

2.4 Conclusion

This study demonstrates that the inclusion of more realistic representation of surface spectral emissivity in the Sahara and Sahel can affect simulated climate in these regions as well as adjacent regions. Over the Sahara and Sahel, the NEW run simulates a warmer surface air temperature and a warmer and wetter planetary boundary layer than the CTL run. The surface energy balance in the NEW run is achieved mainly through an increase of latent heat flux compensated by a reduction of net upward radiative flux. Such conditions favor more convection in the NEW run, leading to more convective precipitation in the Sahara and Sahel. In regions south to the Sahel, particularly the north coastal region of the Gulf of Guinea, the NEW run simulates larger annual-mean precipitation and stronger large-scale ascending motion at 500 hPa than the CTL run and such differences are statistically significant. Over West Africa, the rainfall pattern change from the CTL run to the NEW run is caused largely by stronger local evaporation in the Sahara sector, by larger moisture flux convergence in the coastal region of the Gulf of Guinea, and by changes of both local evaporation and moisture convergence in the Sahel.

As far as biases in the CESM with respect to the observations are concerned, the inclusion of surface spectral emissivity in the Sahara and Sahel reduces the cold bias of surface air temperature in the Sahara and the dry biases in the precipitation over the Gulf of Guinea sector. But it also makes the wet bias in precipitation over the Sahel and part of the Sahara worse. Identifying causes of regional biases in a climate model is generally difficult. These biases are usually caused by a myriad of compensating factors in the model. A more realistic representation of surface emissivity in the numerical

models fundamentally improves the surface–atmosphere LW coupling and, thus, eliminates one factor that can contribute to such biases. When the biases are worsened in the NEW run, it indicates that the incorrect assumption of surface emissivity in the CTL run has masked the effects of other representations. From this perspective, the direct benefits of inclusion of surface spectral emissivity are twofold: to eliminate one possible cause for the biases and to help reveal biases from other factors.

The GCM biases in both simulated climatology and major modes of Sahel rainfall versus SST variability have been well documented for the CMIP3 models (e.g., Biasutti and Giannini 2006; Cook and Vizy 2006; Joly et al. 2007) and similar biases were seen in the CMIP5 models as well (e.g., Biasutti 2013). Meanwhile, previous studies have noted that the SSTs alone cannot explain the Sahel rainfall variability in the models (Scaife et al. 2009) and local processes such as vegetation changes can affect the Sahel rainfall and its decadal variations (Zeng et al. 1999; Kucharski et al. 2013). Our study shows that another local process, the surface–atmosphere LW coupling through spectrally varying surface emissivity, can also affect the Sahel rainfall climatology. A follow-up study would be to investigate, given the multidecadal variations of SST and the projection of future SST changes, to what extent the inclusion of surface spectral emissivity can affect the Sahel rainfall (drought) variations and future change.

Desert emissivity has a strong spectral dependence, which can be as low as 0.6–0.7 in the IR window band and close to unity in other LW bands. This study indicates that if a GCM does not take such spectral dependence into account, it will have an incorrect band-by-band partition for the surface upward LW flux and its OLR will have an incorrect band-by-band decomposition with excessive flux from the window band. Given

that most GCMs do not include proper treatments for surface spectral emissivity, future work would be needed to incorporate such treatments in GCMs, thus making the radiative coupling between the atmosphere and the surface more consistent and more realistic. The CESM, for example, assumes constant graybody emissivity in the surface models (i.e., land, ocean, and sea ice) while assuming blackbody in the atmospheric model. To fully solve such spectral inconsistency across different components in the CESM, the same treatments of surface spectral emissivity in the atmospheric model, as done in this study, should be implemented into the surface models as well. Regional climate models and weather forecast models usually assume blackbody surfaces in their radiation schemes too. Inclusion of surface spectral emissivity should in principle improve the surface–atmosphere LW radiative coupling in all weather and climate models.

Acknowledgements:

The authors are thankful to four anonymous reviewers for their insightful and constructive comments. GPCP precipitation data can be obtained from https://www.esrl.noaa.gov/psd/. The ECWMF ERA-Interim data are obtained from http://apps.ecmwf.int/datasets/. The CESM code is obtained from https://svn-ccsm-release.cgd.ucar.edu/model_versions/cesm1_1_1. This material is based upon work supported by the U.S. Department of Energy, Office of Science, Office of Biological and Environmental Research, Climate and Environmental Science Division under Awards DE-SC0012969 and DE-SC0019278 to the University of Michigan.

References

Adler, R.F., and Coauthors, 2003: The Version 2 Global Precipitation Climatology Project (GPCP) Monthly Precipitation Analysis (1979-Present). J. Hydrometeor., 4, 1147-1167. https://doi.org/10.1175/1525-7541(2003)004<1147:TVGPCP>2.0.CO;2.

Baldridge, A. M., S. J. Hook, C. I. Grove, and G. Rivera, 2009: The ASTER Spectral Library version 2.0. Remote Sens. Environ., 113, 711–715, https://doi.org/10.1016/j.rse.2008.11.007.

Biasutti, M., 2013: Forced Sahel rainfall trends in the CMIP5 archive. J. Geophys. Res. Atmos., 118, 1613–1623, doi:10.1002/jgrd.50206.

Biasutti, M., and A. Giannini, 2006: Robust Sahel drying in response to late 20th century forcings. Geophys. Res. Lett., 33, 10–13, doi:10.1029/2006GL026067.

Charney, J., W. J. Quirk, S. Chow, and J. Kornfield, 1977: A Comparative Study of the Effects of Albedo Change on Drought in Semi–Arid Regions. J. Atmos. Sci., 34, 1366–1385,https://doi.org/10.1175/1520-0469(1977)034<1366:ACSOTE>2.0.CO;2.

Chen, X. H., X. L. Huang, and M. G. Flanner, 2014: Sensitivity of modeled far-IR radiation budgets in polar continents to treatments of snow surface and ice cloud radiative properties. Geophys. Res. Lett., 41, 6530–6537, https://doi.org/10.1002/2014GL061216.

Cook, K. H., and E. K. Vizy, 2006: Coupled model simulations of the West African monsoon system: Twentieth- and twenty-first-century simulations. J. Climate, 19, 3681–3703, doi:10.1175/JCLI3814.1.

Dee, D. P., and Coauthors, 2011: The ERA-Interim reanalysis: configuration and performance of the data assimilation system. Quart. J. Roy. Meteor. Soc., 137, 553–597. https://doi.org/10.1002/qj.828.

Druyan, L. M., 2011: Studies of 21st-century precipitation trends over West Africa. Int. J. Climate, 31, 1415–1424, https://doi.org/10.1002/joc.2180.

Epule, E. T., C. Peng, L. Lepage, and Z. Chen, 2014: The causes, effects and challenges of Sahelian droughts: A critical review. Reg. Environ. Chang., 14, 145–156, https://doi.org/10.1007/s10113-013-0473-z.

Fontaine, B., M. Gaetani, A. Ullmann, and P. Roucou, 2011: Time evolution of observed July-September sea surface temperature-Sahel climate teleconnection with removed quasi-global effect (1900-2008). J. Geophys. Res. Atmos., 116, 1–17, doi:10.1029/2010JD014843.

Giannini, A., 2003: Oceanic Forcing of Sahel Rainfall on Interannual to Interdecadal Time Scales. Science, 302, 1027–1030, https://doi.org/10.1126/science.1089357.

Gong, C., and E. Eltahir, 1996: Sources of moisture for rainfall in West Africa. Water Resour. Res., 32, 3115–3121, https://doi.org/10.1029/96WR01940.

Held, I. M., T. L. Delworth, J. Lu, K. L. Findell, and T. R. Knutson, 2005: Simulation of Sahel drought in the 20th and 21st centuries. Proc. Natl. Acad. Sci., 102, 17891–17896, https://doi.org/10.1073/pnas.0509057102.

Huang, H., Y. Gu, Y. Xue, J. Jiang, and B. Zhao, 2018: Assessing aerosol indirect effect on clouds and regional climate of East/South Asia and West Africa using NCEP GFS. Climate Dyn., doi:10.1007/s00382-018-4476-9.

Huang, X. L., X. H. Chen, D. K. Zhou, and X. Liu, 2016: An Observationally Based Global Band-by-Band Surface Emissivity Dataset for Climate and Weather Simulations. J. Atmos. Sci., 73, 3541–3555, https://doi.org/10.1175/JAS-D-15-0355.1.

Huang, X. L., X. H. Chen, M. Flanner, P. Yang, D. Feldman, and C. Kuo, 2018: Improved representation of surface spectral emissivity in a global climate model and its impact on simulated climate. J. Climate, 31, 3711-3727, https://doi.org/10.1175/JCLI-D-17-0125.1.

Hurrell, J. W., J. J. Hack, D. Shea, J. M. Caron, and J. Rosinski, 2008: A new sea surface temperature and sea ice boundary dataset for the community atmosphere model. J. Climate, 21, 5145–5153, https://doi.org/10.1175/2008JCLI2292.1.

Hurrell, J. W., and Coauthors, 2013: The Community Earth System Model: A Framework for Collaborative Research. Bull. Amer. Meteor. Soc., 94, 1339–1360, doi:10.1175/BAMS-D-12-00121.1. http://journals.ametsoc.org/doi/abs/10.1175/BAMS-D-12-00121.1.

IPCC, 2013: Climate Change 2013: The Physical Science Basis. Contribution of Working Group I to the Fifth Assessment Report of the Intergovernmental Panel on Climate Change [Stocker, T.F., D. Qin, G.-K. Plattner, M. Tignor, S.K. Allen, J. Boschung, A. Nauels, Y. Xia, V. Bex and P.M. Midgley (eds.)]. Cambridge University Press, Cambridge, United Kingdom and New York, NY, USA, 1535 pp, https://doi.org/10.1017/CBO9781107415324.

Joly, M., A. Voldoire, H. Douville, P. Terray, and J.-F. Royer, 2007: African monsoon teleconnections with tropical SSTs: validation and evolution in a set of IPCC4 simulations. Climate Dyn., 29, 1–20, doi:10.1007/s00382-006-0215-8.

Kato, S., and Coauthors, 2018: Surface irradiances of edition 4.0 Clouds and the Earth's Radiant Energy System (CERES) Energy Balanced and Filled (EBAF) data product. J. Climate, 31, 4501–4527, doi:10.1175/JCLI-D-17-0523.1.

Kucharski, F., N. Zeng, and E. Kalnay, 2013: A further assessment of vegetation feedback on decadal Sahel rainfall variability. Climate Dyn., 40, 1453–1466, doi:10.1007/s00382-012-1397-x.

Loeb, N. G., and Coauthors, 2018: Clouds and the Earth'S Radiant Energy System (CERES) Energy Balanced and Filled (EBAF) top-of-atmosphere (TOA) edition-4.0 data product. J. Climate, 31, 895–918, doi:10.1175/JCLI-D-17-0208.1.

Mlawer, E. J., S. J. Taubman, P. D. Brown, M. J. Iacono, and S. A. Clough, 1997: Radiative transfer for inhomogeneous atmospheres: RRTM, a validated correlated-k model for the longwave. J. Geophys. Res., 102, 16663-16682, https://doi.org/10.1029/97JD00237.

Mohino, E., S. Janicot, and J. Bader, 2011: Sahel rainfall and decadal to multi-decadal sea surface temperature variability. Climate Dyn., 37, 419–440, doi:10.1007/s00382-010-0867-2.

Monerie, P. A., E. Sanchez-Gomez, and J. Boé, 2017: On the range of future Sahel precipitation projections and the selection of a sub-sample of CMIP5 models for impact studies. Climate Dyn., 48, 2751–2770, https://doi.org/10.1007/s00382-016-3236-y.

Monerie, P. A., T. Oudar, and E. Sanchez-Gomez, 2018: Respective impacts of Arctic sea ice decline and increasing greenhouse gases concentration on Sahel precipitation. Climate Dyn., doi:10.1007/s00382-018-4488-5.

Nicholson, S. E., and J. P. Grist, 2003: The seasonal evolution of the atmospheric circulation over West Africa and equatorial Africa. J. Climate, 16, 1013–1030, doi:10.1175/1520-0442(2003)016<1013:TSEOTA>2.0.CO;2.

Nieto, R., L. Gimeno, and R. M. Trigo, 2006: A Lagrangian identification of major sources of Sahel moisture. Geophys. Res. Lett., 33, 1–6, https://doi.org/10.1029/2006GL027232.

Noble, E., L. M. Druyan, and M. Fulakeza, 2014: The Sensitivity of WRF Daily Summertime Simulations over West Africa to Alternative Parameterizations. Part I: African Wave Circulation. Mon. Wea. Rev., 142, 1588–1608, doi:10.1175/MWR-D-13-00194.1. http://journals.ametsoc.org/doi/abs/10.1175/MWR-D-13-00194.1.

Noble, E., L. M. Druyan, and M. Fulakeza, 2017: The Sensitivity of WRF Daily Summertime Simulations over West Africa to Alternative Parameterizations. Part II: Precipitation. Mon. Wea. Rev., 145, 215–233, doi:10.1175/MWR-D-15-0294.1.

Rodríguez-Fonseca, B., and Coauthors, 2015: Variability and Predictability of West African Droughts: A Review on the Role of Sea Surface Temperature Anomalies. J. Climate, 28, 4034–4060, doi:10.1175/JCLI-D-14-00130.1.

Rotstayn, L. D., and U. Lohmann, 2002: Tropical rainfall trends and the indirect aerosol effect. J. Climate, 15, 2103–2116, https://doi.org/10.1175/1520-0442(2002)015<2103:TRTATI>2.0.CO;2.

Scaife, A. A., and Coauthors, 2009: The CLIVAR C20C project: selected twentieth century climate events. Climate Dyn., 33, 603–614, doi:10.1007/s00382-008-0451-1.

Smith, D. M., N. J. Dunstone, A. A. Scaife, E. K. Fiedler, D. Copsey, and S. C. Hardiman, 2017: Atmospheric response to Arctic and Antarctic sea ice: The importance of ocean-atmosphere coupling and the background state. J. Climate, 30, 4547–4565, doi:10.1175/JCLI-D-16-0564.1.

Sud, Y. C., and M. Fennessy, 1982: A study of the influence of surface albedo on July circulation in semi-arid regions using the glas GCM. J. Climatol., 2, 105–125, https://doi.org/10.1002/joc.3370020202.

Sylla M.B., Nikiema P.M., Gibba P., Kebe I., Klutse N.A.B., 2016: Climate Change over West Africa: Recent Trends and Future Projections. Adaptation to Climate Change and Variability in Rural West Africa. Yaro J., Hesselberg J. Ed., Springer, 25-40.

Taylor, C. M., E. F. Lambin, N. Stephenne, R. J. Harding, and R. L. H. Essery, 2002: The Influence of Land Use Change on Climate in the Sahel. J. Climate, 15, 3615–3629, https://doi.org/10.1175/1520-0442(2002)015<3615:TIOLUC>2.0.CO;2.

Thorncroft, C., H. Nguyen, C. Zhang, and P. Peyrille, 2011: Annual cycle of the West African monsoon: Regional circulations and associated water vapour transport. Quart. J. Roy. Meteor. Soc., 137, 129–147, https://doi.org/10.1002/qj.728.

Wilber,A. C., D. P.Kratz, and S.K.Gupta, 1999: Surface emissivity maps for use in satellite retrievals of longwave radiation. NASA Tech. Publ. NASA/TP-1999-209362, 35 pp. [Available online at http://www-cave.larc.nasa.gov/pdfs/Wilber.NASATchNote99.pdf.]

Xue, Y., and J. Shukla, 1993: The Influence of Land Surface Properties on Sahel Climate. Part 1: Desertification. J. Climate, 6, 2232–2245, https://doi.org/10.1175/1520-0442(1993)006<2232:TIOLSP>2.0.CO;2.

Xue, Y., and Coauthors, 2010: Intercomparison and analyses of the climatology of the West African Monsoon in the West African Monsoon Modeling and Evaluation project (WAMME) first model intercomparison experiment. Climate Dyn., 35, 3–27, doi:10.1007/s00382-010-0778-2.

Xue, Y., and Coauthors, 2016: West African monsoon decadal variability and surface-related forcings: second West African Monsoon Modeling and Evaluation Project Experiment (WAMME II). Climate Dyn., 47, 3517–3545, doi:10.1007/s00382-016-3224-2.

Zeng, N., J. D. Neelin, K. M. Lau, and C. J. Tucker, 1999: Enhancement of Interdecadal Climate Variability in the Sahel by Vegetation Interaction. Science (80-.)., 286, 1537–1540, doi:10.1126/science.286.5444.1537.

Zhou, D. K., A. M. Larar, X. Liu, W. L. Smith, L. L. Strow, P. Yang, P. Schlüssel, and X. Calbet, 2011: Global land surface emissivity retrieved from satellite ultraspectral IR measurements. IEEE Trans. Geosci. Remote Sens., 49, 1277–1290, https://doi.org/10.1109/TGRS.2010.2051036.

Chapter 3

Seasonal Dependent Impact of Cloud Longwave Scattering on the Polar Climate

3.1 Introduction

Cloud-radiation interactions play an important role in the Earth's climate system [Stephens 2005; Ceppi et al., 2017; and references therein]. Cloud can absorb and scatter incident shortwave (SW) and longwave (LW) radiation, and emit LW radiation itself. These radiative processes depend on both cloud macroscopic properties (e.g. cloud amount, cloud top temperature) as well as its microscopic optical properties, namely extinction optical depth, single scattering albedo, and phase function, all of which are decided by the cloud droplet size distribution, particle shape, cloud water content, and sometimes particle orientation. Correct and faithful representations of these cloud radiative properties and cloud-radiation interactions in climate models, usually referred to as cloud-radiation parameterization, are critical to the success of climate modeling. Sustained efforts have been invested for the cloud-radiation parameterizations [e.g. Stephens 1984; Randall 1989; Fu and Liou 1993; Edward and Slingo 1996; Mlawer et al. 1997; Pincus et al. 2003; Yang et al. 2015], but many challenges and issues still remain.

Because numerous processes involve in the cloud-radiation parameterizations and resolving all of them is extremely computational expensive, climate models usually

make reasonable approximations for the sake of computational cost. One widely used approximation is the neglect of the LW scattering effect of clouds. Chen et al. [2014] and Kuo et al. [2020] surveyed climate models that participated in the IPCC 5th assessment report and found that only models from three modeling centers had considered the cloud LW scattering effect. The traditional rationales for modelers to neglect cloud LW scattering in the weather and climate models are two folds: (1) In the LW spectrum, the imaginary parts of the index of refraction for both ice and liquid are orders of magnitude larger than those in the SW spectrum. As a result, the overall attenuation of LW radiation by cloud alone is largely due to absorption instead of scattering. (2) LW is featured with prominent gaseous absorptions by H_2O, CO_2, O_3, and other trace gases. For a given vertical layer in the atmosphere and for LW, its layer-mean single scattering albedo, which describes the probability an attenuated photon being scattered instead of being absorbed in the layer, can be expressed as

$$\omega = \frac{\omega_c \Delta\tau_c}{\Delta\tau_{air}+\Delta\tau_c} \qquad (3.1),$$

where $\Delta\tau_{air}$ is the gaseous optical thickness of the layer, $\Delta\tau_c$ is the cloud optical thickness, and ω_c is the single scattering albedo of cloud. All variables in eq. (1) are frequency dependent so the subscript for frequency is omitted for brevity. As long as $\Delta\tau_{air} \gg \Delta\tau_c$, the scattering of the layer is negligible regardless of the value of ω_c. Such conditions usually hold for the spectral bands with strong greenhouse gas absorptions, e.g., the center of CO_2 15μm band (630-690 cm^{-1}) with $\Delta\tau_{air}$ ranging from 100 to ~9000 in the troposphere. For the H_2O bands, this is also the case as long as water vapor is abundantly presented in the air, e.g. in the tropics and mid-latitudes.

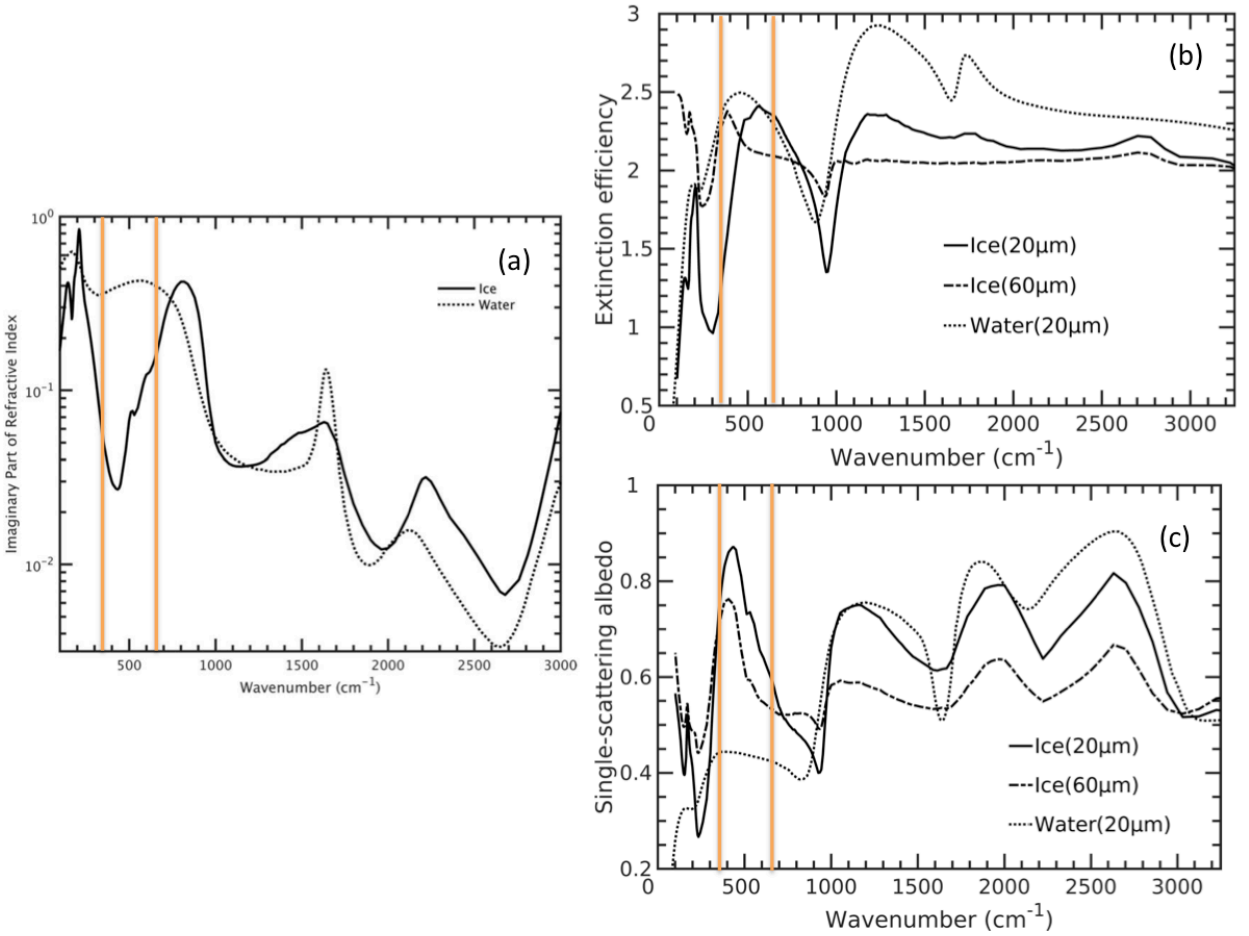

Fig. 3.1. (a) The imaginary part of the index of refraction for ice (solid line) and liquid water (dotted line) over the LW spectrum. (b) The extinction coefficients of ice particles and water droplet over the LW spectrum with several assumed effective diameters. The effective diameter of the ice particle is 20 μm (solid line) and 60μm (dash-dotted line). The effective diameter of the water droplet is 20 μm (dotted line). (c) Same as (b) but for the single scattering albedo. The two vertical orange lines bracket 350 to 630 cm^{-1}, the bandwidth for two consecutive RRTMG_LW bands. This figure is adopted from Kuo et al. (2017) but with higher spectral resolution.

While the reasoning above is generally applicable to water vapor bands in the tropics and mid-latitudes, it breaks down in the polar region due to three facts. First, the imaginary part of the index of refraction of ice has a local minimum around 400 cm^{-1} (Fig. 3.1a) and, as a result, ice clouds can have a single scattering albedo as large as 0.6-0.8 over 350-630 cm^{-1} (Fig. 3.1c), a portion of far-infrared (far-IR) spectrum featured with water vapor rotational absorption. Second, the same portion of far-IR spectrum

contributes ~35-40% of outgoing LW radiation (OLR) in the polar regions (Fig. 3.2b), which means ice clouds can scatter a fair amount of LW radiation and affect the energy budget. Third, the high-latitude total column water vapor (TCWV) is much smaller than the TCWV in the tropics and mid-latitudes (Fig 3.2a). In the deep Antarctic, the TCWV is only ~ 2 mm or even less owing to its high elevation, and the TCWV variation from summer to winter can be as large as a factor of 2.5. In the Arctic, the TCWV is slightly above 10 mm in the summer and the summer-to-winter variation is about a factor of 5. Since the optical depth is proportional to the density of the absorber, the optical depth of water vapor in high latitudes is also significantly less than those in the extra-polar regions. Therefore, even for the same ice cloud, its LW scattering effect can be much larger in the high latitudes than in the rest of globe, simply because $\Delta\tau_{air}$ of such water vapor band is much smaller in the polar regions than in the rest of the globe. Note that the ice cloud scattering effect can be especially important over the aforementioned far-IR region where the ice cloud scattering effects peak. Given the fractional contribution of this far-IR region to the broadband LW radiation budget, neglecting such scattering effects can be questionable, at least for the simulation of polar climate.

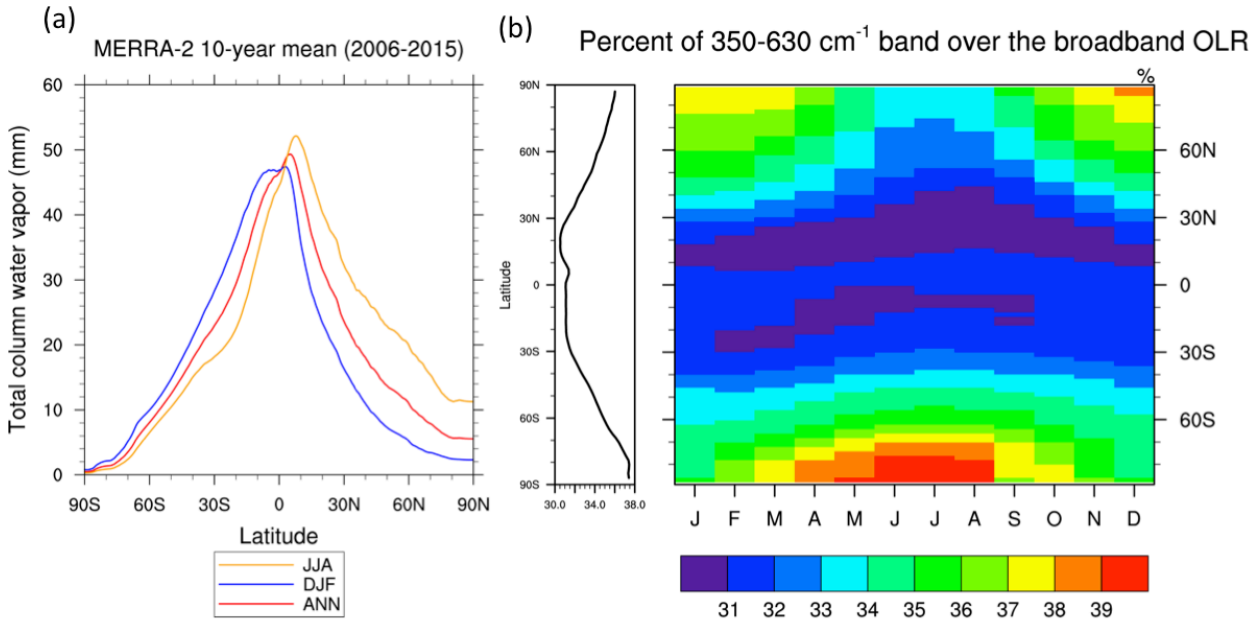

Fig. 3.2 (a) A zonal-mean climatology of total column water vapor as derived from NASA MERRA-2 reanalysis. Ten years of data is used and the results for JJA, DJF, and annual mean are plotted in orange, blue, and red, respectively. (b) The percentage contribution of 350-630cm^{-1} flux to the entire outgoing longwave as a function of latitude and calendar month (right panel) and the annual-mean as a function of latitude (left panel). The result is based on averages of 10-year spectral flux (2006-2015) derived using the method in Huang et al. [2014] from the collocated CERES and AIRS observations.

In order to show the impact of ice cloud scattering on the LW radiative fluxes in the polar regions, we carry out offline radiative transfer model calculations using a typical sub-Arctic summer profile [McClatchy et al. 1972]. The radiative transfer model and ice cloud LW optical scheme are based on Kuo et al. [2020]. Details about these schemes will be given in Section 3.2.1 and the same schemes are used in the following climate simulations. These offline calculations involve different locations of a layer of ice cloud, different cloud optical properties, and different TCWV amount. The cloud layer is assumed at either 7-8 km (equivalent to 359-413 hPa) or 1-2 km (equivalent to 792-896 hPa), representing a high and low cloud condition, respectively. To represent different cloud optical properties, ice particle effective diameter is varied from 10μm to 200μm with a fixed ice water path of 20 g m^{-2}, a typical value for polar cloud. Lastly, the TCWV

is scaled by a factor ranging from 0.25 to 1.5. The ice cloud scattering effect is deemed as the differences between two parallel calculations: one enables the cloud scattering effect and the other disables the scattering effect by setting the cloud extinction optical depth to the absorption optical depth and the single scattering albedo to zero. The scattering effects on the OLR and downward LW flux at the surface (FLDS) are shown in Fig. 3.3.

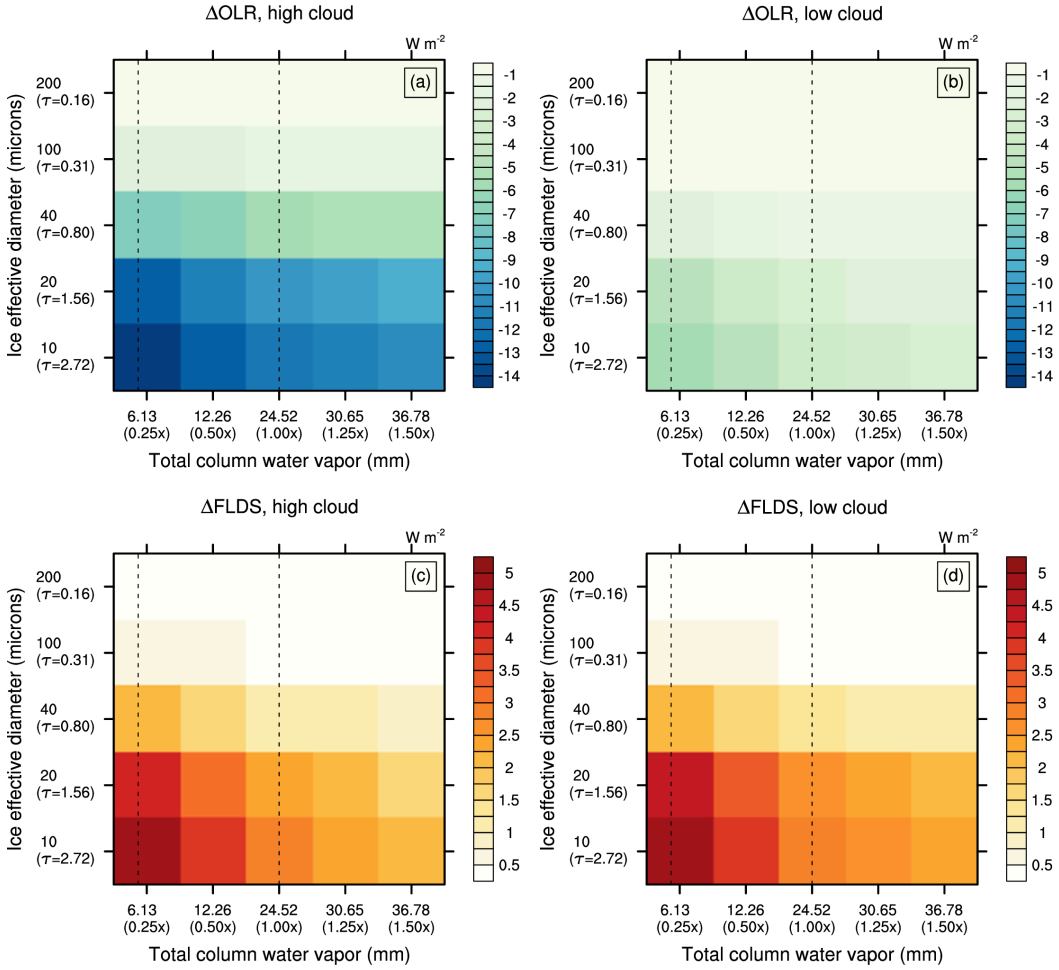

Fig. 3.3 (Upper row) Offline radiative transfer calculation of the change of outgoing LW radiation (ΔOLR) due to the inclusion of ice cloud LW scattering for different combinations of total column water vapor (TCWV) and ice cloud optical properties. A typical sub-Arctic summer sounding profile is used in the calculations and the total column water vapor is scaled by a factor ranging from 0.25 to 1.5. The ice cloud is one layer with a fixed ice water path of 20 g m^{-2}, a typical value for polar cloud. The ice particle effective diameter varies from 10μm to 200μm, and the optical depth at 11μm (τ) is shown in the Y-Axis. Left panel is for a layer of ice cloud at 7-8km (high cloud) and the right panel is at 1-2km (low cloud). (Lower row) Same as the upper row but for the changes of downward longwave flux at the surface (ΔFLDS). On each panel, two vertical dash lines denote the typical TCWV for sub-Arctic winter (left) and summer (right).

There are several noteworthy features in Fig. 3.3. First, The scattering effect decreases the OLR and increases the FLDS, consistent with previous offline calculations over the entire globe [Kuo et al. 2017]. A scattering cloud, compared to a purely absorptive cloud, redirects upwelling LW radiation to different directions, including reflecting it back to surface, which in turn decreases the OLR and increases the FLDS. Second, the smaller ice effective diameter is, the higher single-scattering albedo is (Fig. 3.1c), which then induces collectively strong scattering effect on both the OLR and FLDS. Third, when the TCWV is small and thus the atmosphere has weak absorption of LW radiation, the scattering effects on the OLR and FLDS tend to be strong. Fourth, the reduction of OLR due to scattering is larger than the increase of downward LW flux at surface, implying large atmospheric LW absorption between the surface and cloud, as mentioned in Chen et al. [2014]. Finally, The scattering effect for the low cloud is generally smaller than that for the high cloud, which can be explained using eq. (1) as the optical depth due to water vapor absorption in the lower troposphere is much larger than its counterparts in the upper troposphere. Compared to the high cloud, the scattering effect of the low cloud on the OLR is smaller, which is mainly because a larger amount of water vapor exists between the low cloud top and the top of the atmosphere, implying stronger atmospheric absorption and thus weakening the scattering effect.

Our offline calculations show that the cloud scattering effect can increase the FLDS in the polar regions by several Wm^{-2}, which can affect the surface energy budget and consequently, surface air temperature (SAT). Interestingly, previous studies using climate model simulations to investigate the cloud LW scattering effect have *not*

reported the influences on the SAT in the polar regions (e.g. Zhao et al. 2018; Wu et al. 2019; Jin et al. 2019). We speculate that because all these studies carried out simulations with prescribed sea surface temperatures (SSTs) and sea ice, the LW radiative boundary condition is hence prescribed over oceans so that the LW radiative coupling between surface and atmosphere does not exist over ocean surfaces. Even though the cloud LW scattering can increase the FLDS and potentially alter surface energy budget over the polar ocean, the responses cannot be fully represented when the SSTs and sea ice are prescribed. This poses an issue in assessing the cloud LW scattering effect using prescribed-SST simulations.

The objective of this chapter is to examine the ice cloud LW scattering effect using climate model simulations, with a particular focus on the polar regions. We modify the Community Earth System Model (CESM) version 1.1.1 to include ice cloud LW scattering treatments and use this modified CESM to quantify the impact of ice cloud LW scattering on the polar regions. In order to see the LW coupling effects between the surface and atmosphere, we carry out two types of parallel simulations: one prescribes SSTs and sea ice, similar to the previous studies, and the other uses a slab-ocean model, in which ocean and sea ice have thermodynamic responses to the changes in surface energy processes so the surface temperature is allowed to change as well. Lastly, given the potential contribution from the far-IR bands to the total cloud LW scattering effect, we also examine this in this chapter. The remainder of this chapter is organized as follows: Section 3.2 describes the modified version of the CESM used in this study and the design of simulation experiments. Section 3.3 presents the simulation results and physical interpretations. Conclusions are then given in section 3.4.

3.2 Methods

3.2.1 The modification of cloud-LW radiation schemes in the CESM 1.1.1

The LW radiation scheme used by the CESM 1.1.1 is RRTMG_LW [Mlawer et al. 1997], which does not take LW scattering into account. To include the scattering calculations in the RRTMG_LW, Kuo et al. (2020) implemented a hybrid two-stream and four-stream (2S/4S) radiative transfer solver [Toon et al. 1989; Fu et al. 1997] into the RRTMG_LW. This solver represents the source function using a two-stream approximation, in which the Planck function is approximated linearly in optical depth [Toon et al. 1989]. This source function representation is then combined with a four-stream approximation to solve radiative fluxes [Fu et al. 1997], i.e., two upward streams use the same source function. Compared to the 128-stream DISORT solver (DIScrete Ordinate Radiative Transfer; Stamnes et al. 1988), this modified RRTMG_LW scheme works well in both clear and cloudy conditions in terms of accuracy and efficiency, as revealed in column tests of different atmospheric and cloud profiles. More detailed evaluations and justification of the 2S/4S radiative transfer solver for LW scattering can be found in [Kuo et al. 2020]. I then incorporated this modified RRTMG_LW into the CESM 1.1.1 to study the LW scattering effect on the simulated climate.

The CESM 1.1.1 does not parameterize the LW scattering properties of clouds [Mitchell et al. 1996; Gent et al. 2011]. Because the scattering effects of liquid clouds are generally small over the entire LW spectrum, I hence implemented a new ice cloud-radiation scheme developed by Kuo et al. [2020] into the CESM1.1.1, This scheme parameterizes ice cloud LW optical properties, namely, extinction coefficient, single-scattering albedo, and asymmetric factor, by utilizing the MODIS (Moderate Resolution

Imaging Spectroradiometer) Collection 6 ice cloud model [Platnick et al. 2017) with in-situ observed particle size distributions [Baum et al. 2011; Heymsfield et al. 2010; 2013]. Accurate optical properties of such ice clouds were regressed as a function of the ice effective particle diameter. Details about this new scheme can be found in Kuo et al. [2020]. The ice effective diameter used in the CESM1.1.1 is based on Kristjansson et al. [2000], which parameterized the ice effective diameter as a function of temperature.

3.2.2 CESM simulation settings

Using the modified version of the CESM1.1.1, three sets of experiments are carried out. The scattering effects of liquid clouds are generally small over the entire LW (Fig. 3.1) and thus are not included in this study. The first set of experiments enables the ice cloud LW scattering effect, hereby referred as “Scat”. The second set, called “noScat”, is identical to the first set except cloud LW scattering being turned off by setting cloud extinction optical depth to the absorption optical depth and cloud single scattering albedo to zero. In order to examine the contributions from the far-IR bands, the third set, called “noFIR”, is identical to the Scat set except the ice cloud scattering in the far-IR bands being turned off (10-630 cm^{-1} in the RRTMG_LW). The impact of ice cloud LW scattering on the simulated climate is then deduced by differencing the results from Scat and noScat runs, or from noFIR and noScat runs. To understand how ice cloud LW scattering interacts with the surface, these three experiments are carried out with a slab-ocean model (hereafter, SOM runs), in which ocean and sea ice can have thermodynamic response to the change of surface energy processes and surface

temperature is allowed to change over ocean and sea ice. We also carry out the same three sets of experiments with prescribed climatological SSTs (hereafter, prescribed-SST runs), following the traditional way of assessing atmospheric parameterizations in climate models. To account for model internal variability, four ensemble members are included in each set of simulations. Each member begins with a slightly different initial condition, similar to the settings in the CESM Large Ensemble Project [Kay et al. 2015]. All simulations are carried out for 35 years and the outputs from the last 30 years are used in the following analysis.

A side note is that the default atmospheric physics package in the CESM 1.1.1 is CAM5, but the CESM1.1.1 only supports the slab-ocean simulations with the previous CAM4 atmospheric physics package [Neale et al. 2010]. Hence, we carried out all CESM1.1.1 simulations with the CAM4 physics for both SOM and prescribed-SST runs (the CESM component set “E2000” and “F2000”, respectively), but replaced the LW and SW radiation schemes with the RRTMG_LW and RRTMG_SW, respectively. RRTMG_LW and RRTMG_SW are the radiation schemes used in CAM5 and such changes of radiation scheme configuration can be configured using the scripts with the CESM 1.1.1 package. All simulations are forced with present-day forcings at the level of year 2000. Solar forcing is prescribed without year-to-year variation. The horizontal resolution of the simulations is 1.9^{o} latitude by 2.5^{o} longitude and the number of vertical levels in the atmospheric model is 26.

3.3 Results and discussion

3.3.1 The ice cloud LW scattering effect on surface air temperature

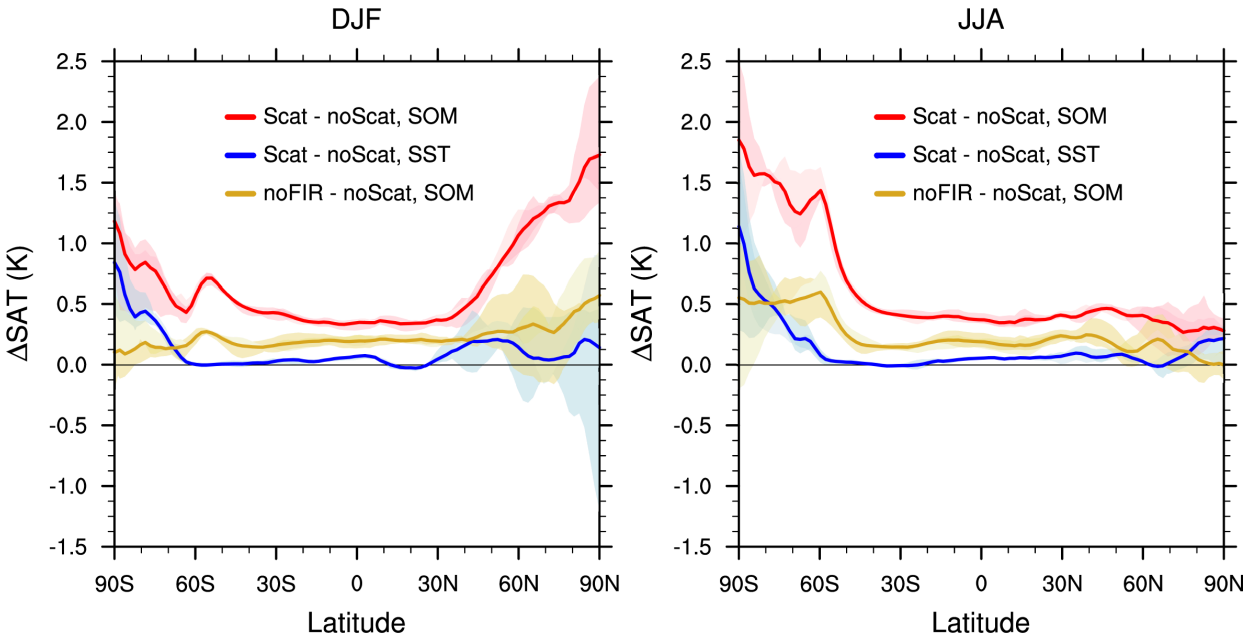

Fig. 3.4. (Left panel) The changes of boreal winter (December to February, DJF) zonal-mean surface air temperature (ΔSAT) due to inclusion of ice cloud LW scattering in the CESM. The ensemble-mean difference between the Scat and noScat for the SOM runs is shown in red, and the spread of four ensemble members is shown in the shade of the same color. Blue curve and shade are for the same difference but from the prescribed-SST runs. Yellow curve and shade show the difference between the noFIR and noScat for the SOM runs. (Right panel) Same as the left one except for the austral winter (June to August, JJA). 30 years of simulations are used in the analysis.

Fig. 3.4 shows the impact of including ice cloud LW scattering on the simulated zonal-mean surface air temperature (SAT) climatology for December-January-February (DJF) and June-July-August (JJA) periods, respectively. When the SSTs and sea ice are prescribed in the simulations (blue lines), including LW scattering or not has little impact on simulated SAT except the southern hemisphere polar region. Such results are consistent with the traditional wisdom that the LW scattering matters little in the prescribed-SST simulations. The simulated SAT difference (ΔSAT) south of 60^{o}S is notable due to the fact that the Antarctic continent covers the majority of the region and

the land surface temperature can respond to the changes caused by enabling ice cloud LW scattering in the prescribed-SST runs. Over the Arctic, the ensemble-mean ΔSAT is nearly zero but the ΔSAT of an individual member can be either positive or negative. This indicates that, when the SSTs and sea ice are prescribed, including ice cloud LW scattering or not behaves as a noisy perturbation in the simulated Arctic climate. Therefore, the ensemble-mean difference is not statistically different from zero.

However, the zonal-mean SAT difference due to ice cloud LW scattering for the SOM runs is positive everywhere and for all ensemble members, as shown in Fig. 3.4. The ensemble spread of such difference is well separated from its counterparts from the prescribed-SST runs. The SAT increase due to the inclusion of LW scattering in the tropics and mid-latitude is ~0.5K for both DJF and JJA periods. The ensemble mean ΔSAT in the Arctic winter is ~1.8K, 3-5 times larger than it in the Arctic summer (~0.3K), and all ensemble members show a consistent increase of SAT. Such large contrast between the Arctic summer and winter ΔSAT can be understood in two folds: (1) the large variation of Arctic TCWV from summer to winter as mentioned above, less TCWV in the winter implying stronger LW scattering effect; (2) moreover, the absence of SW radiation in the polar winter, as well as reduced surface turbulent heat flux due to extensive sea ice coverage, imply that the LW radiation plays the decisive role in regulating the SAT [Serreze and Barry 2005; Overland and Guest 1991]. In contrast to winter, SW radiation plays a lead role in the summer Arctic surface energy balance. Moreover, snow and ice melting in the summer consume surface energy residue, further reducing energy available to increase surface temperature. Also, during winter, the boundary layer in the Arctic is shallow and featured with strong temperature inversion,

which implies the anomalies in surface energy flux tend to affect the surface temperature rather than the atmosphere. A similar contrast between winter and summer SAT change can also be seen in the Antarctic, though not as large as it in the Arctic.

Yellow curves (noFIR – noScat runs) in Fig. 3.4 show the impact on zonal-mean SAT when ice cloud scattering is turned off in the far-IR but still on the mid-IR. The yellow curves are in the middle between red and blue curves over the extra-polar regions, suggesting that the mid-IR scattering contributes to about half of total ΔSAT. The mid-IR scattering primarily results from window regions, where gaseous absorption is weak. However, for both Arctic and Antarctic winter, the SAT change in the noFIR run is much smaller than the change in the Scat run, indicating the dominant contribution of far-IR scattering to the total scattering effect in terms of the SAT changes. Such contrast of the role of ice cloud far-IR scattering between polar winter and extra-polar regions can be largely understood using Eq. (1) and is primarily due to the drastic difference in the TCWV (and hence gaseous optical depth) between the extra-polar regions and the polar winter. It is also partly due to the increasing importance of far-IR contribution to the LW radiation from tropics to polar regions (Fig. 3.2b), an inference from Wien's Displacement Law.

3.3.2 The ice cloud LW scattering effect on the Arctic

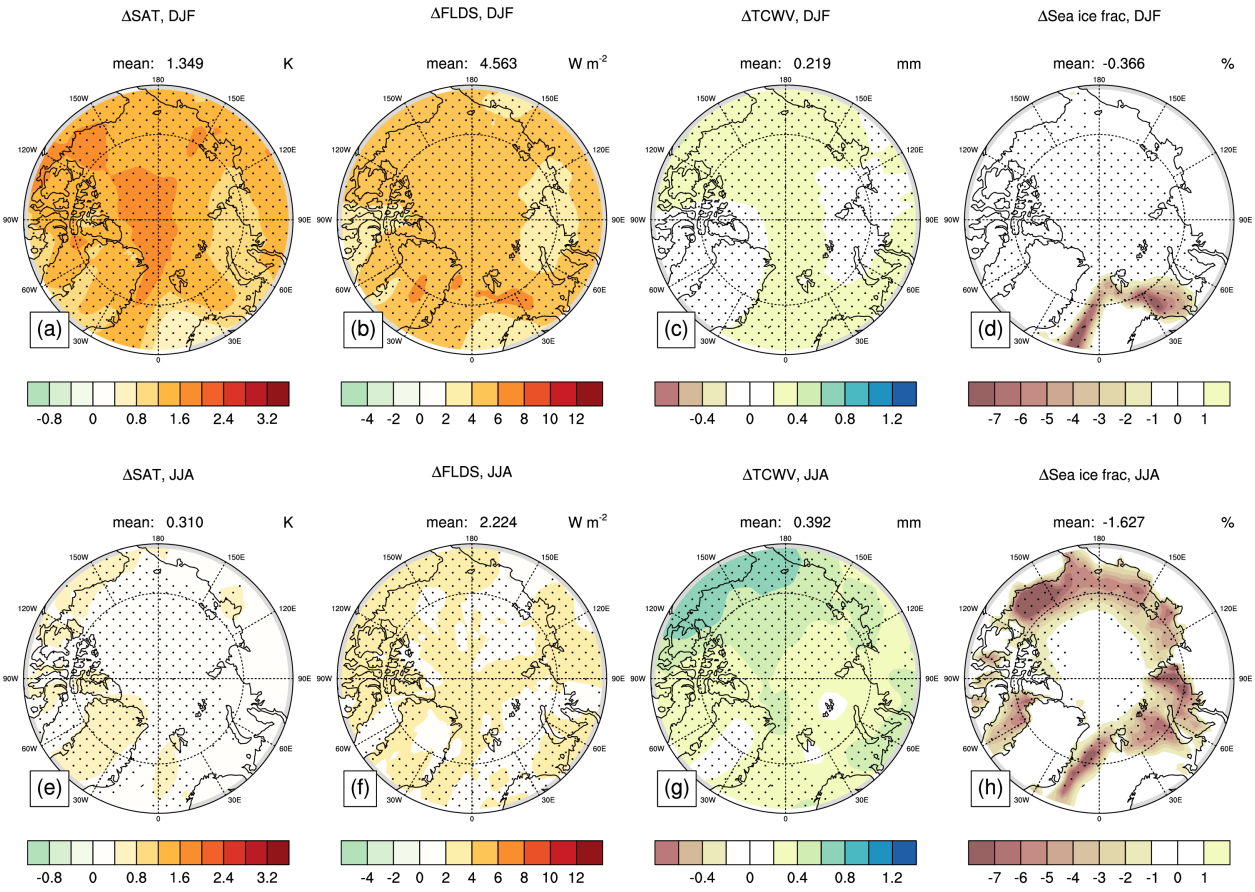

Fig. 3.5 The spatial maps of the ensemble-mean differences between the Scat and noScat for the SOM runs. (a,e) the SAT differences, (b,f) the FLDS difference, (c,g) the TCWV difference, and (d,h) the sea ice fraction difference. The DJF climatological differences are shown on the top row and the JJA counterparts are on the bottom row.

We further examine the ice cloud LW scattering effects in the Arctic. Figure 3.5 shows the spatial map of the differences between Scat and noScat for several variables in the SOM runs. In wintertime (Fig. 3.5a-d), the increases of SAT and FLDS due to ice cloud LW scattering are uniform across the entire Arctic domain. The increase of wintertime TCWV scales with the absolute value of TCWV, that is why ΔTCWV over Greenland is smaller than that over the surrounding area. Compared to the wintertime, the changes in the SAT and FLDS are much smaller in the summertime (Fig. 3.5e and

f), while the changes in the TCWV are larger in the summertime because the absolute value of TVWV in summertime is larger than wintertime. Another notable feature is that, over the summertime, even though ΔSAT is small for the Arctic Ocean, the change of sea ice fraction is statistically significant. Such change of sea ice fraction might be an accumulated effect: increased SAT through the winter and spring, as well as increased FLDS in the summer, both work towards the reduction of sea ice in the summertime

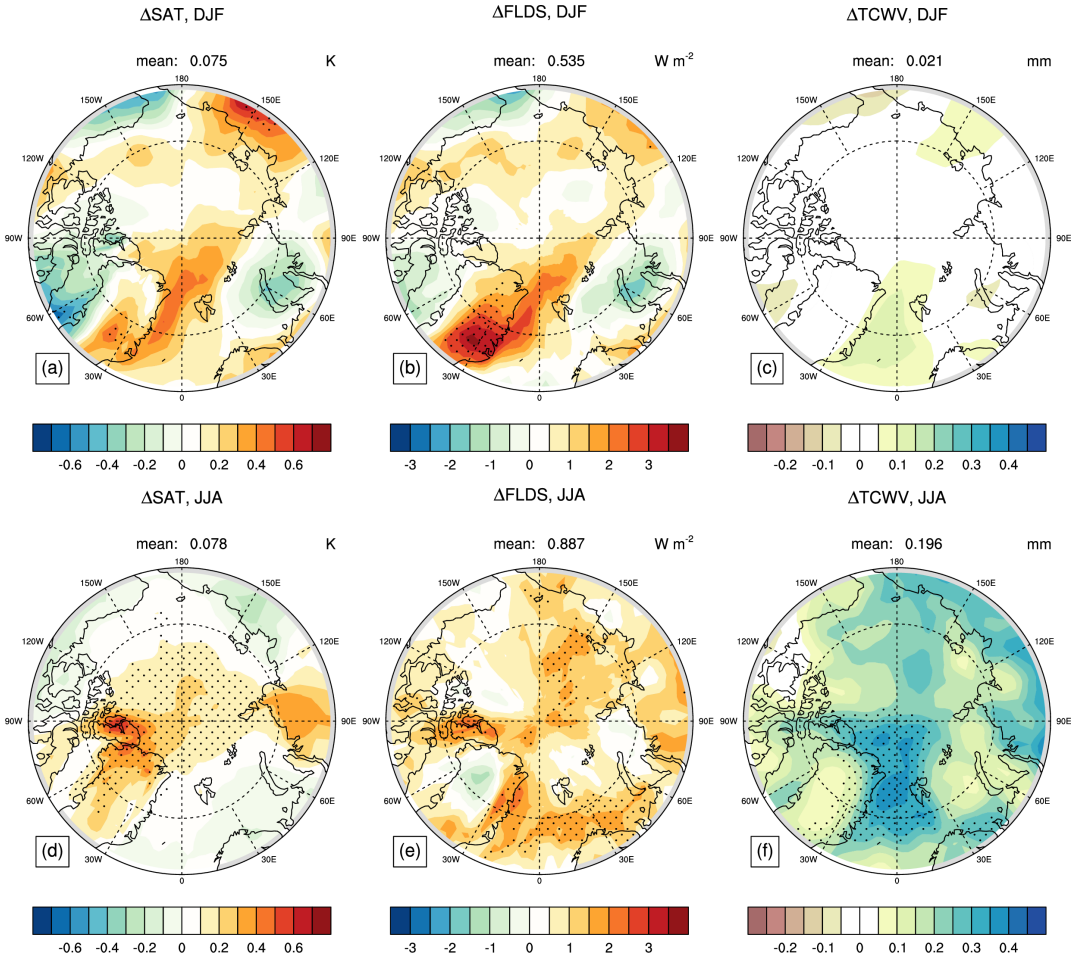

Fig 3.6. Same as Fig. 3.5 but for the SST runs. The ice fraction is excluded because the prescribed-SST runs prescribe the sea ice fraction, there is no any differences between the Scat and noScat.

Similar to Fig. 3.5, we examine the scattering effect in the prescribed-SST runs, as shown in Fig. 3.6. The difference in sea ice fraction is excluded in Fig. 3.6 because

these runs prescribe the SSTs and sea ice fraction, sea ice fraction remains the same for both Scat and noScat experiments. Compared to the SOM runs, the prescribed-SST runs have much smaller differences in wintertime SAT, FLDS, and TCWV, and most of them are not statistically significant (Fig. 3.6a-c). Because the majority of the Arctic is covered by sea ice or ocean, and the sea ice fraction and SSTs are not allowed to change in the prescribed-SST runs, these can exhibit the LW radiative coupling between the surface and atmosphere, resulting in small changes in the SAT, FLDS and TCWV responding to the cloud LW scattering effect. In summertime, the differences induced by cloud LW scattering are small as well.

In order to see how the ice cloud LW scattering effect influences the energy budget in the Arctic wintertime, we perform the Arctic domain-averaged (66.5^{o}N to 90^{o}N) energy budget analysis in DJF at the surface and the TOA, as shown in Fig. 3.7. The TOA energy budget shows minimal changes in response to the scattering effect in all experiments. Inspecting the surface energy budget, the scattering effect in the prescribed-SST runs shows minimal changes with large internal variability. For example, the scattering effect increases the ensemble-mean, Arctic domain-averaged SAT by 0.07K with a standard deviation of 0.25 among four members. The scattering effect in the SOM runs, in contrast, shows large changes in SAT with a small standard deviation (1.35±0.13K). Examining each term in the surface energy budget, it becomes clear that the increase in SAT in the SOM runs is mainly due to the increase in downward LW flux at the surface (+4.56 Wm^{-2}), as the changes in SW fluxes, latent heat, and sensible heat fluxes are minimal, less than 0.5 Wm^{-2}. The increase in downward LW flux at the surface is largely attributed to the clear-sky part, which

contributes roughly 80% of this increase. When the cloud scattering in the far-IR is turned off, the scattering effect on the SAT becomes much smaller with large standard deviation (0.34±0.27K), indicating that far-IR scattering has a dominant contribution to the total scattering effect in the Arctic wintertime.

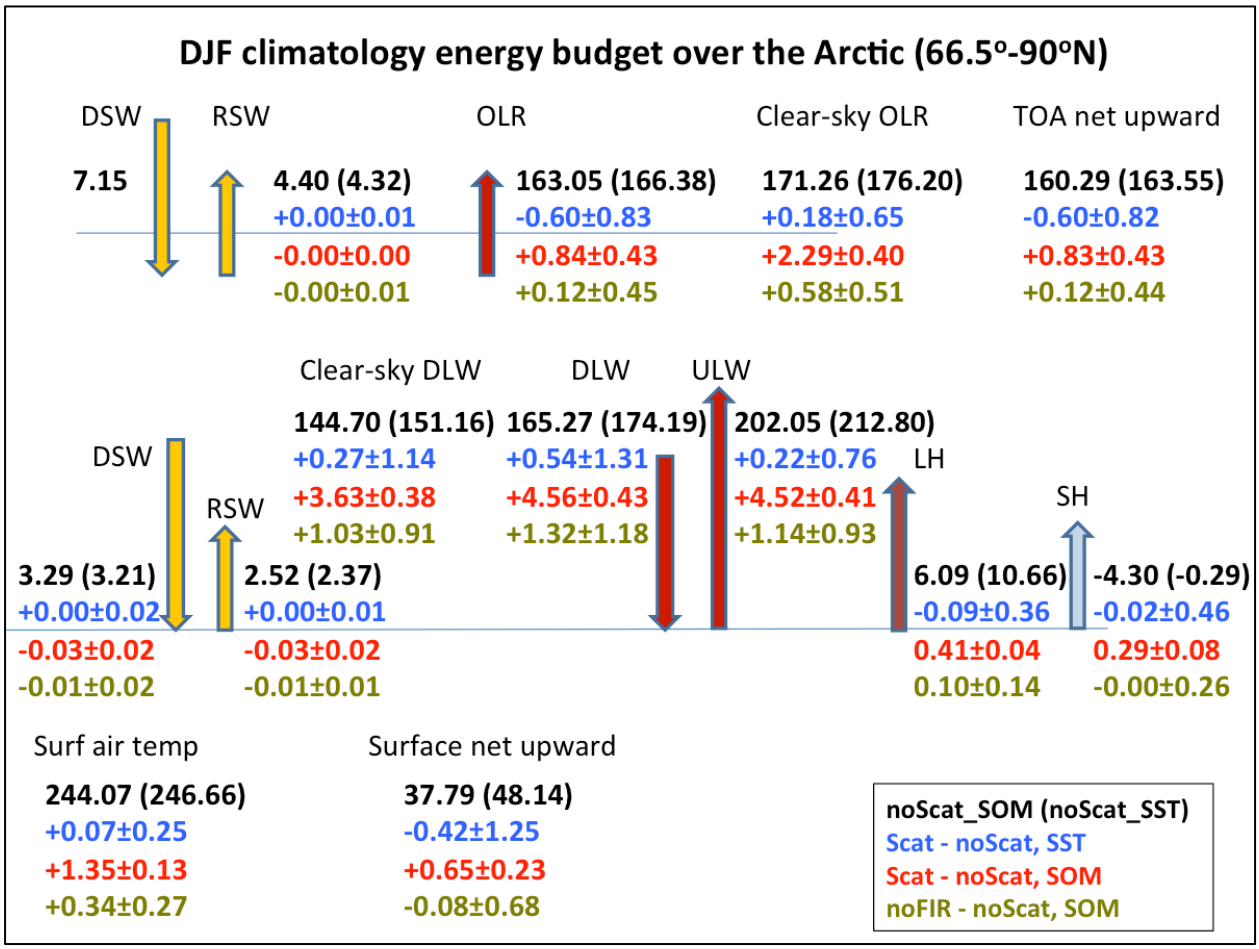

Fig. 3.7. The DJF climatology, Arctic domain-average (66.5°-90°N) energy budget at the TOA and the surface. Values in black are the ensemble mean of the noScat experiment for the SOM and prescribed-SST runs, the latter is enclosed by parenthesis. Values in blue show the Scat-noScat differences for the prescribed-SST run. Values in red show the Scat-noScat differences for the SOM runs. Values in gold show the noFIR-noScat differences between for the SOM run. The standard deviation of four ensemble members is also shown. DSW means downward SW flux, RSW means reflected SW flux, DLW means downward LW flux, ULW means upward LW flux, LH means latent heat flux, SH means sensible heat flux.

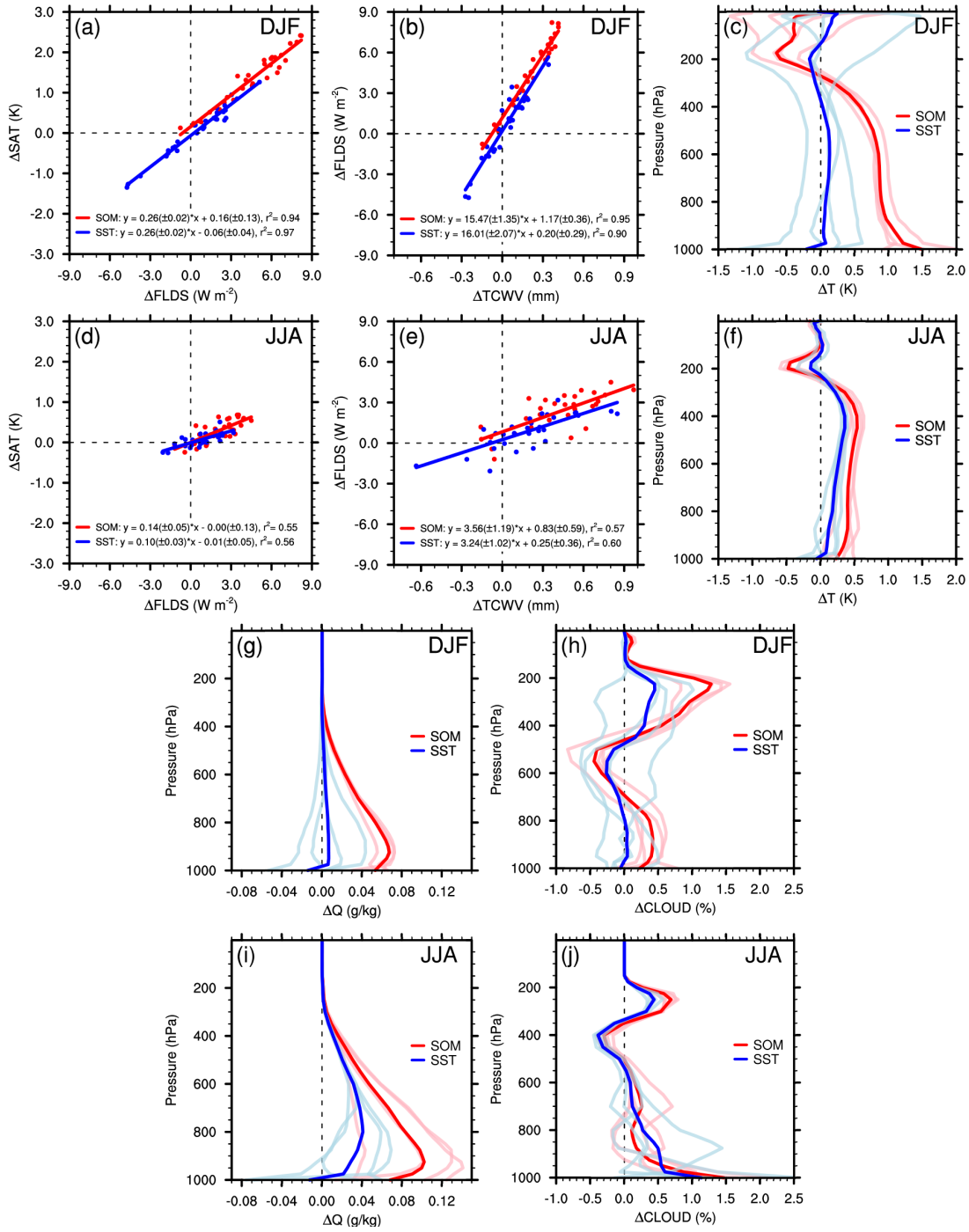

Fig. 3.8. (a) Ensemble-mean, Arctic domain-averaged Scat-noScat difference of SAT (ΔSAT) in DJF with respect to the difference of FLDS (ΔFLDS). Results from the SOM and prescribed-SST runs are plotted as red and blue dots, respectively. The linear regression lines are also plotted. The numbers in parentheses are 95% confidence intervals. (b) Same as (a) but for ΔFLDS with respect to ΔTCWV. (c) Difference in Arctic domain-averaged vertical temperature profiles for DJF, ensemble-mean results shown in thick colored lines and results from individual members in thin lightly colored lines. (d,e,f) are the counterparts of (a,b,c) but for JJA. (g,i) Same as (c,f) but for difference in specific humidity. (h,j) Same as (c,f) but the difference in the vertical profiles of cloud amount.

Figure 3.8 includes a few key diagnostics to reveal the reasons behind the differences between the SOM and prescribed-SST runs in response to the ice cloud LW scattering effect. For both runs, the Arctic winter domain-averaged ΔSAT is well correlated with the difference in FLDS (ΔFLDS) caused by the ice cloud LW scattering. A linear regression can explain >90% of the variance in ΔSAT, and the linear regression slope is essentially the same for both the SOM and fixed SST runs (Fig. 3.8a). This is consistent with the dominant role of LW radiation in regulating wintertime SAT. Such good linear relations can also be found between ΔFLDS and ΔTCWV (Fig. 3.8b). The linear relations hold for each ensemble member as well (Fig. 3.9).

The ensemble-mean and Arctic-averaged DJF temperature vertical profile changes due to the LW scattering is negligible in the prescribed-SST run, so does the change of humidity profiles (Fig. 3.8c and 3.8g). However, the counterparts from the SOM runs are positive for all ensemble members and well separated from the prescribed-SST run results. The change of cloud amount vertical profile, however, is ~1% or even less, and the results from the prescribed-SST and SOM runs are not well separated from each other (Fig. 3.8h). These results suggest that the contrast of Arctic DJF ΔSAT between the SOM and prescribed-SST runs is not primarily due to in-situ cloud field change. Instead, it is due to a LW feedback mechanism with surface involved: the inclusion of LW scattering leads to an increase of FLDS, which in the wintertime alters the surface energy budget significantly and leads to an increase of surface temperature over the entire Arctic. Such increase of surface temperature leads to an increase of atmospheric temperature and of the humidity in the troposphere, which further increases the downward LW flux and forms a positive feedback. Such feedback

mechanism is particularly effective in the winter because the summer surface temperature can be affected by multiple factors in addition to FLDS thus the linear regression can only explain ~56% of ΔSAT variances (Fig. 3.8d).

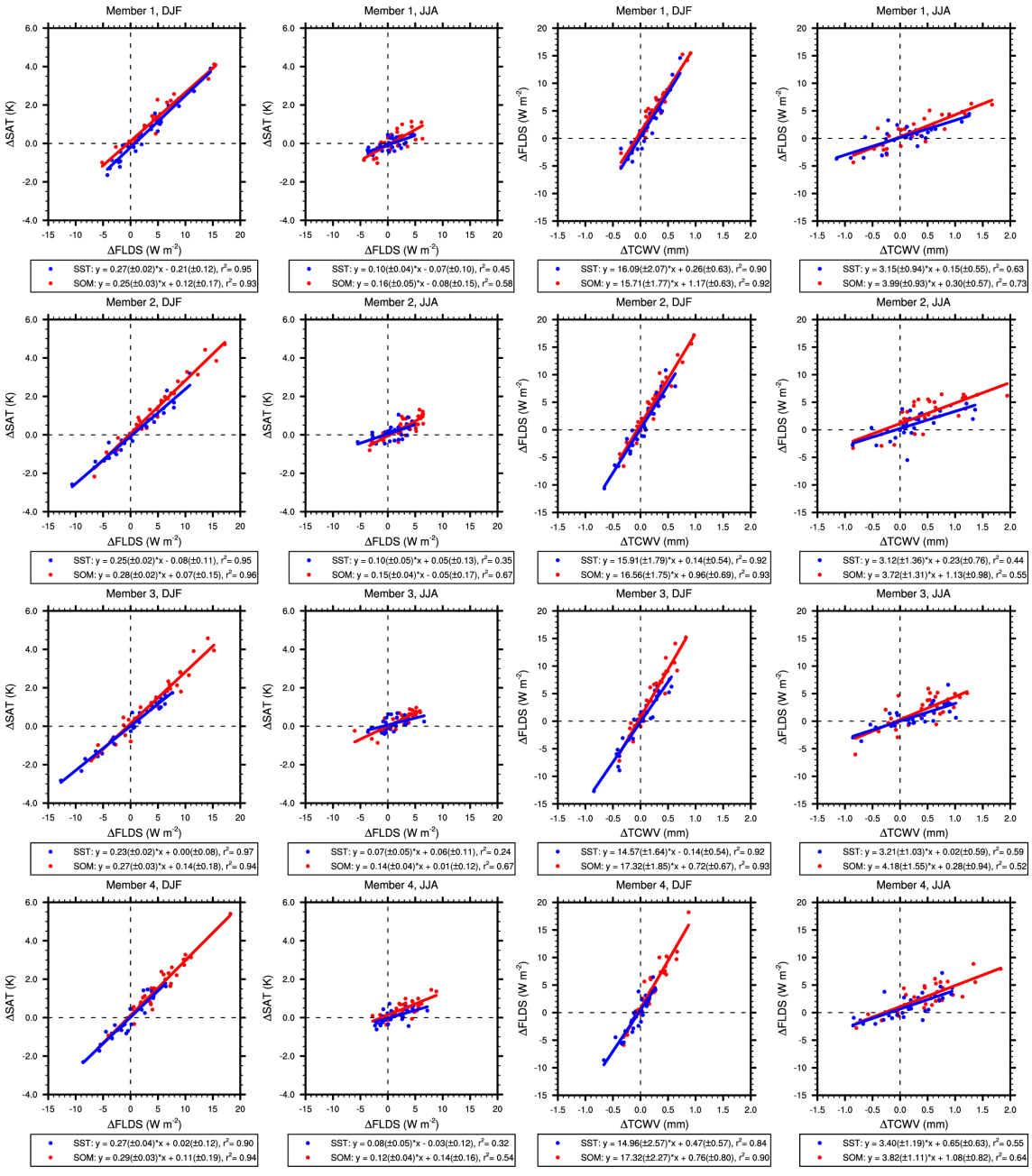

Fig 3.9. (First and second columns) Arctic domain-averaged Scat-noScat difference of SAT (ΔSAT) with respect to the difference of FLDS (ΔFLDS) as caused by the inclusion of ice cloud LW scattering for four ensemble members. The first column shows the results in DJF and the second column shows the results in JJA. Each row represents different ensemble member. (Third and fourth columns) Same as the first and second columns but for ΔFLDS and ΔTCWV.

To corroborate the aforementioned mechanism, we perform a domain-averaged analysis to quantify the contributions of atmosphere-surface LW radiative coupling to the simulated cloud LW scattering impact. The Arctic-averaged ΔTCWV due to ice cloud LW scattering is 0.02cm in the prescribed-SST run but 0.22cm in the SOM run (Table 3.1), i.e. allowing surface-atmosphere coupling amplifies the effect of LW cloud scattering on the simulated TCWV by a factor of 10. A similar large contrast between the prescribed-SST and SOM runs can be seen for the ΔFLDS as well. Such large contrasts are consistent with Fig. 3.8 and corroborate the need of considering surface and atmospheric LW coupling in order to assess the full impact of ice cloud LW scattering, a physical process that has been usually evaluated using the prescribed-SST runs.

Table 3.1. Arctic domain-averaged analysis of the changes (Δ) caused by the inclusion of ice cloud LW scattering. Linear regression coefficients are given with 95% confidence intervals. The numbers in parentheses are fraction of variance explained by the linear regression. In the last column, the results based on the regressions of the Prescribed-SST and SOM runs are in blue and red, respectively.

$\Delta FLDS = \beta_1 \Delta TCWV + c_1$; $\Delta SAT = \beta_2 \Delta FLDS + c_2$; $\Delta SAT = \beta_3 \Delta TCWV + c_3$				
	Prescribed-SST	SOM	δ Difference (SOM - Prescribed-SST)	Estimated difference
β_1	**16.0±2.1 (90.0%)**	**15.5±1.3 (95.2%)**		
β_2	**0.26±0.02 (97%)**	**0.26±0.02 (94%)**		
β_3	**4.02±0.73 (82%)**	**3.95±0.61 (86%)**		
ΔT_{700} (K)	**0.11**	**0.88**	**0.77**	
ΔTCWV (cm)	**0.021**	**0.22**	**0.20**	
ΔFLDS (Wm^{-2})	**0.53**	**4.56**	**4.03**	δ(ΔFLDS) = β_1δ (ΔTCWV) **3.2±0.41** **3.1±0.26**
ΔSAT (K)	**0.075**	**1.35**	**1.27**	δ(ΔSAT) = β_1 β_2δ (ΔTCWV) **0.83±0.06** **0.81±0.06** δ(ΔSAT) = β_3δ (ΔTCWV) **0.80±0.15** **0.79±0.12**

Since the prescribed-SST run does not have surface-atmosphere LW coupling whether the cloud scattering is included or not, we use the contrast between the prescribed-SST and SOM runs to assess the LW coupling between atmosphere and surface. The change of TCWV is highly correlated with the change of atmospheric temperature. For example, the correlation between ΔTCWV and ΔT_{700hPa} is 0.96 in the prescribed-SST run and 0.95 in the SOM run. To avoid collinearity due to correlated variables, we use ΔTCWV as the *sole* linear predictor to represent the change of clear-sky atmospheric state and estimate ΔFLDS and ΔSAT with linear regression, i.e.,

$$\Delta FLDS = \beta_1 \Delta TCWV + c_1, \quad (3.2)$$

$$\Delta SAT = \beta_2 \Delta FLDS + c_2, \quad (3.3)$$

$$\Delta SAT = \beta_3 \Delta TCWV + c_3. \quad (3.4)$$

The regression coefficients are derived from the prescribed-SST and SOM runs, respectively, and shown in Table 3.1 using the same notation as above. Table 3.1 shows that, in any cases, the linear regressions can explain at least 82% of the total variance and the linear regression slopes derived from both runs are highly consistent with each other.

If we denote the difference in ΔTCWV between the SOM and prescribed-SST runs as $\delta(\Delta TCWV)$, i.e., the difference due to the surface-atmospheric LW radiative coupling, then the difference in ΔFLDS and ΔSAT due to such coupling can be estimated as $\delta(\Delta FLDS) = \beta_1 \delta(\Delta TCWV)$, $\delta(\Delta SAT) = \beta_3 \delta(\Delta TCWV)$ or $\delta(\Delta SAT) = \beta_2 \beta_1 \delta(\Delta TCWV)$. Such estimated results are shown in the rightmost column of Table 3.1. The estimates based on regressions from the SOM and prescribed-SST runs are highly consistent with each other. 3.2 out of 4.03 Wm^{-2} total difference in ΔFLDS

and 0.8 out of 1.27K total difference in ΔSAT can be explained by the linear regression relations with respect to ΔTCWV. This supports our explanation that the differences in clear-sky atmospheric features between the prescribed-SST and SOM runs contribute the most to the differences in SAT in response to ice cloud LW scattering.

3.3.3 The ice cloud LW scattering effect on the Antarctic

We now turn to examine the ice cloud LW scattering effect in the Antarctic. Figure 3.10 shows the spatial map of the ensemble-mean differences between Scat and noScat for the SOM runs. In wintertime (JJA), the scattering effect increases the SAT, FLDS, and TCWV uniformly across the entire Antarctic domain. Unlike the Arctic, these increases in the summertime (DJF) are still prominent and statically significant, though the magnitudes are smaller than the wintertime counterparts. This is because in the summertime, the TCWV is still small enough over the Antarctic owing to the high elevation of the Antarctic continent, which allows the scattered LW radiation to reach the surface and then increase the SAT.

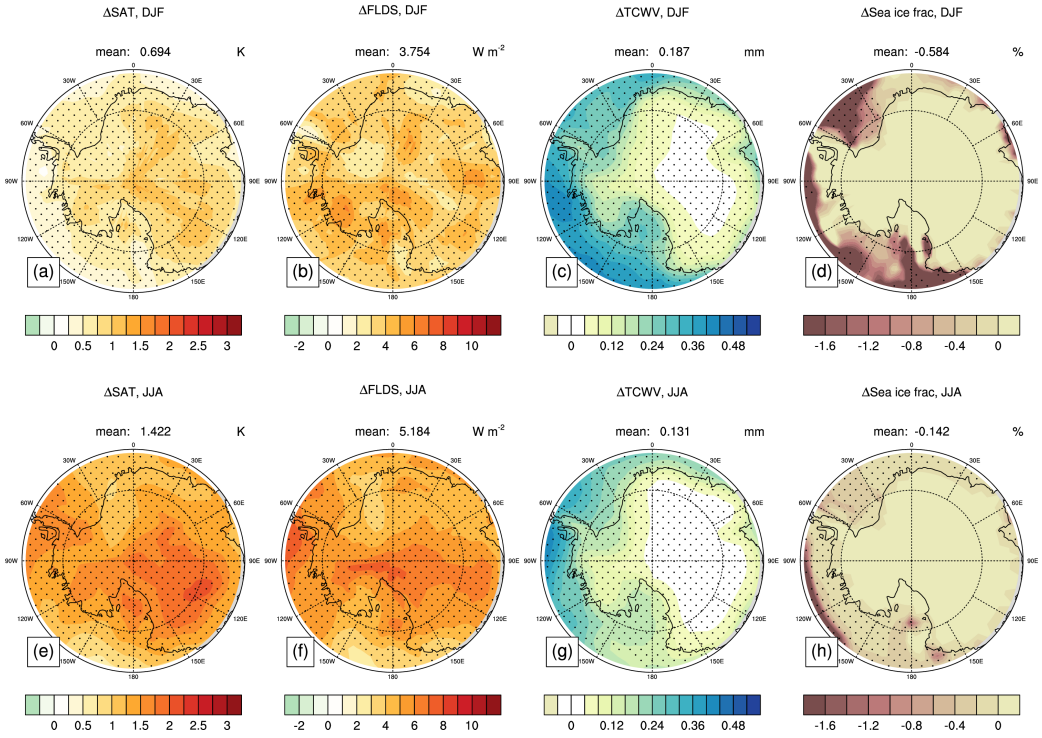

Fig. 3.10 Same as Fig. 3.5 but for the Antarctic.

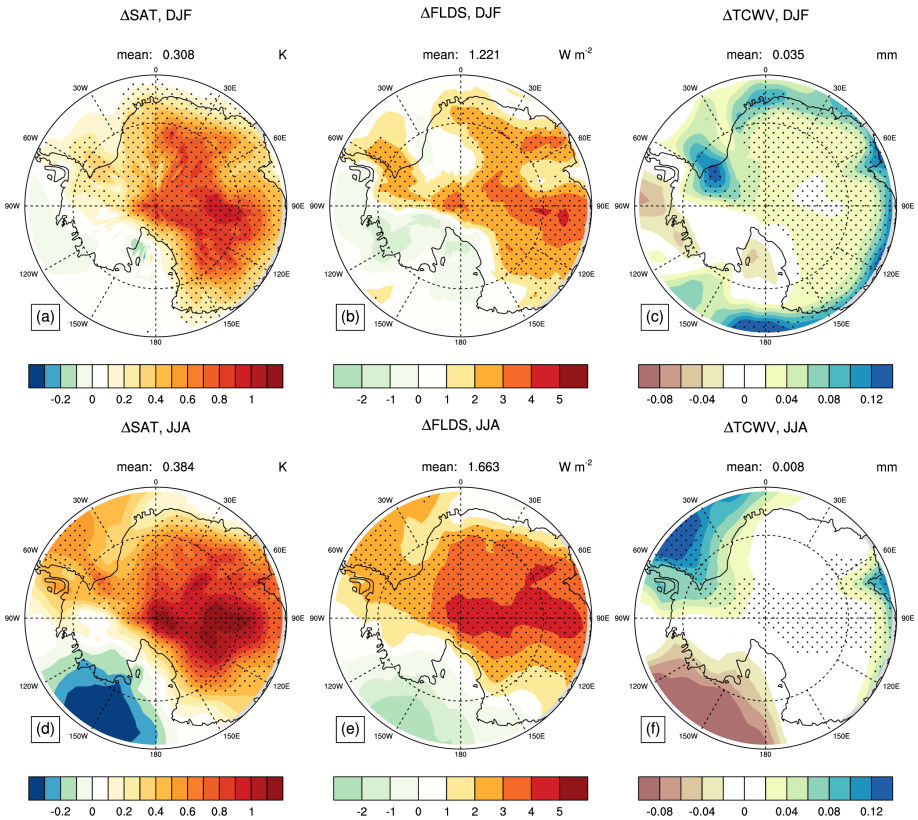

Fig. 3.11 Same as Fig. 3.6 but for the Antarctic.

The scattering effect in the prescribed-SST runs is examined in Fig. 3.11. The scattering effect increases the SAT, FLDS, and TCWV mainly over the Antarctic continent and these increases are larger in wintertime (JJA) than summertime (DJF), similar to the results in the SOM runs but the magnitudes are smaller. In contrast to the Arctic in which the scattering effect is weak in the prescribed-SST run (Fig. 3.6), the scattering effect is decent over the Antarctic. This is because over the Antarctic continent, the LW radiative boundary condition is determined by surface energy processes, not prescribed. As a result, the SAT can respond to the changes in FLDS. This explanation is also supported by the small changes in SAT over the ocean grids around the Antarctic continent, in which the SSTs and sea ice fraction are prescribed so that the SAT shows minimal changes.

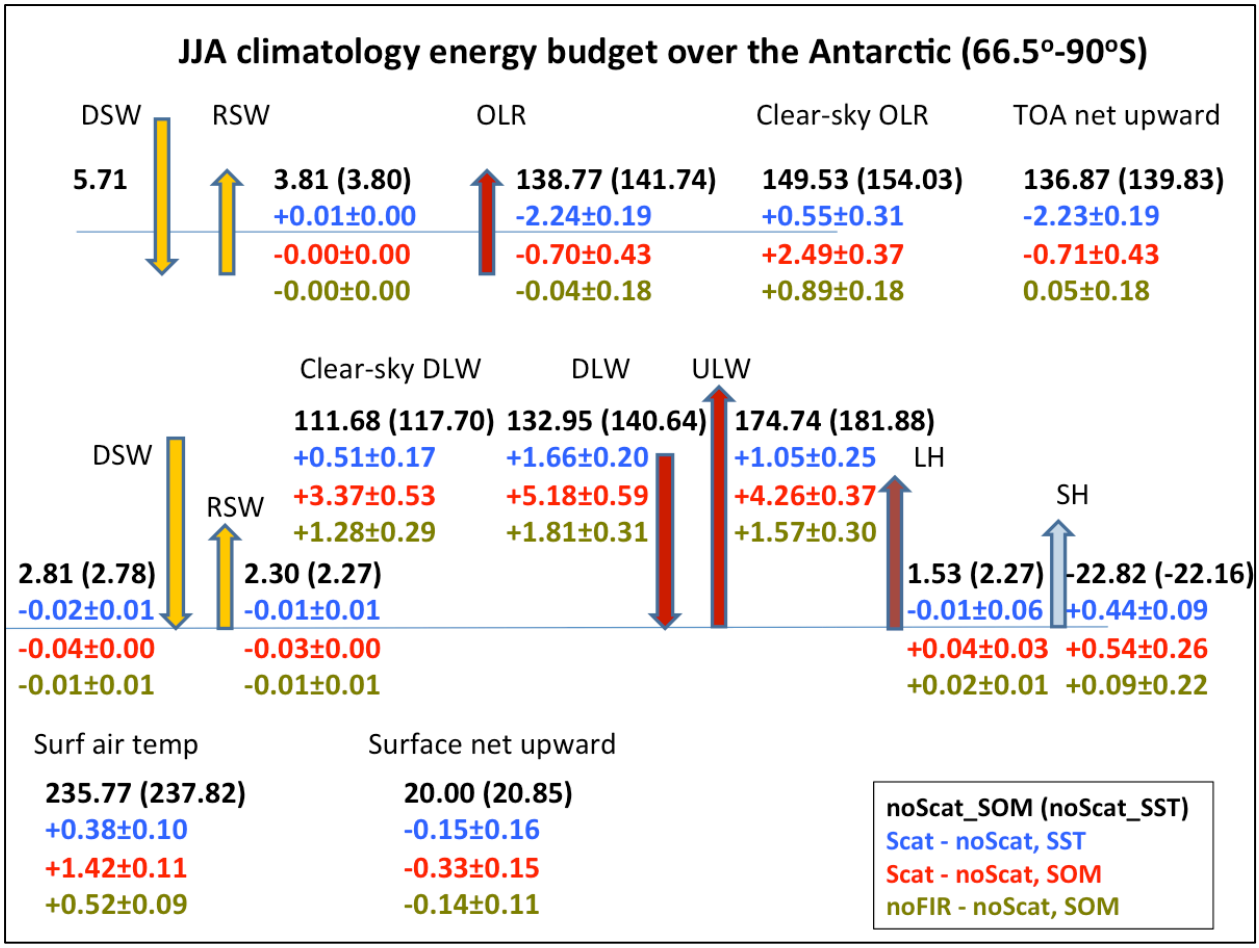

Fig. 3.12 Same as Fig. 3.7 but for the Antarctic (66.5-90°S).

In order to see how the ice cloud LW scattering effect affects the energy budget in the Antarctic JJA, we perform the Antarctic domain-averaged (66.5°S to 90°S) energy budget analysis at the surface and the TOA, as shown in Fig. 3.12. At the TOA, the scattering effect induces approximately 2 Wm^{-2} difference between the all-sky OLR and clear-sky OLR for both the prescribed-SST and SOM runs, indicating some changes in cloud properties due to the scattering effect. At the surface, because other energy terms exhibit minimal changes, the increase in FLDS is mainly balanced by the upward LW flux at the surface, which is consistent with what we have seen in the Arctic surface energy budget. Similarly, the increase in FLDS in the SOM run is mainly from clear-sky

part while in the prescribed-SST runs, only 31% increase in the FLDS is from the clear-sky part. This indicates that in the prescribed-SST run, the changes in cloud is primarily responsible to the FLDS increase. When the scattering from the far-IR bands is turned off, the resulting scattering effects become much weaker, implying the importance of scattering in the far-IR band in the Antarctic.

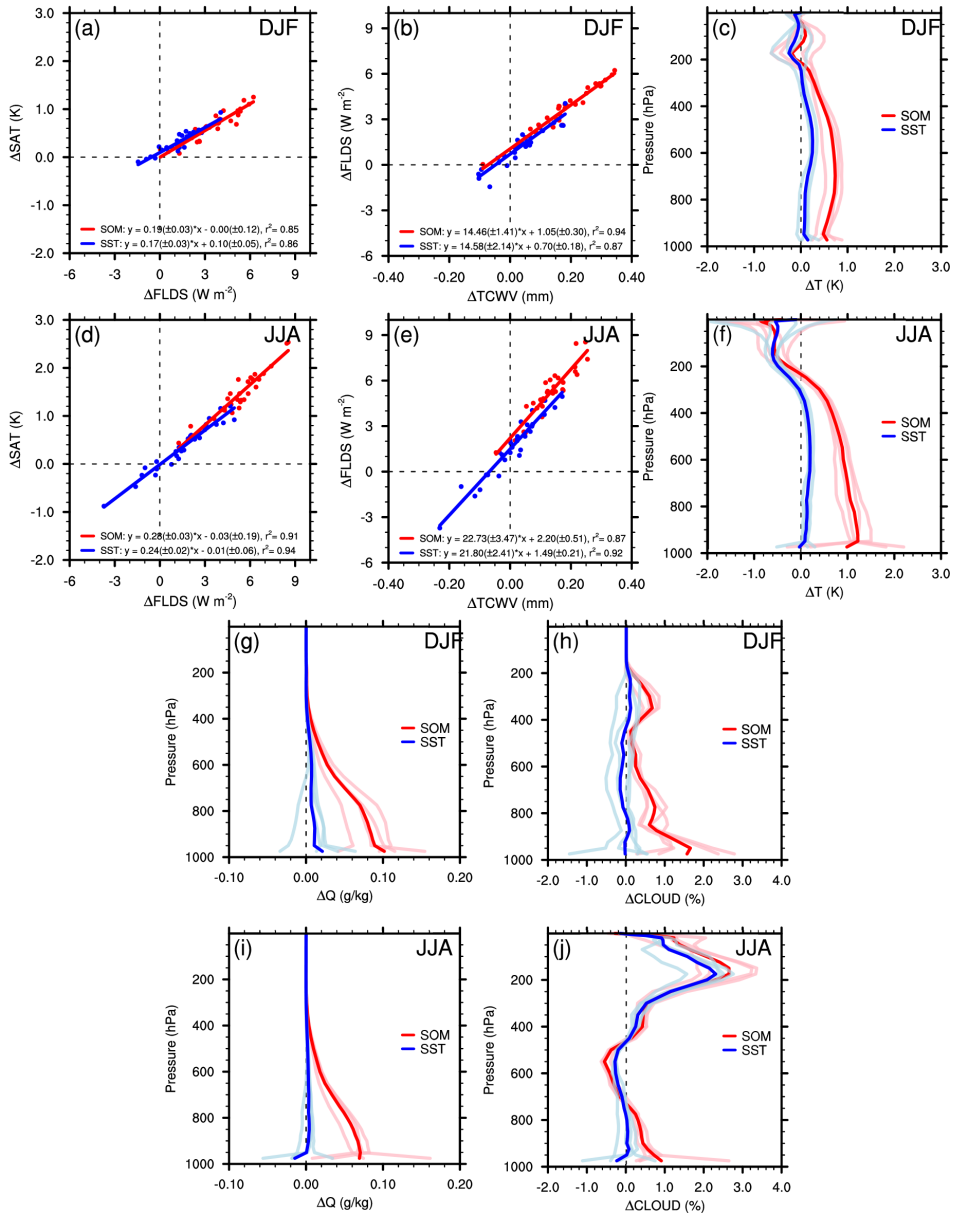

Fig. 3.13 Same as Fig. 3.8 but for the Antarctic.

To reveal the importance of surface-atmosphere LW coupling effect over the Antarctic winter, we perform a similar analysis as what we have done for the Arctic, shown in Fig. 3.13, 3.14, and Table 3.2. Conclusions gained from the Arctic are largely applicable to the Antarctic. First, the winter Antarctic domain-averaged ΔSAT is well correlated with the difference in FLDS (ΔFLDS) caused by the ice cloud LW scattering. A linear regression can explain >90% of the variance in ΔSAT, and the linear regression slope is essentially the same for both the SOM and prescribed-SST runs (Fig. 3.13d). This is consistent with the dominant role of LW radiation in regulating wintertime SAT. Such good linear relations can also be found between ΔFLDS and ΔTCWV (Fig. 3.13e). Unlike the Arctic, ΔSAT, ΔFLDS, and ΔTCWV still have good correlations during summertime (Fig. 3.13a and b), implying that the FLDS still plays an important role in the surface energy process. This is probably because in summertime, the surface albedo is sufficiently high, weakening the role of SW radiation in the surface energy processes. Also, the latent heat flux is small in the Antarctic as the majority of the surface area is covered by ice or snow instead of water. Second, in the prescribed-SST runs, the LW scattering effect induces minimal changes in the ensemble-mean and Antarctic-averaged temperature vertical profile for both DJF and JJA (Fig. 3.13c and f), as well as the humidity profiles (Fig. 3.13g and i). In contrast, the counterparts from the SOM runs are positive for all ensemble members and well separated from the prescribed-SST run results. Lastly, the change of cloud amount vertical profile is ~3% or even less, and the results from the prescribed-SST and SOM runs are not well separated from each other (Fig. 3.13h and j). These results suggest that the contrast of

ΔSAT in Antarctic JJA between the SOM and prescribed-SST runs is not primarily due to in-situ cloud field change.

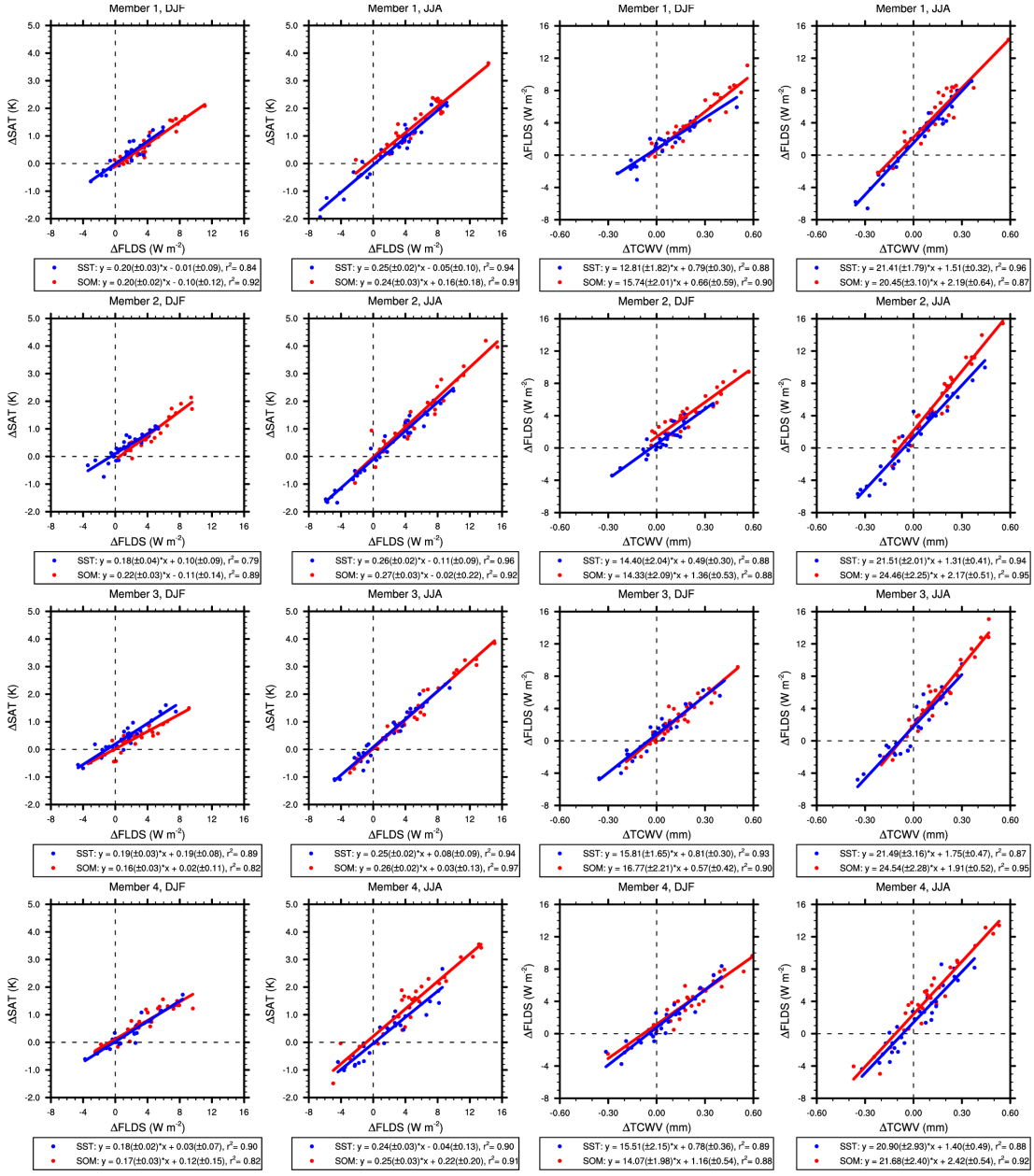

Fig 3.14. Same as Fig. 3.9 but for the Antarctic.

We also perform linear regression to estimate the surface-atmospheric LW radiative coupling in the Antarctic. The regression coefficients are shown in Table 3.2. Like the Arctic, the estimates based on the regressions results from the SOM and

prescribed-SST runs are highly consistent with each other and can be used to explain the SAT differences between these two runs. The linear regression relations with respect to ΔTCWV can explain 2.7 out of 3.52 Wm^{-2} total difference in ΔFLDS and 0.7 out of 1.03K total difference in ΔSAT. Like the Arctic, this supports our explanation that the differences in clear-sky atmospheric features between the prescribed-SST and SOM runs in response to ice cloud LW scattering contribute the most to the differences in SAT.

Table 3.2. Same as Table 3.1 bur for Antarctic ensemble-mean results in JJA.

$\Delta FLDS = \beta_1 \Delta TCWV + c_1$; $\Delta SAT = \beta_2 \Delta FLDS + c_2$; $\Delta SAT = \beta_3 \Delta TCWV + c_3$				
	Prescribed-SST	SOM	δ Difference (SOM - Prescribed-SST)	Estimated difference
β_1	**21.8±2.4 (92.5%)**	**22.8±3.5 (86.6%)**		
β_2	**0.23±0.02 (94%)**	**0.28±0.03 (91%)**		
β_3	**4.95±0.98 (79%)**	**5.95±1.56 (69%)**		
ΔT_{700} (K)	**0.20**	**0.90**	**0.70**	
ΔTCWV (cm)	**0.008**	**0.13**	**0.12**	
ΔFLDS (Wm^{-2})	**1.66**	**5.18**	**3.52**	δ(ΔFLDS) = β_1δ (ΔTCWV) **2.6±0.29** **2.7±0.42**
ΔSAT (K)	**0.38**	**1.42**	**1.03**	δ(ΔSAT) = β_1 β_2δ (ΔTCWV) **0.60±0.05** **0.77±0.08** δ(ΔSAT) = β_3δ (ΔTCWV) **0.59±0.12** **0.71±0.19**

3.4 Concluding remarks

As ice cloud LW scattering is missing in a dominant majority of climate models, recently the inclusion of ice cloud LW scattering in the climate models has received certain attention [Wu et al. 2019; Zhao et al. 2018; Jin et al. 2019], but all relevant

studies have been conducted using prescribed-SST type simulations. Although the inclusion of cloud LW scattering enhances the LW absorptions by the climate system, we show that, without the surface-atmosphere radiative coupling, such enhanced LW absorption alone has limited impact on the simulated climate. When such coupling is allowed, its impact on the polar surface climate can be manifested through a positive feedback between the atmosphere and surface, causing considerable differences in the simulated surface climate. Such impact is seasonably dependent, due to the role played by LW radiation in regulating surface energy budget. The contrast between the prescribed-SST and SOM runs supports such findings and the domain-averaged energy budget analysis further confirms the feedback mechanisms. Our results also show that the scattering in the far-IR bands dominates the impact of ice cloud LW scattering on the simulated polar surface climate, highlighting the importance of far-IR radiation to the polar climate.

Methodology wise, while the parameterization of atmospheric physical processes is usually developed and assessed using the atmospheric model alone, our study serves as an example to stress two points: (1) the need of using coupled simulations to assess different parameterizations of atmospheric processes and (2) a parameterization scheme applicable to one climate zone might not be equally applicable to other climate zones.

References

Baum, B. A., P. Yang, A. J. Heymsfield, C. G. Schmitt, Y. Xie, A. Bansemer, Y. X. Hu, and Z. Zhang, 2011: Improvements in shortwave bulk scattering and absorption models for the remote sensing of ice clouds. J. Appl. Meteorol. Climatol., 50, 1037–1056, doi:10.1175/2010JAMC2608.1.

Ceppi, P., F. Brient, M. D. Zelinka, and D. L. Hartmann, 2017: Cloud feedback mechanisms and their representation in global climate models. Wiley Interdiscip. Rev. Clim. Chang., 8, e465, doi:10.1002/wcc.465. http://doi.wiley.com/10.1002/wcc.403.

Chen, X. H., X. L. Huang, and M. G. Flanner, 2014: Sensitivity of modeled far-IR radiation budgets in polar continents to treatments of snow surface and ice cloud radiative properties. Geophys. Res. Lett., 41, 6530–6537, doi:10.1002/2014GL061216.

Edwards, J. M., and A. Slingo, 1996: Studies with a flexible new radiation code. I: Choosing a configuration for a large-scale model. Q. J. R. Meteorol. Soc., 122, 689–719, doi:10.1256/smsqj.53106.

Fu, Q., and K. N. Liou, 1993: Parameterization of the Radiative Properties of Cirrus Clouds. J. Atmos. Sci., 50, 2008–2025, doi:10.1175/1520-0469(1993)050<2008:POTRPO>2.0.CO;2.

Fu, Q., K. N. Liou, M. C. Cribb, T. P. Charlock, and A. Grossman, 1997: Multiple Scattering Parameterization in Thermal Infrared Radiative Transfer. J. Atmos. Sci., 54, 2799–2812, doi:10.1175/1520-0469(1997)054<2799:MSPITI>2.0.CO;2.

Gent, P. R., and Coauthors, 2011: The Community Climate System Model Version 4. J. Clim., 24, 4973–4991, doi:10.1175/2011JCLI4083.1.

Heymsfield, A. J., A. Bansemer, P. R. Field, S. L. Durden, J. L. Stith, J. E. Dye, W. Hall, and C. A. Grainger, 2002: Observations and Parameterizations of Particle Size Distributions in Deep Tropical Cirrus and Stratiform Precipitating Clouds: Results from In Situ Observations in TRMM Field Campaigns. J. Atmos. Sci., 59, 3457–3491, doi:10.1175/1520-0469(2002)059<3457:OAPOPS>2.0.CO;2.

Jin, Z., Y. Zhang, A. Del Genio, G. Schmidt, and M. Kelley, 2019: Cloud scattering impact on thermal radiative transfer and global longwave radiation. J. Quant. Spectrosc. Radiat. Transf., 239, 106669, doi:10.1016/j.jqsrt.2019.106669.

Kay, J. E., and Coauthors, 2015: The community earth system model (CESM) large ensemble project : A community resource for studying climate change in the presence of internal climate variability. Bull. Am. Meteorol. Soc., 96, 1333–1349, doi:10.1175/BAMS-D-13-00255.1.

Kristjánsson, J. E., J. M. Edwards, and D. L. Mitchell, 2000: Impact of a new scheme for optical properties of ice crystals on climates of two GCMs. J. Geophys. Res. Atmos., 105, 10063–10079, doi:10.1029/2000JD900015.

Kuo, C.-P., P. Yang, X. Huang, Y.-H. Chen, and G. Liu, 2020: Assessing the accuracy and efficiency of longwave radiative transfer models involving scattering effect with cloud optical property parameterizations. J. Quant. Spectrosc. Radiat. Transf., 240, 106683, doi:10.1016/j.jqsrt.2019.106683.

McClatchy, R. A., Fenn, R. W., Selby, J. E. A., Volz, F. E., and J. A. Garing, 1972: A Optical properties of the atmosphere, 3rd ed., AFGRL‐72–0497, 80 pp.

Mitchell, D. L., A. Macke, and Y. G. Liu, 1996: Modeling cirrus clouds .2. Treatment of radiative properties. J. Atmos. Sci., 53, 2967–2988, doi:Doi 10.1175/1520-0469(1996)053<2967:Mccpit>2.0.Co;2.

Mlawer, E. J., S. J. Taubman, P. D. Brown, M. J. Iacono, and S. A. Clough, 1997: Radiative transfer for inhomogeneous atmospheres: RRTM, a validated correlated-k model for the longwave. J. Geophys. Res. Atmos., 102, 16663–16682, doi:10.1029/97JD00237.

Neale, R. B., and Coauthors, 2010: Description of the NCAR community atmosphere model (CAM 4.0), NCAR Technical Note NCAR/TN-485 + STR, 2010. [Available online at https://www.cesm.ucar.edu/models/ccsm4.0/cam/docs/description/cam4_desc.pdf].

Overland, J. E., and P. S. Guest, 1991: The Arctic snow and air temperature budget over sea ice during winter. J. Geophys. Res., 96, 4651, doi:10.1029/90JC02264.

Pincus, R., H. Barker, and J. Morcrette, 2003: A fast, flexible, approximate technique for computing radiative transfer in inhomogeneous cloud fields. J. Geophys. Res., 108, 1–5, doi:10.1029/2002JD003322.

Platnick, S., and Coauthors, 2017: The MODIS Cloud Optical and Microphysical Products: Collection 6 Updates and Examples from Terra and Aqua. IEEE Trans. Geosci. Remote Sens., 55, 502–525, doi:10.1109/TGRS.2016.2610522.

Randall, D. A., 1989: Cloud parameterization for climate modeling: Status and prospects. Atmos. Res., 23, 345–361, doi:10.1016/0169-8095(89)90025-2.

Serreze, M. C., and Barry, R. G, 2005:. The Arctic Climate System. Cambridge University Press, 385 pp.

Stamnes, K., S.-C. Tsay, W. Wiscombe, and K. Jayaweera, 1988: Numerically stable algorithm for discrete-ordinate-method radiative transfer in multiple scattering and emitting layered media. Appl. Opt., 27, 2502, doi:10.1364/AO.27.002502.

Stephens, G. L., 2005: Cloud Feedbacks in the Climate System: A Critical Review. J. Clim., 18, 237–273, doi:10.1175/JCLI-3243.1.

Stephens, G. L., 1984: The Parameterization of Radiation for Numerical Weather Prediction and Climate Models. Mon. Weather Rev., 112, 826–867, doi:10.1175/1520-0493(1984)112<0826:TPORFN>2.0.CO;2.

Toon, O. B., C. P. McKay, T. P. Ackerman, and K. Santhanam, 1989: Rapid calculation of radiative heating rates and photodissociation rates in inhomogeneous multiple scattering atmospheres. J. Geophys. Res., 94, 287–301, doi:10.1029/JD094iD13p16287.

Wu, K., J. Li, J. Cole, X. Huang, K. von Salzen, and F. Zhang, 2019: Accounting for Several Infrared Radiation Processes in Climate Models. J. Clim., 32, 4601–4620, doi:10.1175/JCLI-D-18-0648.1.

Yang, P., K.-N. Liou, L. Bi, C. Liu, B. Yi, and B. A. Baum, 2015: On the radiative properties of ice clouds: Light scattering, remote sensing, and radiation parameterization. Adv. Atmos. Sci., 32, 32–63, doi:10.1007/s00376-014-0011-z.

Zhao, W., Y. Peng, B. Wang, and J. Li, 2018: Cloud longwave scattering effect and its impact on climate simulation. Atmosphere (Basel)., 9, 1–20, doi:10.3390/atmos9040153.

Chapter 4

Quantifying the Combined Effect of Surface Spectral Emissivity and Ice Cloud Longwave Scattering in High-Latitude Regions

4.1 Introduction

In recent decades, high-latitude regions in both hemispheres have shown many signs of changes. In the northern hemisphere, the Arctic has been warming at a rate approximately twice that of the global average (Richter-Menge et al. 2018). The Arctic sea ice extent is shrinking rapidly with the ten lowest extents since 1979 occurring in this 21st century (Parkinson and DiGirolamo 2016). In the southern hemisphere, surface temperature trends show significant warming over the Antarctic Peninsula (Mayewski et al. 2009; Turner et al. 2014). The Southern Ocean sea ice extent has expanded at a rate of 1.5% per decade since the late 1970s, but with large regional variations (Fan et al. 2014; Turner et al. 2015; Hobbs et al. 2016). The causes of these changes are not well understood, which also lowers the confidence in projections of future changes in the high-latitude regions.

General circulation models (GCMs) are essential tools to understand these changes and project future climate in the high-latitude regions. Current GCMs still struggle to simulate key features in these regions, such as surface energy budget (Boeke and Taylor 2016; Previdi et al. 2015), cloud amount (English et al. 2015; Boeke

and Taylor 2016), and cloud phase (Morrison et al. 2009; Kay et al. 2016). To improve the GCMs, a thorough understanding of relevant processes is necessary, such as atmosphere-surface interactions, clouds, radiation, etc. Among them, longwave (LW) radiation receives relatively little attention compared to other processes. This chapter will focus on two particular aspects of the LW radiation scheme in the GCMs, namely, surface spectral emissivity and cloud LW scattering.

Virtually all GCMs assume surface as blackbody or graybody and neglect cloud LW scattering in their LW radiation scheme, but these assumptions have not been closely examined until recently. Using a modified version of the Community Earth System Model (CESM) that includes realistic surface emissivity, Feldman et al. (2014) and Huang et al. (2018) showed that, compared to blackbody surface, the inclusion of realistic surface emissivity can increase the surface temperature in the high-latitude regions by about 1 K. Chapter 3 also shows that the inclusion of ice cloud LW scattering can increase the surface temperature in the high-latitude regions by about 1 K during wintertime. The combined effect of surface emissivity and cloud LW scattering is also worth studying. Chen et al. (2014), using offline radiative transfer model calculations over the Antarctic plateau, demonstrated that when the surface is not blackbody and clouds can scatter LW radiation, multiple reflection of LW radiation between the surface and clouds can occur and retain more energy in the earth system than the case of blackbody surface and non-scattering clouds. This combined effect, to our best knowledge, has not been quantified in the high-latitude regions using climate model simulations. This chapter intends to quantify this combined effect as well as the relative

contribution of each effect, using a modified version of the CESM version 1.1.1 (CESM1.1.1).

The remainder of this chapter is organized as follows: Section 4.2 describes the modified version of the CESM used in this chapter and the design of simulation experiments. Section 4.3 presents the numeric results and physical interpretations. Conclusions and further discussions are then given in section 4.4.

4.2 Methods

4.2.1 Description of the modified version of the CESM1.1.1

Because the original CESM1.1.1 assumes the surface as blackbody and non-scattering clouds in the LW radiation scheme in the atmosphere model, three modifications are implemented and briefly described as follows:

(1) The implementation of surface spectral emissivity based on Huang et al. (2018). Surface spectral emissivity dataset is taken from Huang et al. (2016), in which a hybrid approach was used to develop a global surface emissivity dataset suitable for the use in weather and climate models. This surface emissivity dataset is implemented into the LW radiation scheme of the CESM1.1.1, RRTMG_LW (Mlawer et al. 1997), through which the surface upward broadband LW flux provided from the surface models is redistributed into RRTMG_LW bands according to the realistic surface spectral emissivity, instead of blackbody. Details about this modification and its verification can be found in Huang et al. (2018).

(2) The implementation of a two/four-stream radiation transfer solver into the RRTMG_LW based on Kuo et al. (2020). Because the RRTMG_LW is designed for a

non-scattering medium and cannot calculate the LW scattering effect, a two/four-stream radiation transfer solver (Toon et al. 1989; Fu et al. 1997) is implemented into the RRTMG_LW. This solver represents the source function with a two-stream approximation and solves radiative fluxes with a four-stream approximation. Details about this modified RRTMG_LW scheme can be found in Kuo et al. (2020).

(3) The implementation of a new ice cloud LW optical scheme based on Kuo et al. (2020). Since the CESM 1.1.1 does not include the cloud LW scattering effect, the ice cloud LW optical schemes also lacks parameters for cloud LW scattering calculation (e.g. Ebert and Curry 1992; Mitchell et al. 1996). A set of up-to-date ice cloud LW optical parameters is therefore implemented into the CESM1.1.1, namely, extinction coefficients, single-scattering albedos, and asymmetric factors. These parameters are calculated by using the MODIS (Moderate Resolution Imaging Spectroradiometer) Collection 6 ice cloud model (Platnick et al. 2017) with in-situ observed particle size distributions (Baum et al. 2011; Heymsfield et al. 2010; 2013), and then are regressed as a function of the ice effective particle diameter. Details about this ice cloud LW optical scheme can be found in Kuo et al. (2020).

This modified version of CESM1.1.1 has been used to investigate the effects of surface emissivity on the simulated climate (Huang et al. 2018; Chapter 2), and the ice cloud scattering effects in the polar regions in Chapter 3.

4.2.2 Simulation experiment designs

In order to quantify the combined effect of surface emissivity and ice cloud LW scattering, four sets of parallel simulations are carried out. The first set, called “noEmis_noScat”, assumes the surface as blackbody and disables the ice cloud

scattering effect by setting the ice cloud extinction coefficients to its absorption coefficients and single-scattering albedo to zero. The second set, called “Emis_noScat”, is the same as the noEmis_noScat, except using realistic surface spectral emissivity over the entire globe. The differences between the Emis_noScat and noEmis_noScat runs can be deemed as the surface emissivity effect. The third set, “noEmis_Scat”, is the same as the noEmis_noScat, except enabling the ice cloud LW scattering effect. The differences between the noEmis_Scat and noEmis_noScat runs can be deemed as the scattering effect. The last set utilizes realistic surface emissivity and enables ice cloud LW scattering, called “Emis_Scat”. The difference between the Emis_Scat and noEmis_noScat is the combined effect of emissivity and ice cloud scattering.

Since Chapter 3 shows that the ice cloud LW scattering effect is notable only when the surface is coupled with the atmosphere, all simulations are carried out with a slab-ocean model. All simulations are forced with present-day forcings in the year 2000, i.e. the concentration of trace gases and aerosols in the atmosphere are prescribed at the level for the year 2000. Solar forcing is prescribed without year-to-year variation. To account for internal variability, each experiment set is carried out with four ensemble members. Each member begins with a slightly different initial condition, in which a small, random perturbation is imposed to the temperature fields. Each member runs for 35 years and the ensemble mean of the last 30 years are used in following analysis. The horizontal resolution of these simulations is 1.9^{o} latitude by 2.5^{o} longitude and 26 vertical levels exist in the atmospheric model.

4.3 Results and discussion

4.3.1 Emissivity and scattering effects on the entire globe

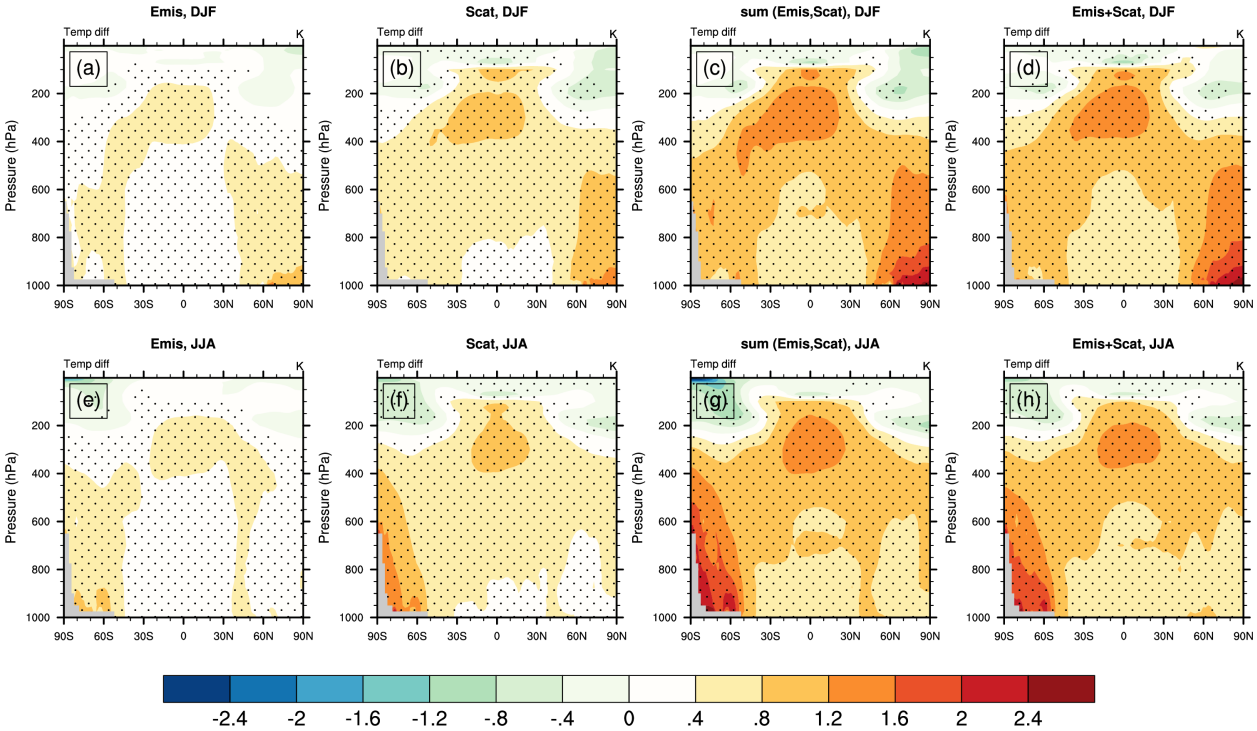

Fig. 4.1. Latitude-pressure cross section of temperature changes due to (a,e) the emissivity effect, (b,f) the scattering effect, (c,g) the sum of the emissivity and scattering effects, and (d,h) the combined effect of emissivity and scattering. (a-d) are in DJF and (e-h) are in JJA. Dotted area indicates that the differences pass the Student's *t* test with a 5% significance level.

Since previous studies have reported that the inclusion of surface emissivity and cloud LW scattering effects can warm the troposphere (Huang et al. 2018; Zhao et al. 2018; Wu et al. 2019), we first examine the changes of tropospheric temperature in response to these effects. Figure 4.1 shows the temperature changes as a function of latitude and pressure level for DJF (December-January-February) and JJA (June-July-August) climatology. Consistent with the findings of previous studies, either emissivity or scattering effect warms virtually the entire troposphere in DJF and JJA. (Fig. 4.1a, b e, and f). Notably, emissivity and scattering effects show distinct spatial and seasonal dependence, with most prominent warming in the polar winter troposphere. The scattering effect in general has larger warming than the emissivity effect, especially in

the tropical upper troposphere, where the cirrus cloud prevails. The combined emissivity and scattering effect (Fig. 4.1d and h) has larger warming than the individual effect, and is approximately the sum of the individual effect (Fig. 4.1d and h versus Fig. 4.1c and g). In other words, the scattering and emissivity effects are linearly additive to a large extent.

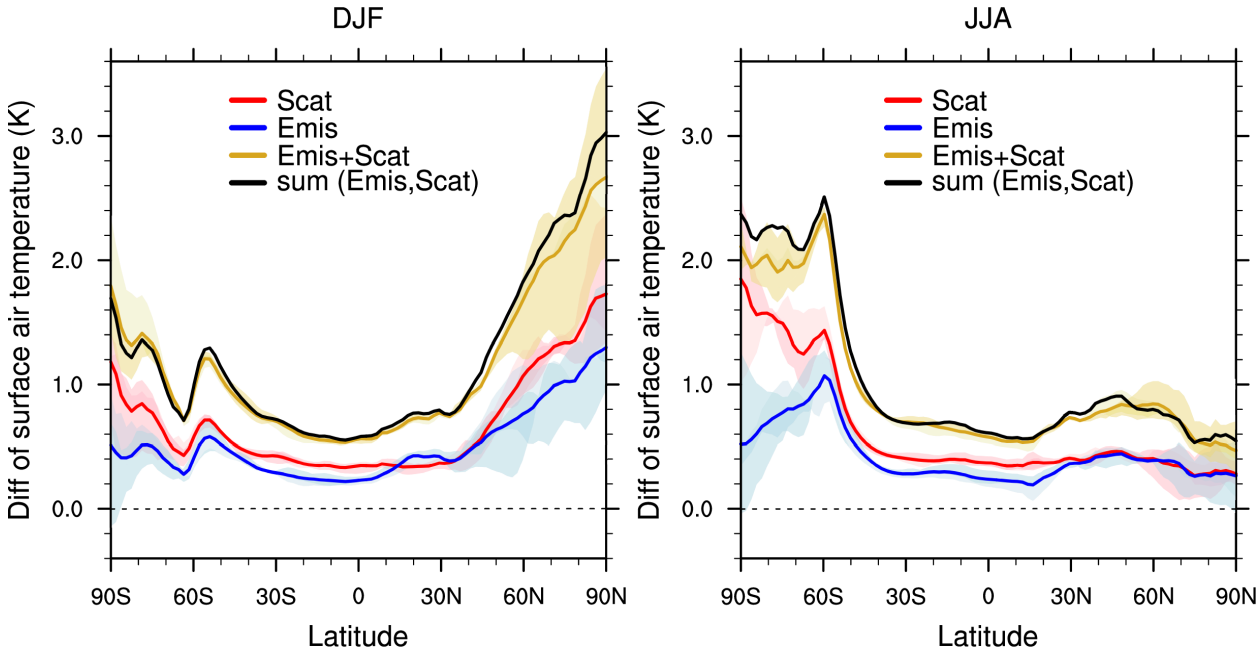

Fig. 4.2. Zonal-mean surface air temperature changes due to the scattering effect (red), the emissivity effect (blue), the sum of emissivity and scattering effects (black), and the combined emissivity and scattering effects (gold). The solid line represents the ensemble mean values and the shaded area indicates the spread of four ensemble members. The left column shows DJF climatology and the right column shows JJA climatology.

We further examine the impact on surface air temperature (SAT). Figure 4.2 shows the changes of the zonal mean SAT responding to these effects in DJF and JJA. Both effects lead to an increase in zonal-mean SAT over the entire globe with comparable magnitudes. In the tropics and mid-latitudes, the SAT increase of either effect is about 0.5K with little seasonal dependence, while in the high-latitude regions, either effect has larger warming, especially in high-latitude winter when the scattering

effect increases the SAT by about 1.8 K in both hemispheres. The combined emissivity and scattering effect (gold line in Fig. 4.2), compared to the individual effect, has a larger warming over the entire globe. This warming roughly equals to the sum of the individual warming effects (black line in Fig. 4.2).

4.3.2 Emissivity and scattering effects on high-latitude surface climate

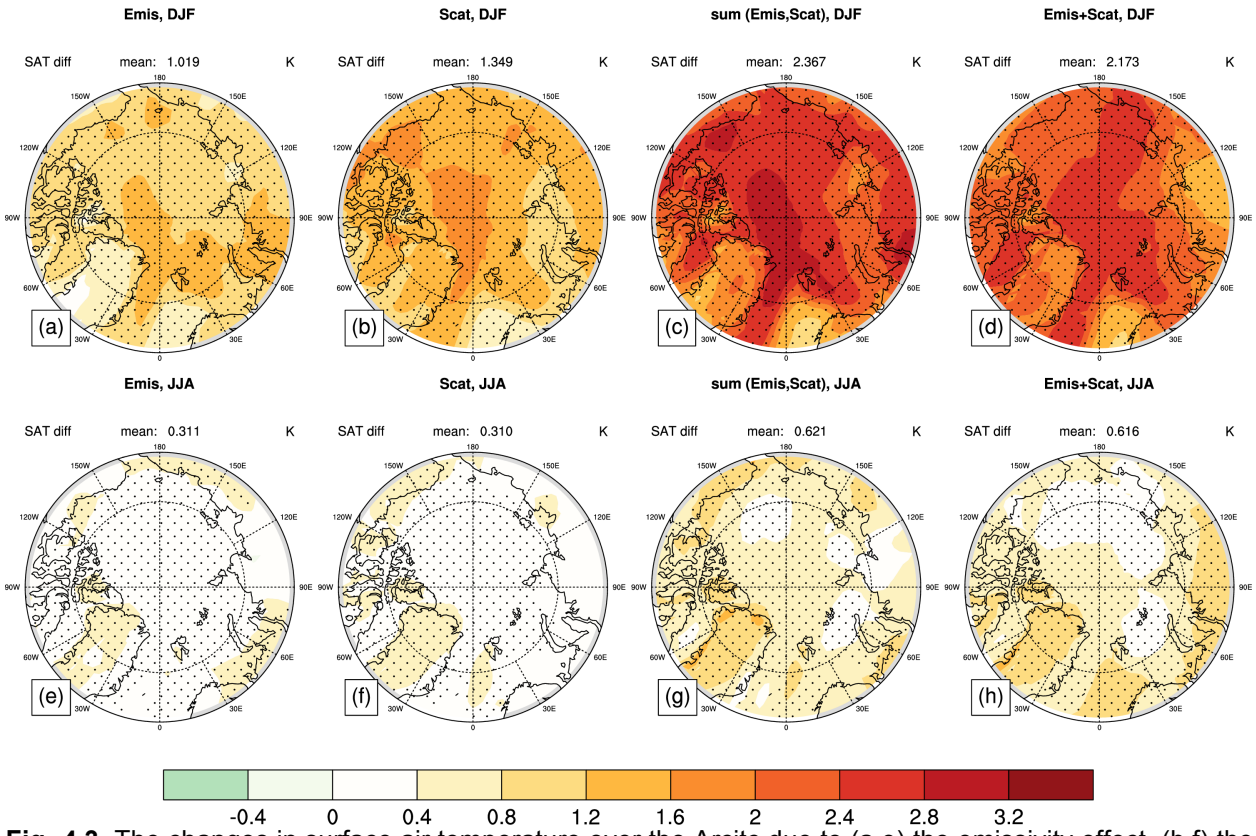

Fig. 4.3. The changes in surface air temperature over the Arcitc due to (a,e) the emissivity effect, (b,f) the scattering effect, (c,g) the sum of the emissivity and scattering effects, and (d,h) the combined effect of emissivity and scattering. (a-d) are in DJF and (e-h) are in JJA. Dotted area indicates that the differences pass the Student's *t* test with a 5% significance level.

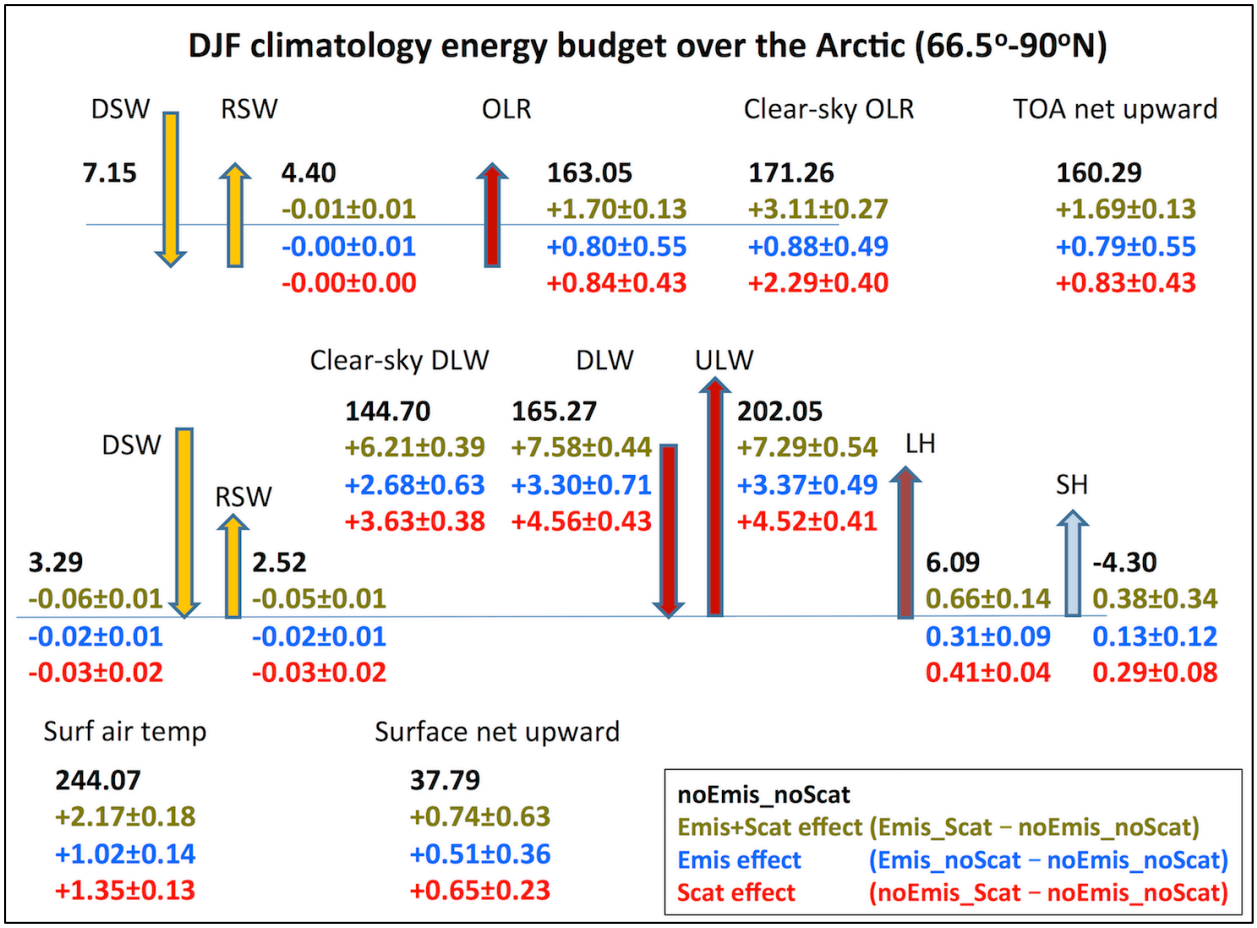

Fig. 4.4. The DJF climatology, Arctic domain-average (66.5°-90°N) energy budget at the TOA and the surface. Values in black are the ensemble mean of the noEmis_noScat run. Values in other colors are the differences between the noEmis_noScat and the respective run. Gold, red, blue colors represent the combined emissivity and scattering effect, the emissivity effect, and the scattering effect, respectively. The standard deviation of four ensemble members is also shown. DSW means downward SW flux, RSW means reflected SW flux, DLW means downward LW flux, ULW means upward LW flux, LH means latent heat flux, SH means sensible heat flux.

Because both the emissivity and scattering effects are most prominent in the high-latitude regions, we take a close look at these regions in both hemispheres. Figure 4.3 shows the SAT changes in the Arctic induced by the emissivity and scattering effects. Each effect warms virtually the entire Arctic basin by approximately 1 K in terms of Arctic domain average (Fig. 4.3a and b), while this warming is largely reduced to about 0.3 K in JJA (Fig. 4.3e and f). Since the combined emissivity and scattering effects can be deemed as a linear summation of each effect, together they warm the

entire Arctic by 2.2 K in DJF and 0.6 K in JJA, respectively (Fig. 4.3d and h). In order to explain the large wintertime warming in Arctic induced by the emissivity and scattering effects, we analyze the Arctic domain-averaged (66.5^{o}N to 90^{o}N) energy budget at the surface and the top of the atmosphere (TOA) as shown in Fig. 4.4. Inspecting each term in the surface energy budget, the largest difference is the downward LW flux at the surface, about +3.30 Wm^{-2} for the emissivity effect, +4.56 Wm^{-2} for the scattering effect, and +7.58 Wm^{-2} for the combined effect. These increases are largely attributed to the increase of clear-sky downward LW flux, as the difference between the all-sky and clear-sky fluxes at the surface is roughly 1 W m^{-2}. Since both the emissivity and scattering effects induce minimal changes in surface shortwave (SW) fluxes, latent heat and sensible heat fluxes, and horizontal energy transport (calculated as the net upward energy flux at the TOA minus the net upward flux at the surface), these increases in surface downward LW flux are largely compensated by the increase in the surface upward LW flux, consistent with the increase in SAT. At the TOA, the outgoing LW radiation (OLR) increases by 0.80, 0.84, and 1.70 Wm^{-2} for the emissivity, scattering, and the combined effect, respectively, which is associated to the increase in SAT.

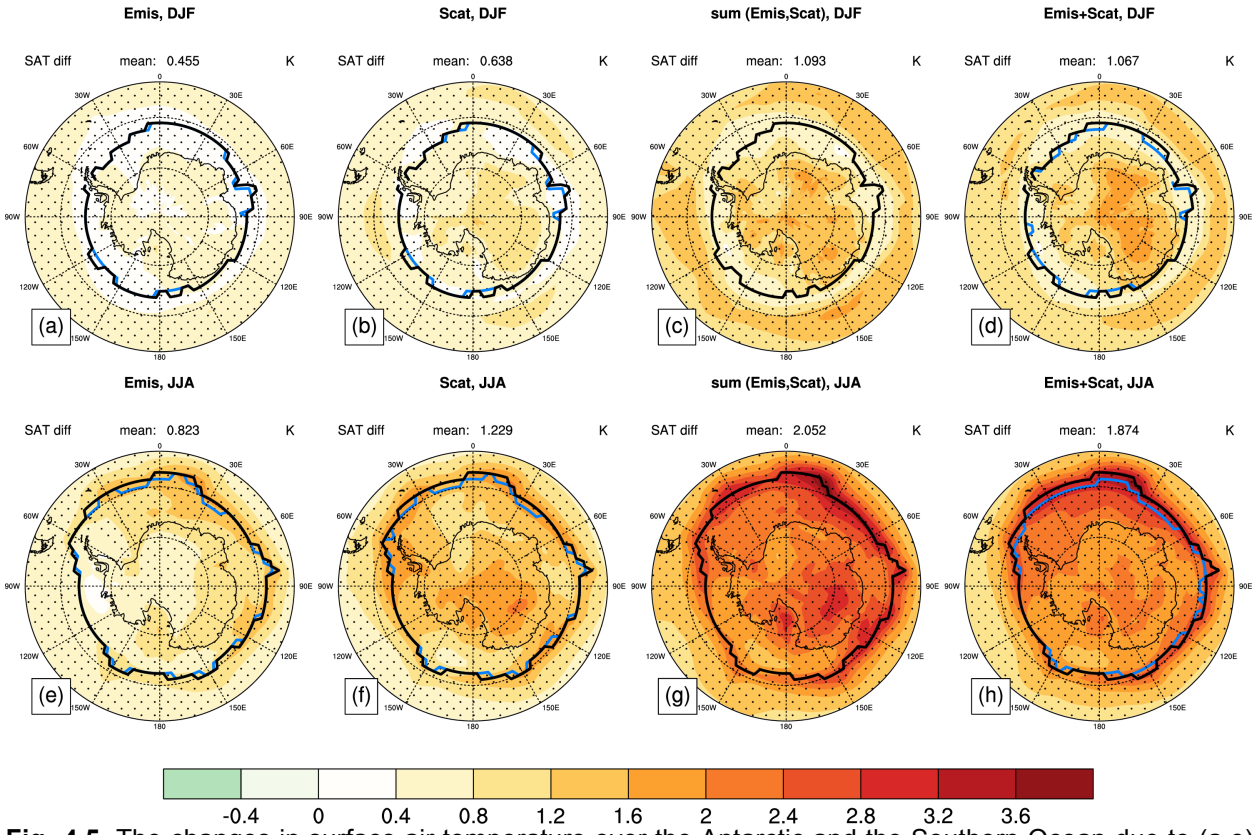

Fig. 4.5. The changes in surface air temperature over the Antarctic and the Southern Ocean due to (a,e) the emissivity effect, (b,f) the scattering effect, (c,g) the sum of the emissivity and scattering effects, and (d,h) the combined effect of emissivity and scattering. (a-d) are in DJF and (e-h) are in JJA. The black line shows the sea ice edge of the noEmis_noScat run and the blue line shows the sea ice edge of Emis_noScat run in (a,e), noEmis_Scat run in (b,f), and Emis_Scat run in (d,h). Dotted area indicates that the differences pass the Student's *t* test with a 5% significance level.

Similar to Fig. 4.3 and 4.4, we also take a close look at the SAT changes in the Antarctic and the Southern Ocean, as shown in Fig. 4.5. Consistent with the findings in the Arctic, either emissivity or scattering effect warms virtually the entire Antarctic and the Southern Ocean, as well as the combined effect. These warming are larger in wintertime (JJA) than summertime (DJF). We also analyze the Antarctic domain-averaged (66.5^{o}S to 90^{o}S) energy budget at the surface and TOA, as shown in Fig. 4.6. The surface energy budget shows increases of downward LW flux at the surface in response to the emissivity and scattering effects (+2.56 Wm^{-2} for the emissivity effect, and +5.18 Wm^{-2} for the scattering effect, and +7.03 Wm^{-2} for the coupling effect). These

increases are mainly attributed to the increases in clear-sky downward LW flux. Similar to the Arctic (Fig. 4.4), the SW fluxes, latent heat and sensible heat fluxes, and horizontal energy transport only show minimal changes in response to either the emissivity or scattering effect. Thus, the increases in downward LW flux at the surface are largely balanced by the increases in upward LW flux at the surface, consistent with the increase in SAT. This increase in SAT also leads to an increase in clear-sky OLR, in particular the cases of the scattering and the combined effects, of which have large SAT increases. The all-sky OLR exhibits minimal changes in these two cases, indicating an increase in high cloud fraction over this region.

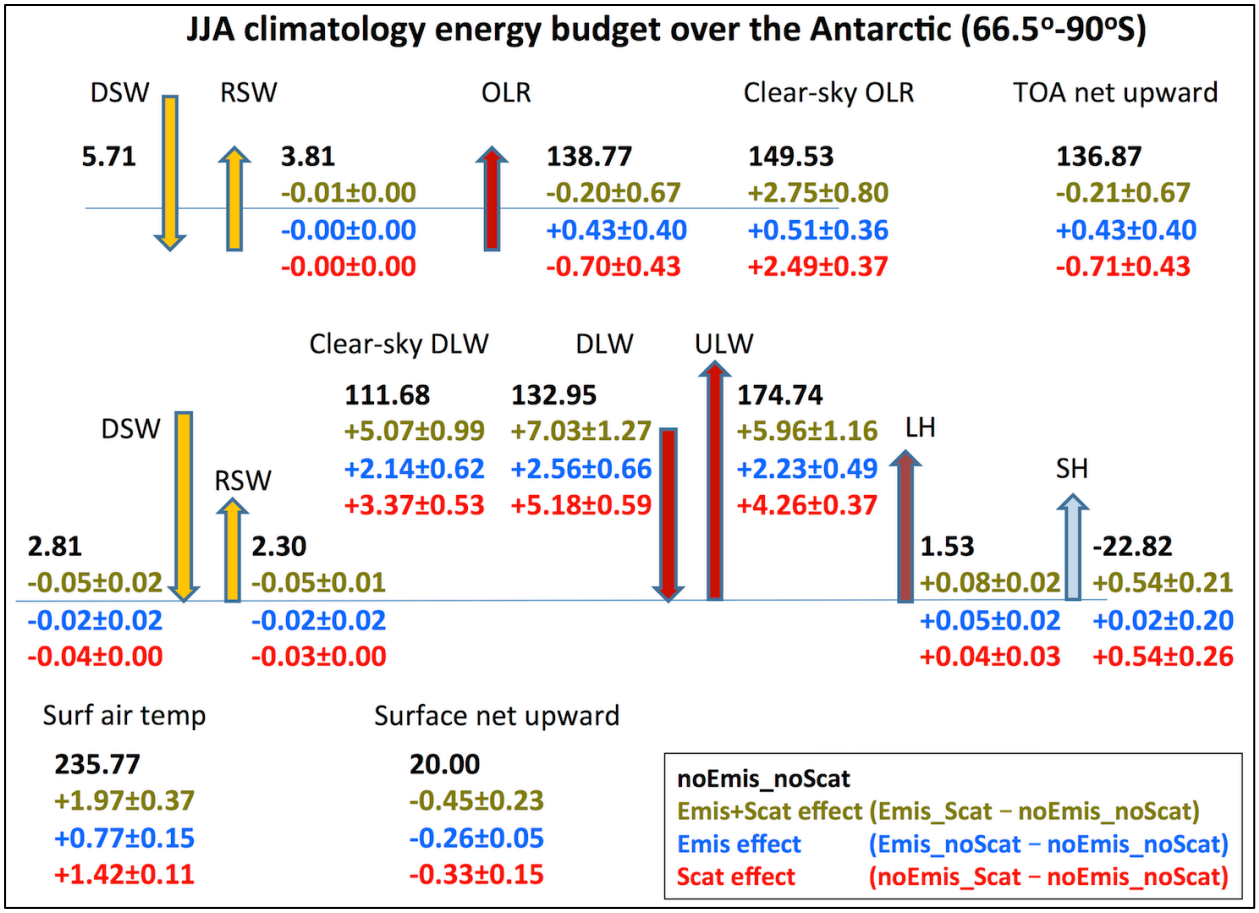

Fig. 4.6. Same as Fig. 4.4 but for the Antarctic domain-average (66.5°-90°S) in JJA.

4.3.3 Emissivity and scattering effects on the Southern Ocean

The increase in SAT over the Southern Ocean can affect the sea ice fraction. Figure 4.5 shows that, in DJF (austral summer), the SAT changes over the sea ice regions exhibit smaller changes than those over the Antarctic continent and adjacent ocean (Fig. 4.5a-d). The sea ice edge, defined as the most equatorward latitude where sea ice fraction is larger than 35%, also exhibits minimal changes responding to the scattering and emissivity effects. In contrast to DJF, the SAT in JJA (austral winter) shows large increases in the proximity of the sea ice edge for emissivity, scattering, and the combined effects. The sea ice retreats in all cases, in particular when the emissivity and scattering effects are combined, though the retreat extent is small. This motivates us to take a further look at the sea ice fraction changes in the Southern Ocean.

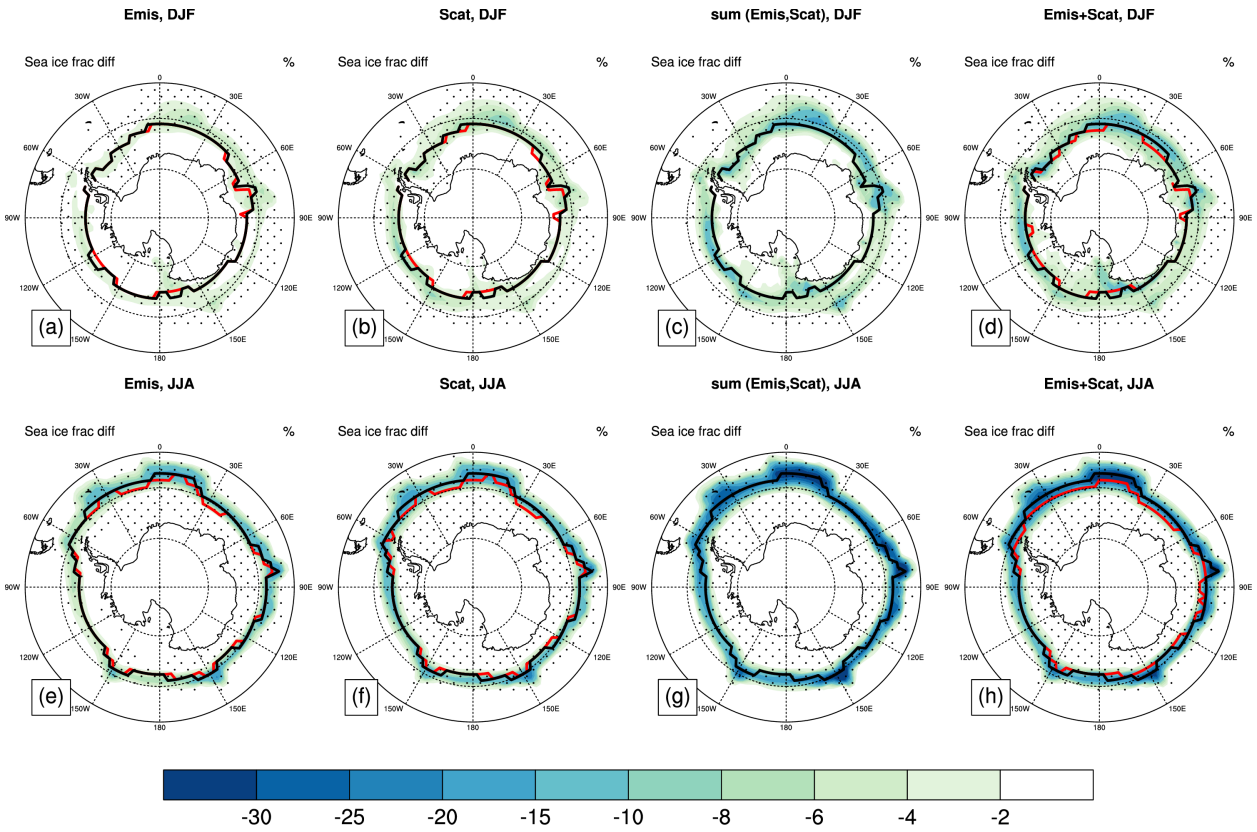

Fig. 4.7. Same as for Fig. 4.5 but for sea ice fraction. The sea ice edge is shown in red lines.

Figure 4.7 shows the changes of sea ice fraction in the Southern Ocean. The sea ice fraction decreases in both DJF and JJA. In JJA, this decrease in sea ice fraction mostly concentrates around the sea ice edge (Fig. 4.7e-h) and can be as large as 30%. These sea ice decreases are associated with the large SAT increase in these regions (Fig. 4.5e-h). In DJF, the decrease in sea ice not only occurs around the sea ice edge, but also around the Antarctic continent (Fig. 4.7a-d). This decrease is not as large as those in JJA, but still can be about 10%. The combined effects of scattering and emissivity show a larger decrease in sea ice fraction than those of the individual effect. These results show that the inclusion of surface emissivity and ice cloud LW scattering increases the SAT, which in turn decreases the sea ice fraction.

Sea ice is a good insulator and inhibits the exchanges of heat and moisture between the surface and the atmosphere. When sea ice melts and exposes the ocean underneath, the exchanges of heat and moisture between the surface and atmosphere can increase significantly (Taylor et al. 2018), influencing the properties of boundary layer and clouds. The changes in low cloud fraction are examined in Fig. 4.8. The low cloud fraction increase over the sea ice in both DJF and JJA, especially around the sea ice edge. The increases in low cloud fraction and the decreases of sea ice fraction are approximately collocated, implying that the changes in surface conditions and boundary layer are responsible to the increases in low cloud fraction. The combined effect of emissivity and scattering has the largest SAT increase and sea ice decrease, resulting in the largest increase in low cloud fraction.

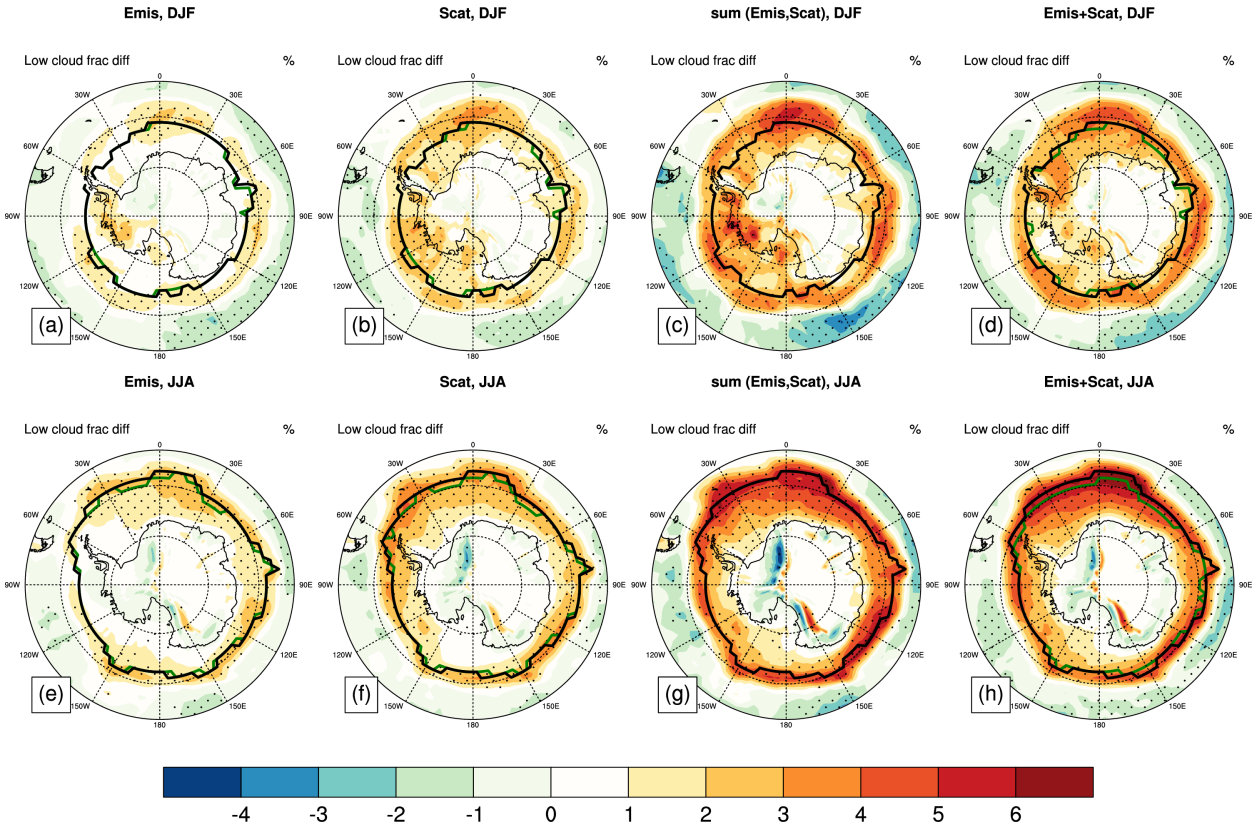

Fig. 4.8. Same as for Fig. 4.5 but for low cloud fraction. The sea ice edge is shown in green lines.

The increase in low cloud fraction in DJF can affect SW radiation at the surface and the TOA. Figure 4.9a-d show that the surface downward SW flux decreases over the sea ice regions by about 10 Wm^{-2} for either the emissivity or scattering effect and by about 15 Wm^{-2} for the combined effect, as a result of the increase in low cloud fraction that reflect more SW flux to space. The surface net downward SW fluxes (Fig. 4.9e-h), however, remain unchanged for emissivity or scattering effect and even increase for the combined effect by about 5 Wm^{-2}. This inconsistency reveals that although the increase in low cloud fraction reduces the surface downward SW flux, this effect on the net flux is largely offset by the decrease in sea ice fraction, in which the surface albedo decreases

so that the surface absorbs more SW energy. The changes of net downward SW flux at the TOA largely resemble that at the surface.

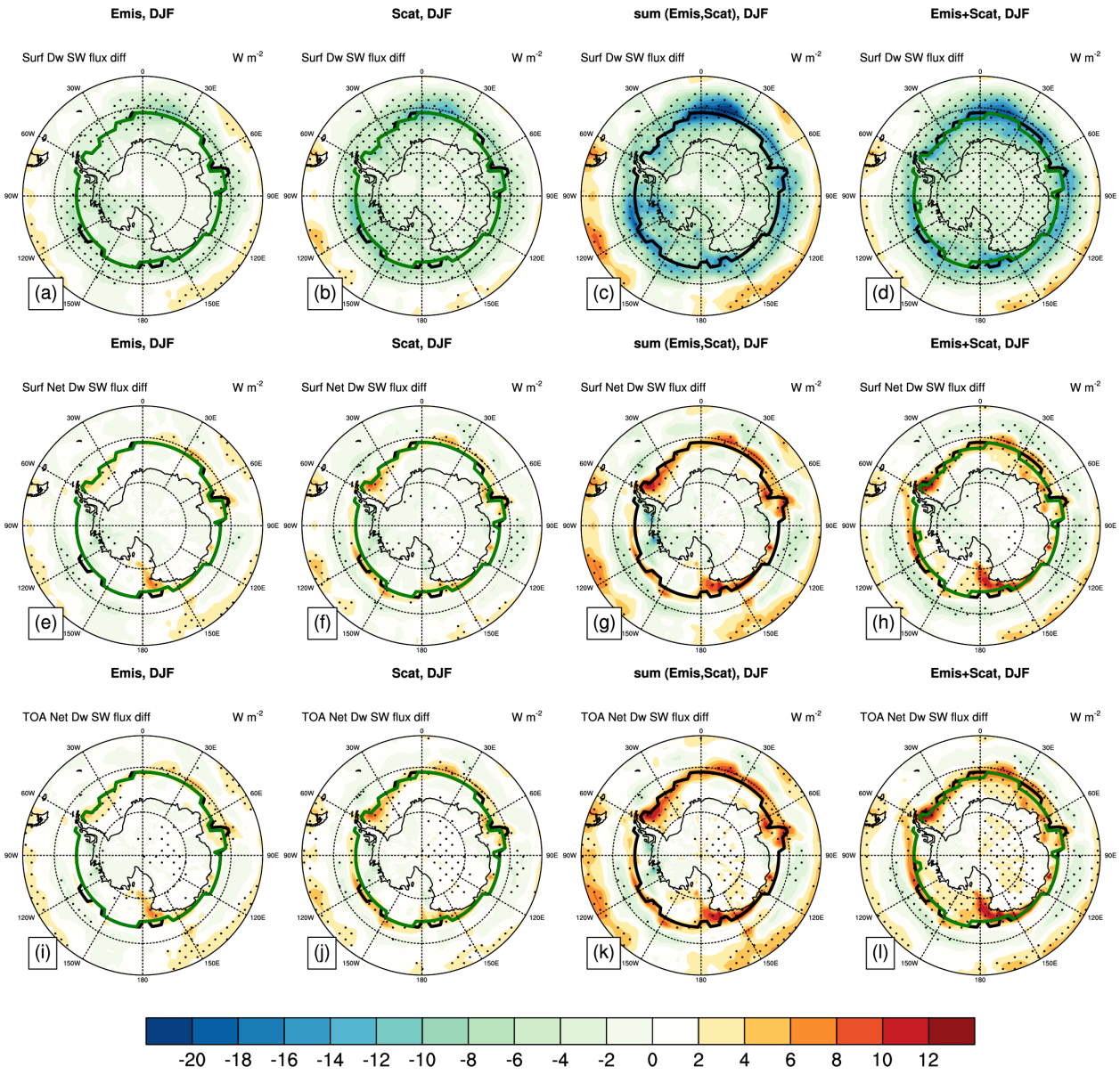

Fig. 4.9. The changes in downward SW flux at the surface (a-d), net downward SW flux at the surface (e-h), and net downward SW flux at the TOA (i-l) in DJF. (a,e,i) show the emissivity effect, (b,f,j) show the scattering effect, (c,g,k) show the sum of the emissivity and scattering effects, and (d,h,l) show the combined effect of emissivity and scattering. The black line shows the sea ice edge of the noEmis_noScat run and the green line shows the sea ice edge of Emis_noScat run in (a,e,i), noEmis_Scat run in (b,f,j), and Emis_Scat run in (d,h,l). Dotted area indicates that the differences pass the Student's *t* test with a 5% significance level.

4.4 Conclusion

Most GCMs assume surface as blackbody and non-scattering clouds in their LW radiation scheme. Previous studies have reported that these two assumptions can be questionable in the high-latitude regions, and demonstrated that the inclusion of either surface spectral emissivity or ice cloud LW scattering can increase the SAT in the high-latitude regions. However, the combination of these two effects and the relative contributions of each on the high-latitude regions have not been quantified, which becomes the main focus of this chapter.

Consistent with previous studies, our results show that either surface emissivity and ice cloud LW scattering effects warm virtually the entire troposphere and the surface on the high-latitude regions, and this warming is more prominent in wintertime than in summertime. Our results show that the magnitudes of these two effects are comparable and the combined effect of these two is roughly the summation of each individual effect.

This study mainly focuses on the surface energy budget in high-latitude regions in response to the emissivity and scattering effect. It is worthwhile to conduct further analyses. For instance, this study shows that the emissivity and scattering effects induce larger warming in the high-latitude regions than the tropic and mid-latitudes, which can change the meridional temperature gradient and potentially affect large-scale circulations. Studying the changes in large-scale circulations due to the surface emissivity and scattering effects would be a potential research topic.

References

Baum, B. A., P. Yang, A. J. Heymsfield, C. G. Schmitt, Y. Xie, A. Bansemer, Y. X. Hu, and Z. Zhang, 2011: Improvements in shortwave bulk scattering and absorption models for the remote sensing of ice clouds. J. Appl. Meteorol. Climatol., 50, 1037–1056, doi:10.1175/2010JAMC2608.1.

Boeke, R. C., and P. C. Taylor, 2016: Evaluation of the Arctic surface radiation budget in CMIP5 models. J. Geophys. Res. Atmos., 121, 8525–8548, doi:10.1002/2016JD025099.

Chen, X. H., X. L. Huang, and M. G. Flanner, 2014: Sensitivity of modeled far-IR radiation budgets in polar continents to treatments of snow surface and ice cloud radiative properties. Geophys. Res. Lett., 41, 6530–6537, doi:10.1002/2014GL061216.

Ebert, E. E., and J. A. Curry, 1992: A parameterization of ice cloud optical properties for climate models. J. Geophys. Res., 97, 3831–3836, doi:10.1029/91JD02472.

English, J. M., A. Gettelman, and G. R. Henderson, 2015: Arctic radiative fluxes: Present-day biases and future projections in CMIP5 models. J. Clim., 28, 6019–6038, doi:10.1175/JCLI-D-14-00801.1.

Fan, T., C. Deser, and D. P. Schneider, 2014: Recent Antarctic sea ice trends in the context of Southern Ocean surface climate variations since 1950. Geophys. Res. Lett., 41, 2419–2426, doi:10.1002/2014GL059239.

Feldman, D. R., W. D. Collins, R. Pincus, X. Huang, and X. Chen, 2014: Far-infrared surface emissivity and climate. Proc. Natl. Acad. Sci. U. S. A., 111, 16297–16302, doi:10.1073/pnas.1413640111.

Fu, Q., K. N. Liou, M. C. Cribb, T. P. Charlock, and A. Grossman, 1997: Multiple Scattering Parameterization in Thermal Infrared Radiative Transfer. J. Atmos. Sci., 54, 2799–2812, doi:10.1175/1520-0469(1997)054<2799:MSPITI>2.0.CO;2.

Heymsfield, A. J., C. Schmitt, A. Bansemer, and C. H. Twohy, 2010: Improved Representation of Ice Particle Masses Based on Observations in Natural Clouds. J. Atmos. Sci., 67, 3303–3318, doi:10.1175/2010jas3507.1.

Heymsfield, A. J., C. Schmitt, and A. Bansemer, 2013: Ice Cloud Particle Size Distributions and Pressure-Dependent Terminal Velocities from In Situ Observations at Temperatures from 0° to −86°C. J. Atmos. Sci., 70, 4123–4154, doi:10.1175/jas-d-12-0124.1.

Hobbs, W. R., R. Massom, S. Stammerjohn, P. Reid, G. Williams, and W. Meier, 2016: A review of recent changes in Southern Ocean sea ice, their drivers and forcings. Glob.

Planet. Change, 143, 228–250, doi:10.1016/j.gloplacha.2016.06.008. http://dx.doi.org/10.1016/j.gloplacha.2016.06.008.

Huang, X. L., X. H. Chen, D. K. Zhou, and X. Liu, 2016: An Observationally Based Global Band-by-Band Surface Emissivity Dataset for Climate and Weather Simulations. J. Atmos. Sci., 73, 3541–3555, doi:10.1175/JAS-D-15-0355.1.

Huang, X. L., X. H. Chen, M. Flanner, P. Yang, D. R. Feldman, and C. Kuo, 2018: Improved Representation of Surface Spectral Emissivity in a Global Climate Model and Its Impact on Simulated Climate. J. Clim., 31, 3711–3727, doi:10.1175/JCLI-D-17-0125.1.

Kay, J. E., L. Bourdages, N. B. Miller, A. Morrison, V. Yettella, H. Chepfer, and B. Eaton, 2016: Evaluating and improving cloud phase in the Community Atmosphere Model version 5 using spaceborne lidar observations. J. Geophys. Res. Atmos., 121, 4162–4176, doi:10.1002/2015JD024699.

Kuo, C.-P., P. Yang, X. Huang, Y.-H. Chen, and G. Liu, 2020: Assessing the accuracy and efficiency of longwave radiative transfer models involving scattering effect with cloud optical property parameterizations. J. Quant. Spectrosc. Radiat. Transf., 240, 106683, doi:10.1016/j.jqsrt.2019.106683.

Lawson, R. P., and A. Gettelman, 2014: Impact of Antarctic mixed-phase clouds on climate. Proc. Natl. Acad. Sci. U. S. A., 111, 18156–18161, doi:10.1073/pnas.1418197111.

Mayewski, P., and Coauthors, 2009: State of the Antarctic and Southern Ocean climate system. Rev. Geophys., 47, RG1003, doi:10.1029/2007RG000231.

Mitchell, D. L., A. Macke, and Y. G. Liu, 1996: Modeling cirrus clouds .2. Treatment of radiative properties. J. Atmos. Sci., 53, 2967–2988, doi:Doi 10.1175/1520-0469(1996)053<2967:Mccpit>2.0.Co;2.

Mlawer, E. J., S. J. Taubman, P. D. Brown, M. J. Iacono, and S. A. Clough, 1997: Radiative transfer for inhomogeneous atmospheres: RRTM, a validated correlated-k model for the longwave. J. Geophys. Res. Atmos., 102, 16663–16682, doi:10.1029/97JD00237.

Morrison, H., and Coauthors, 2009: Intercomparison of model simulations of mixed-phase clouds observed during the ARM Mixed-Phase Arctic Cloud Experiment. II: Multilayer cloud. Q. J. R. Meteorol. Soc., 135, 1003–1019, doi:10.1002/qj.415. http://arxiv.org/abs/0801.1618.

Parkinson, C. L., and N. E. DiGirolamo, 2016: New visualizations highlight new information on the contrasting Arctic and Antarctic sea-ice trends since the late 1970s.

Remote Sens. Environ., 183, 198–204, doi:10.1016/j.rse.2016.05.020. http://dx.doi.org/10.1016/j.rse.2016.05.020.

Platnick, S., and Coauthors, 2017: The MODIS Cloud Optical and Microphysical Products: Collection 6 Updates and Examples from Terra and Aqua. IEEE Trans. Geosci. Remote Sens., 55, 502–525, doi:10.1109/TGRS.2016.2610522.

Previdi, M., K. L. Smith, and L. M. Polvani, 2015: How well do the CMIP5 models simulate the antarctic atmospheric energy budget? J. Clim., 28, 7933–7942, doi:10.1175/JCLI-D-15-0027.1.

Richter-Menge, J., M. O. Jeffries, and E. Osborne, Eds., 2018: The Arctic [in “State of the Climate in 2017”]. Bull. Amer. Meteor. Soc., 99 (8), S143–173, doi:10.1175/2018BAMSStateoftheClimate.1.

Taylor, P. C., B. M. Hegyi, R. C. Boeke, and L. N. Boisvert, 2018: On the increasing importance of air-sea exchanges in a thawing Arctic: A review. Atmosphere (Basel)., 9, 1–39, doi:10.3390/atmos9020041.

Toon, O. B., C. P. McKay, T. P. Ackerman, and K. Santhanam, 1989: Rapid calculation of radiative heating rates and photodissociation rates in inhomogeneous multiple scattering atmospheres. J. Geophys. Res., 94, 287–301, doi:10.1029/JD094iD13p16287.

Turner, J., and Coauthors, 2014: Antarctic climate change and the environment: An update. Polar Rec. (Gr. Brit)., 50, 237–259, doi:10.1017/S0032247413000296.

Turner, J., J. S. Hosking, T. J. Bracegirdle, G. J. Marshall, and T. Phillips, 2015: Recent changes in Antarctic Sea Ice. Philos. Trans. R. Soc. A Math. Phys. Eng. Sci., 373, 20140163, doi:10.1098/rsta.2014.0163.

Wu, K., J. Li, J. Cole, X. Huang, K. von Salzen, and F. Zhang, 2019: Accounting for Several Infrared Radiation Processes in Climate Models. J. Clim., 32, 4601–4620, doi:10.1175/JCLI-D-18-0648.1.

Zhao, W., Y. Peng, B. Wang, and J. Li, 2018: Cloud longwave scattering effect and its impact on climate simulation. Atmosphere (Basel)., 9, 1–20, doi:10.3390/atmos9040153.

Chapter 5

Improving the Surface and Cloud Longwave Radiation Treatments in the Energy Exascale Earth System Model (E3SM)

5.1 Introduction

Both long-term climate trends and short-term climate variability can have substantial impacts on the energy sector and affect energy security. The U.S. Department of Energy (DOE) has identified at least three observed climate trends that can impact the energy sector, namely, increasing air and water temperatures, decreasing water availability in some regions and seasons, and increasing intensity and frequency of storm events, flooding, and sea level rise (U.S. Department of Energy, 2013). The ability to simulate and predict these climate trends is crucial for energy-sector decisions, but beyond the capabilities of the existing state-of-the-art Earth system models. To meet the mission needs of the DOE and the science needs of the nation, the DOE has funded the Energy Exascale Earth System Model (E3SM) project, formerly known as the Accelerated Climate Modeling for Energy (ACME; Bader et al., 2014). In particular, the E3SM aims to address three climate change thematic areas, namely, Water Cycle, Cryosphere, and Biogeochemistry.

Longwave (LW) radiation processes play an important role in the Earth's climate system, and these processes can influence the three main climate thematic areas of the

E3SM. The E3SM, among other Earth system models, assumes that the surface is blackbody or graybody and clouds are non-scattering in its LW radiation scheme. Previous studies (e.g. Chen et al. 2014; Feldman et al. 2014; Huang et al. 2018) and Chapters 3 and 4 have demonstrated that these assumptions are not valid in the high-latitude regions. Specifically, the inclusion of surface spectral emissivity or ice cloud LW scattering can warm the high-latitude surface air temperature by about 1K for each and they together can warm by about 2K. Since the E3SM particularly focuses on water cycle and cryosphere, of which the high-latitude regions play an important role, proper representations of the LW radiation processes are essential to predict future climate in these regions. This suggests that both surface spectral emissivity and cloud LW scattering treatments need to be included in the E3SM. This chapter describes the implementations of these treatments into the E3SM, similar to what we have been done for the CESM (Community Earth System Model) in the previous chapters. We then carry out climate simulations to examine the impact of these implementations in the E3SM, particularly to what extent these treatments affect the key climate features in high-latitude regions, such as surface air temperature, precipitation, and radiative fluxes at the surface and the top of the atmosphere.

The remainder of this chapter is organized as follows. Section 5.2 briefly describes the E3SM and the design of simulation experiments. Section 5.3 presents the simulation results analysis and discussion. Conclusions and further discussions are given in section 5.4.

5.2 Methods

5.2.1 Description of the E3SM

This study uses the first version of the E3SM (E3SMv1; Golaz et al. 2019). The E3SMv1 is branched from the CESM version 1 (CESM1; Hurrell et al. 2013), but has evolved significantly ever since. Similar to the CESM1, the E3SMv1 has six sub-model components: atmosphere, land, ocean, sea ice, land ice, and river. The Atmospheric Model component (EAM) is based on the Community Atmospheric Model version 5.3 (CAM5.3; Neale et al. 2012), with notable changes in parameterizations of aerosol, clouds, and convection (Rasch et al. 2019). Note that these changes are broadly similar to those from CAM5.3 to CAM6. The Land Model component (ELM) is based on the Community Land Model Version 4.5 (CLM4.5; Oleson et al. 2013) with new options for representing soil hydrology and biogeochemistry. The ocean, sea ice, and land ice components, compared to the CESM1, are replaced with the Model for Prediction Across Scales (MPAS; Ringler et al. 2010; Petersen et al. 2019). The river component is also replaced with the Model for Scale Adaptive River Transport (MOSART; Li et al. 2013; 2015).

Similar to what we have done for the CESM, we implement three modifications into the LW radiation scheme in the E3SM, namely, surface spectral emissivity (Huang et al. 2016; 2018), a two/four-stream radiation transfer solver to handle scattering calculation (Kuo et al. 2020), and a new ice cloud LW optical scheme based on MODIS (Moderate Resolution Imaging Spectroradiometer) Collection 6 ice cloud model (MC6; Kuo et al. 2020). Details about these modifications can be found in Chapter 4.2 of this dissertation.

5.2.2 Simulation experiment designs

In order to examine the impact of these implementations, we carry out four sets of parallel simulations. The first set uses the standard E3SM as the reference, called "CTL". The second set, called "Emis", is the same as CTL except using realistic surface spectral emissivity over the entire globe. The differences between the Emis and CTL runs can be deemed as the surface emissivity effect. The third set, called "IceCloud", is the same as the CTL except using the two/four-stream radiation transfer solver, the MC6 ice cloud LW optical scheme, and enabling the ice cloud LW scattering effect. The differences between the IceCloud and CTL runs can be deemed as the impact of the new ice cloud LW treatments. The last set, called "Emis+IceCloud", utilizes realistic surface emissivity and the new ice cloud LW treatments. The difference between the Emis+IceCloud and CTL represents the combined effect of surface emissivity and ice cloud treatments.

Because the ice cloud LW scattering effects are notable only when the surface is coupled with the atmosphere (Chapter 3), we carry out fully-coupled E3SM simulations for each experiment set, i.e. all model components are active and coupled with each other. Given that the fully-coupled simulations can take hundreds of simulation years to spin up and requires considerable computational resources, all simulations are initialized with the Year 2000 from the historical run of the standard E3SM, provided by the E3SM team. Details about the E3SM historical run can be found in Golaz et al. (2019). Due to the limitation of computational resources, only one member for each experiment set is performed in this chapter. Each experiment member runs for 15 years (2000-2014) with the historical forcings, e.g. the concentration of carbon dioxide

increases with time, and then all 15-year results are used in the following analysis. The historical forcings and the configuration of the E3SM historical run closely resemble those in the Climate Model Intercomparison Project Phase 6 (Eyring et al., 2016; Golaz et al. 2019). The horizontal resolution is 1° latitude by 1° longitude for the atmosphere and land models, 0.5° for the river model, and mesh spacing varying between 60 km in the midlatitudes and 30 km at the equator and poles for the ocean and sea ice model. 72 vertical levels are in the atmospheric model.

5.3 Results

5.3.1 Impacts on surface climate

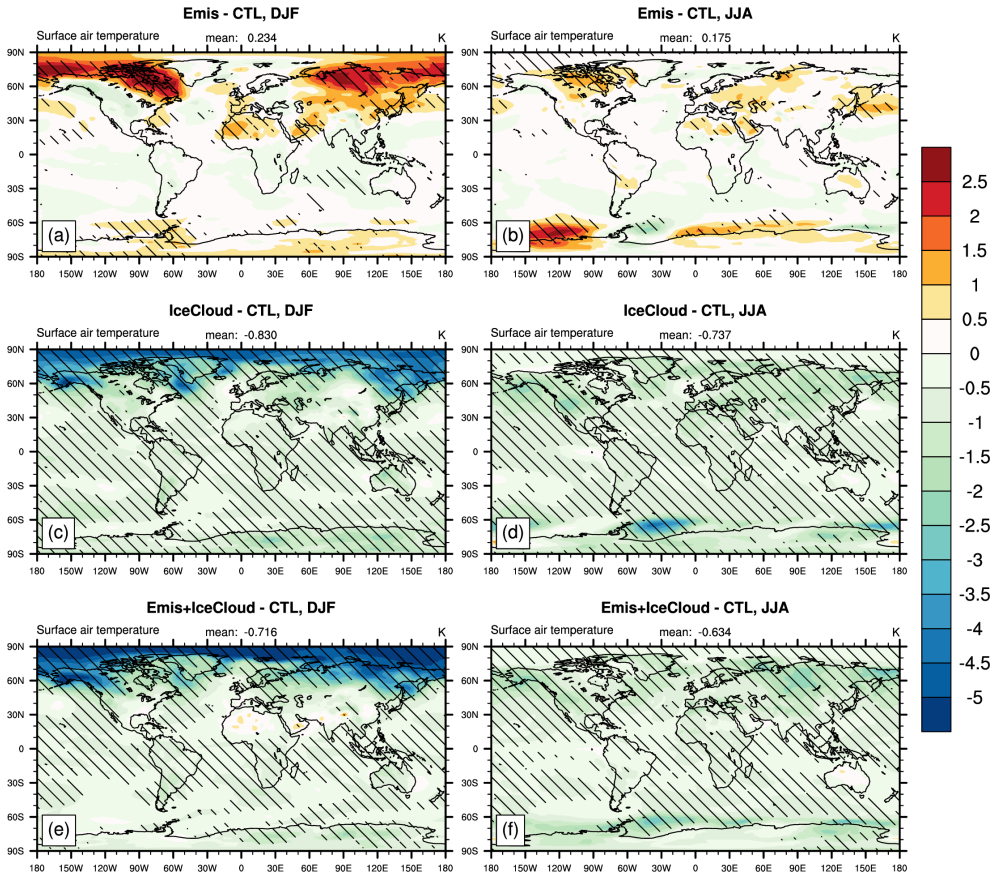

Fig. 5.1. The differences of surface air temperature in DJF (left column) and JJA (right column). (a,b) The differences between the Emis and CTL runs, (c,d) the difference between the IceCloud and CTL runs. (e,f) The difference between the Emis+IceCloud and CTL runs. Slashed area indicates that the differences pass the Student's *t* test with a 5% significance level.

Figure 5.1 shows the changes of surface air temperature (SAT) in response to the inclusion of surface spectral emissivity and ice cloud treatment. The inclusion of surface emissivity leads to an increase in SAT over the high-latitude regions, especially during wintertime (Fig. 5.1a and b), consistent with the results shown in Chapter 4 using the CESM simulations with a slab-ocean model. The inclusion of surface emissivity also increases the SAT over the Sahara and Sahel, consistent with the findings in Chapter 2 using the CESM with prescribed sea surface temperatures. Since the inclusion of surface emissivity exhibits similar effects in different models and configurations, this shows the robustness of the surface emissivity effect. The physical explanations for the SAT increases in the high-latitude and the Sahara and Sahel regions have been discussed in Chapter 4 and Chapter 2, respectively, and is briefly summarized as follows. In the high-latitude regions, the surface emissivities of ice and snow are around 0.9 in the far-IR bands (0-630 cm^{-1}; Huang et al. 2018). Using realistic surface emissivity over these regions, compared to blackbody, reduces the surface emission in the far-IR band. This reduction cannot be compensated by the enhancement of the reflected downward LW flux at the surface, as the downward far-IR flux is much smaller than the surface emission in the far-IR because of the small far-IR emission from the cold and dry atmosphere. As a result, the surface emits less energy when the realistic surface emissivity is used, which means more energy is retained at the surface and leads to an increase in the SAT. The physical explanation for the SAT increase in the Sahara and Sahel regions is similar to those in the high-latitude regions, but switches from the far-IR band to the atmospheric window band (~800-1200 cm^{-1}). The surface emissivity over the window band can be as low as 0.7 over the Sahara and Sahel,

which reduces surface emission compared to those use blackbody surface. This reduction is unable to be compensated by the enhancement of reflection of the downward LW flux at the surface, because the atmospheric emission in the window band is small over the Sahara and Sahel, mainly because clouds are infrequent.

Examining the SAT changes due to the inclusion of the ice cloud treatments (Fig. 5.1c and d), it shows that the SAT decreases over the entire globe, especially during high-latitude wintertime. These decreases in SAT are mainly because the MC6 ice optical scheme has smaller ice cloud LW extinction coefficients compared to the counterpart in the E3SM. As a result, ice clouds with the same water path have smaller optical depth in the IceCloud run than that in the standard E3SM. This leads to less absorption as well as emission by the cloud, in another word, the greenhouse effect of ice cloud in the IceCloud run is not as strong as it in the standard E3SM, resulting in a reduction of surface temperature overall. These SAT decreases are most prominent in the high-latitude winter because LW radiation is the primary energy source to the surface and the contribution from ice clouds is large. In contrast, the SAT decrease is minimal in the tropics and mid-latitude regions. In these regions, shortwave (SW) radiation, in addition to LW radiation, has strong influences on the SAT. Also, the abundant water vapor has strong absorption and emission in the LW regime, making the changes in ice cloud LW properties be slightly felt by the surface, resulting in minimal changes of the SAT. The combined effect of emissivity and ice cloud treatments largely resembles those with ice cloud treatments alone (Fig 5.1e and f), indicating that the impacts of ice cloud treatments outweigh the impacts of surface emissivity treatment.

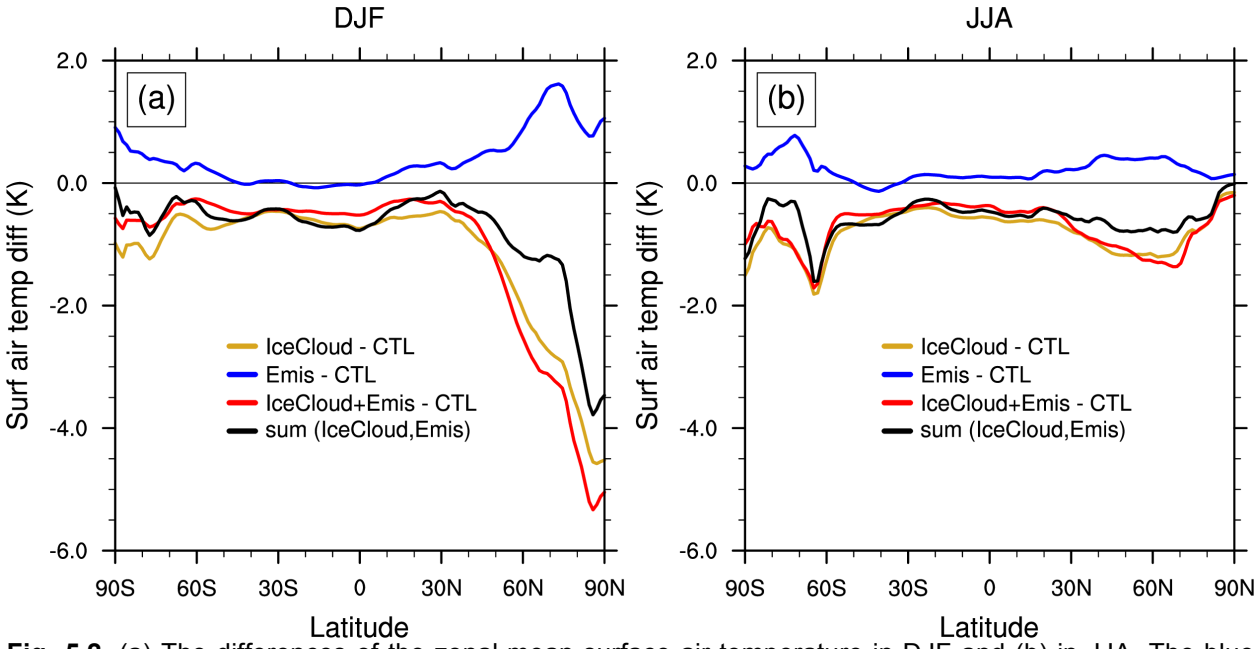

Fig. 5.2. (a) The differences of the zonal-mean surface air temperature in DJF and (b) in JJA. The blue line denotes the difference between the Emis and CTL runs. The gold line denotes the difference between the IceCloud and CTL runs. The red line denotes the difference between the Emis+IceCloud and CTL runs. The black line indicates the sum of the emissivity and ice cloud effects, i.e. the sum of the values from the red and blue lines.

The regional and seasonal dependences of the SAT changes induced by the surface emissivity and ice cloud treatments become clearer when we look at the zonal-mean SAT difference, as shown in Fig. 5.2. The inclusion of surface emissivity increases the DJF zonal-mean SAT in the Arctic by 1-1.5 K, while in the JJA, the SAT changes is no more than 0.5K. In the Antarctic, the SAT increase is about 0.5-1 K with little seasonal dependence. This is because the majority of the Antarctic is cold and dry over the course of the year, the impacts of surface emissivity hence shows little seasonal dependences. Over the tropics and mid-latitudes, the SAT differences due to the inclusion of surface emissivity are much smaller, less than 0.2 K. The impacts of the ice cloud treatments decrease the zonal-mean SAT in the entire globe. This decrease is approximately uniform over the tropics and mid-latitudes by about 0.5 K with little seasonal variation. The SAT decrease is largest in the high-latitude wintertime by about

1-2 K in the Antarctic and by about 2-4 K in the Arctic. In the summertime, this decrease of SAT slightly reduces to approximately 1K in the Antarctic, but the decrease of the SAT largely reduces to 0.5 K in the Arctic. This is because in the Arctic summertime, the atmosphere becomes moist, reducing the contribution from the ice clouds to the downward LW flux at the surface as well as to the influence on SAT. In the Arctic wintertime and the Antarctic throughout the year, both the atmosphere and ice clouds contribute to the surface downward LW flux. Thus, the changes in ice cloud LW optics have large impacts on the SAT. The combined effect of surface emissivity and ice cloud treatment largely resemble those with ice cloud treatment alone, and to some extent, can be linearly added of the individual effect except for Arctic DJF.

To understand whether the inclusions of surface emissivity and ice cloud treatments improve or worsen the simulated SAT compared to the observation, Figure 5.3 shows the SAT difference with respect to the ERA-Interim (Dee et al. 2011). The CTL run, compared to the ERA-Interim, has large warm biases of SAT in the high-latitude regions (Fig. 5.3a). These biases are as large as 8 K in the Arctic DJF, 4-5 K in the Antarctic continent in DJF, and 4-6 K over the Southern Ocean in JJA. The ensemble mean of the E3SM historical runs also shows a large warm SAT bias in the Arctic DJF, partly due to the tuning choices in the Bergeron process (Wuyin Lin, personal communication). Since the inclusion of surface emissivity, compared to the CTL run, increases the SAT in the Arctic DJF (Fig 5.1), this further enhances these SAT warm biases by about 1 K (Fig. 5.3c). The inclusion of ice cloud treatments, on the other hand, largely reduces the SAT warm biases in the Arctic DJF from 6-8K to 2-4K, as the MC6 has smaller ice cloud extinction coefficients than those the standard E3SM uses.

The combined effect of surface emissivity and ice cloud treatments is similar to those with the ice cloud treatments alone.

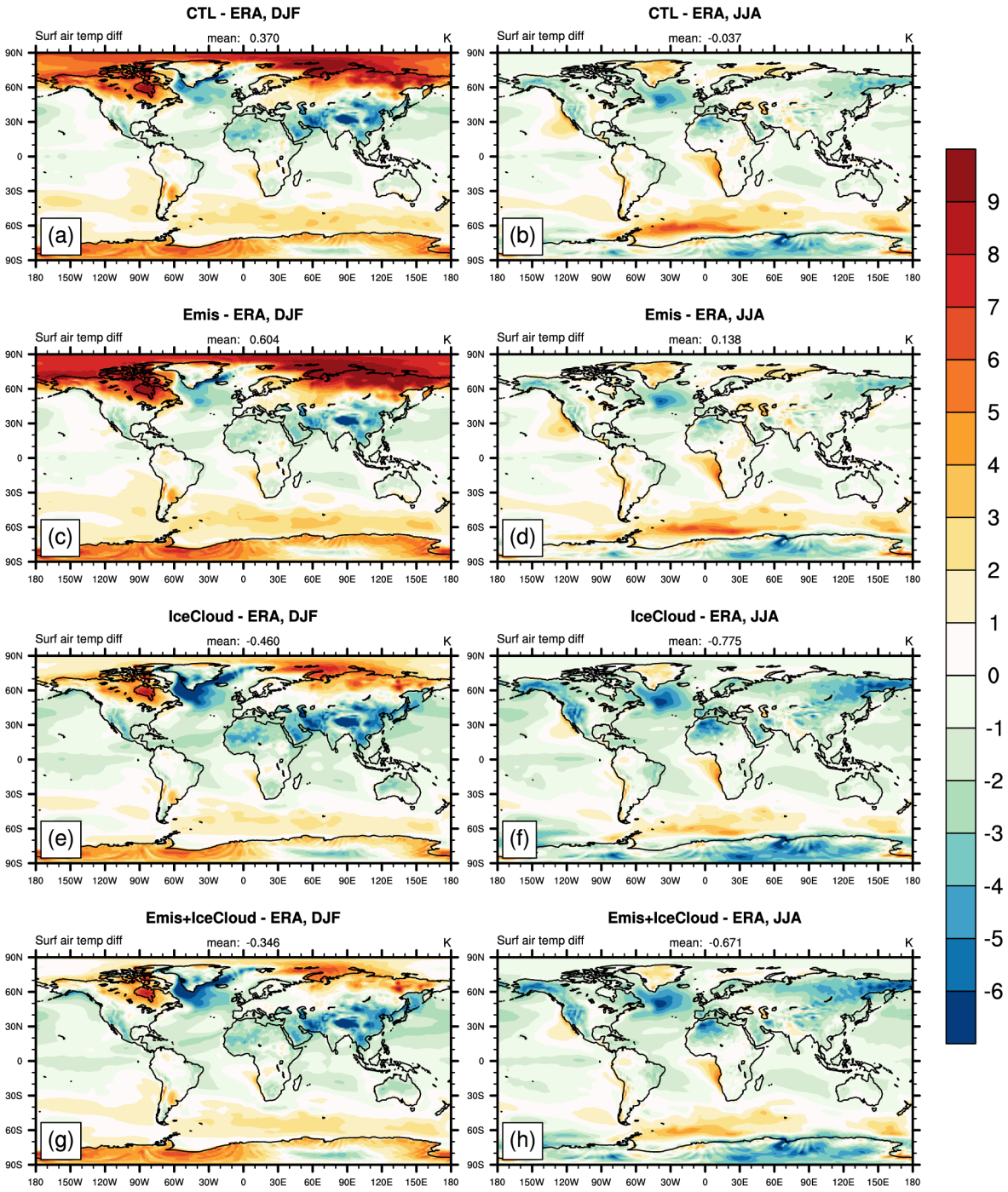

Fig. 5.3. The differences of surface air temperature with respect to the ERA-Interim in DJF (left column) and JJA (right column). (a,b) The differences between the CTL run and ERA-Interim. (c,d) The difference between the Emis run and ERA-Interim. (e,f) The differences between the IceCloud run and ERA-Interim. (g,h) The differences between the Emis+IceCloud run and ERA-Interim.

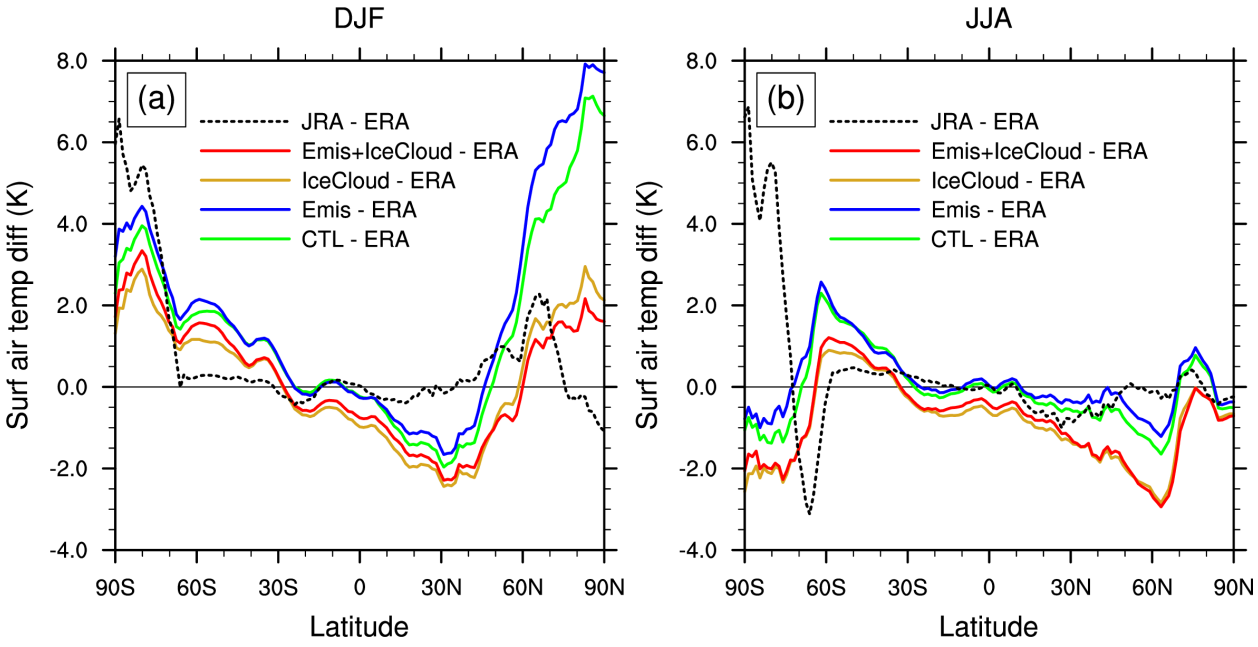

Fig. 5.4. Differences of the zonal-mean surface air temperature with respect to the ERA-Interim in (a) DJF and (b) JJA. The green line denotes the difference between the CTL run and ERA-Interim. The blue line denotes the difference between the Emis run and ERA-Interim. The gold line denotes the difference between the IceCloud run and ERA-Interim. The red line denotes the difference between the Emis+IceCloud run and ERA-Interim. The black dash line denotes the difference between the JRA25 and ERA-Interim.

The SAT differences with respect to the ERA-Interim become clearer when we look at the zonal-mean SAT difference, as shown in Fig. 5.4. We also plot the differences between the ERA-Interim and the JRA-25 (Japanese 25-year ReAnalysis; Onogi et al. 2007) to roughly show the agreement between two different reanalysis datasets. In the Arctic, the JRA-25 agrees well with the ERA-Interim, except an approximately 2 K disagreement at around 65^{o}N in DJF. The CTL run, compared to the ERA-Interim, has warm SAT biases in the Arctic DJF by 4-7 K. These warm biases are reduced to about 2K when the new ice cloud treatments are included. The new ice cloud treatments also decrease the SAT uniformly over the tropics and mid-latitudes, but the magnitude is only around 0.5-1 K with little seasonal dependence. In the Antarctic, a large disagreement by about 6 K between the JRA-25 and the ERA-Interim

is seen, indicating low confidence of the SAT over the Antarctic from reanalysis data (Bracegirdle and Marshall 2012). Consequently, it is hard to conclude whether the inclusion of surface emissivity or the new ice cloud treatments address the SAT biases in the Antarctic or not.

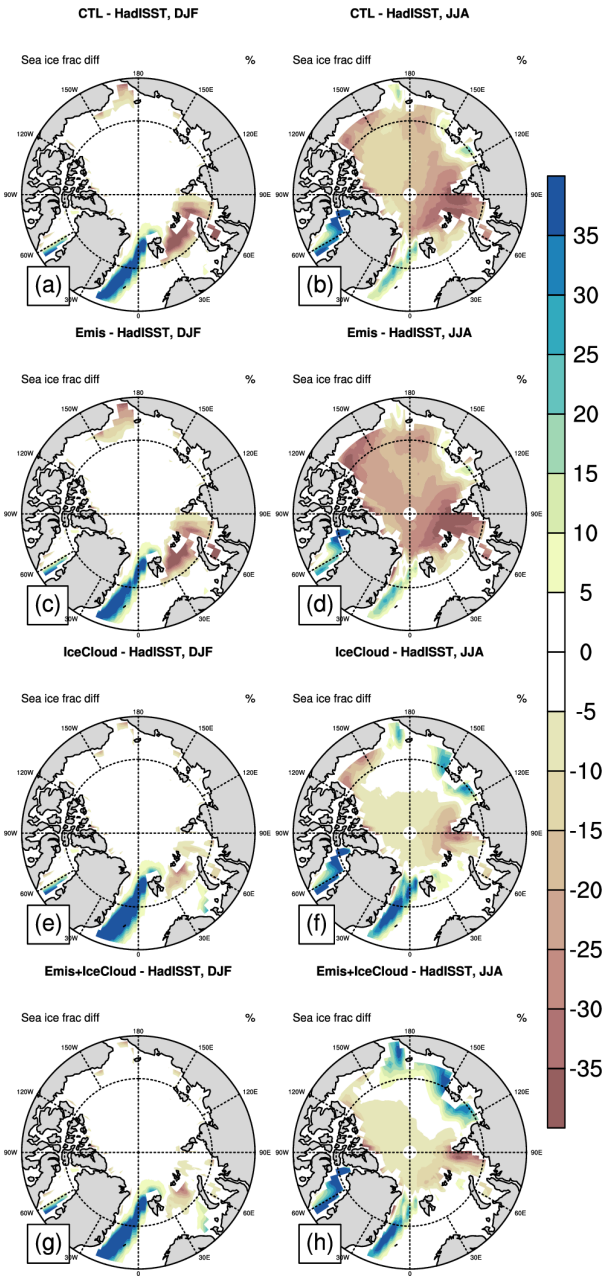

Fig. 5.5. The differences of sea ice fraction with respect to the HadISST in DJF (left column) and JJA (right column). (a,b) The differences between the CTL run and HadISST. (c,d) The difference between the Emis run and HadISST. (e,f) The differences between the IceCloud run and HadISST. (g,h) The differences between the Emis+IceCloud run and HadISST.

Since the inclusion of the new ice cloud treatments reduces the large warm SAT biases in the Arctic, we examine how these SAT changes affect the simulated Arctic sea ice fraction. Figure 5.5 shows the differences in Arctic sea ice fraction between the HadISST (Hadley Center Global Sea Ice and Sea Surface Temperature; Rayner et al. 2013) and all simulation results. Although the CTL has a large warm SAT bias in the Arctic DJF, the sea ice fraction is almost unbiased compared to the HadISST except near the northern Europe (Fig. 5.5a). This is because even though the CTL run has a large warm SAT bias in Arctic DJF, it is still cold enough to maintain the sea ice in DJF over the Arctic Ocean. The inclusion of the ice cloud treatments reduces the negative sea ice biases over the northern Europe by 20-30%. In JJA, the CTL run has a negative bias in sea ice fraction by around 10-30% over the Arctic Ocean and these biases are largely reduced to 5-10% when the new ice cloud treatments are included.

5.3.2 Impacts on other climate variables

This subsection examines the impacts of surface emissivity and the new ice cloud treatments on other climate variables. We first examine the changes in tropospheric temperature fields. Figure 5.6 shows the temperature differences as a function of latitude and pressure level. The inclusion of surface spectral emissivity leads to an increase of temperature in the low troposphere, (Fig. 5.6a and d), in particular during polar winter, consistent with the results shown in Chapter 4. The new ice cloud treatments lead to a decrease in temperature virtually in the entire troposphere (Fig. 5.6b and e). These decreases are prominent in polar winter and the upper troposphere over the tropics, in which ice clouds are frequent over the course of the year. These

decreases in temperature are mainly because the MC6 scheme has smaller ice cloud LW extinction coefficients compared to the counterpart in the E3SM, and thus smaller ice cloud greenhouse effect. The combined effect of emissivity and ice cloud treatments is similar to those with ice cloud treatments alone (Fig 5.6c and f). These results show that inclusions of surface emissivity and ice cloud treatments not only affect the SAT, but also for the tropospheric temperature. Consistent with the changes of the SAT, the changes in tropospheric temperature have strong regional and seasonal dependences.

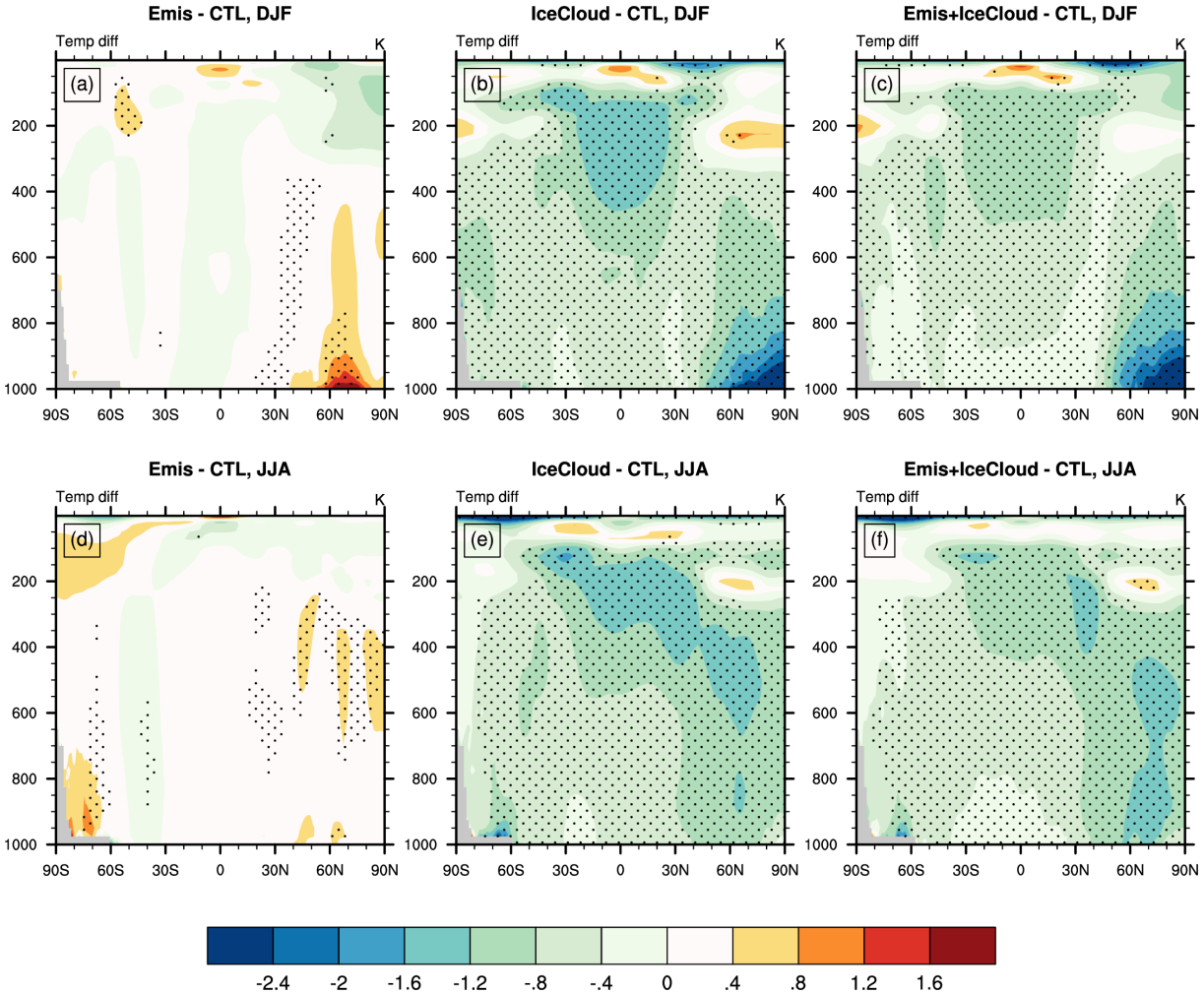

Fig. 5.6. Latitude-pressure cross section of temperature differences with respect to the CTL run in DJF (upper row) and JJA (lower row). (a,d) The difference between the Emis and CTL runs. (b,e) The difference between the IceCloud and CTL runs. (c,f) The difference between the Emis+IceCloud and CTL runs. Dotted area indicates that the differences pass the Student's *t* test with a 5% significance level.

The changes in SAT and tropospheric temperature can influence the OLR. Figure 5.7 and 5.8 show the changes in clear-sky OLR and all-sky OLR, respectively. When the surface emissivity is included, clear-sky OLR increases over the high-latitude land area in the northern hemisphere in DJF (Fig. 5.7a), consistent with the increases in SAT (Fig 5.1). In the Sahara and Sahel, although the SAT increases, the clear-sky OLR decreases by several Wm^{-2}. This is because over the Sahara and Sahel, the surface emissivity can be as low as 0.7 in the atmospheric window band. Although the Emis run has a higher SAT than the CTL run (Fig. 5.1), the surface emission in the window band is still smaller than that of CTL due to the smaller emissivity. This reduction in surface emission in the window band directly reduces the clear-sky and all-sky OLR (Fig 5.7 and 5.8), owing to the weak atmospheric absorption over this band and infrequent clouds over the Sahara and Sahel. The IceCloud run, compared to the CTL, decreases the SAT and tropospheric temperature, resulting in decreases in clear-sky OLR over the entire globe, especially in the Arctic DJF, in which the clear-sky OLR is decreased by around 10 Wm^{-2}. Compared to the CTL run, the annual-mean, global-averaged of clear-sky OLR decreases by 2.59 Wm^{-2} in the IceCloud run and by 3.34 Wm^{-2} in the Emis+IceCloud run. However, the all-sky OLR shows much smaller changes than the clear-sky OLR. In the Arctic DJF, the differences between the IceCloud and CTL runs are less than 2 Wm^{-2} (Fig. 5.8c). The annually and globally averaged all-sky OLR, compared to the CTL run, only decreases by 0.22 Wm^{-2} in the IceCloud run and by 0.42 Wm^{-2} in the Emis+IceCloud run.

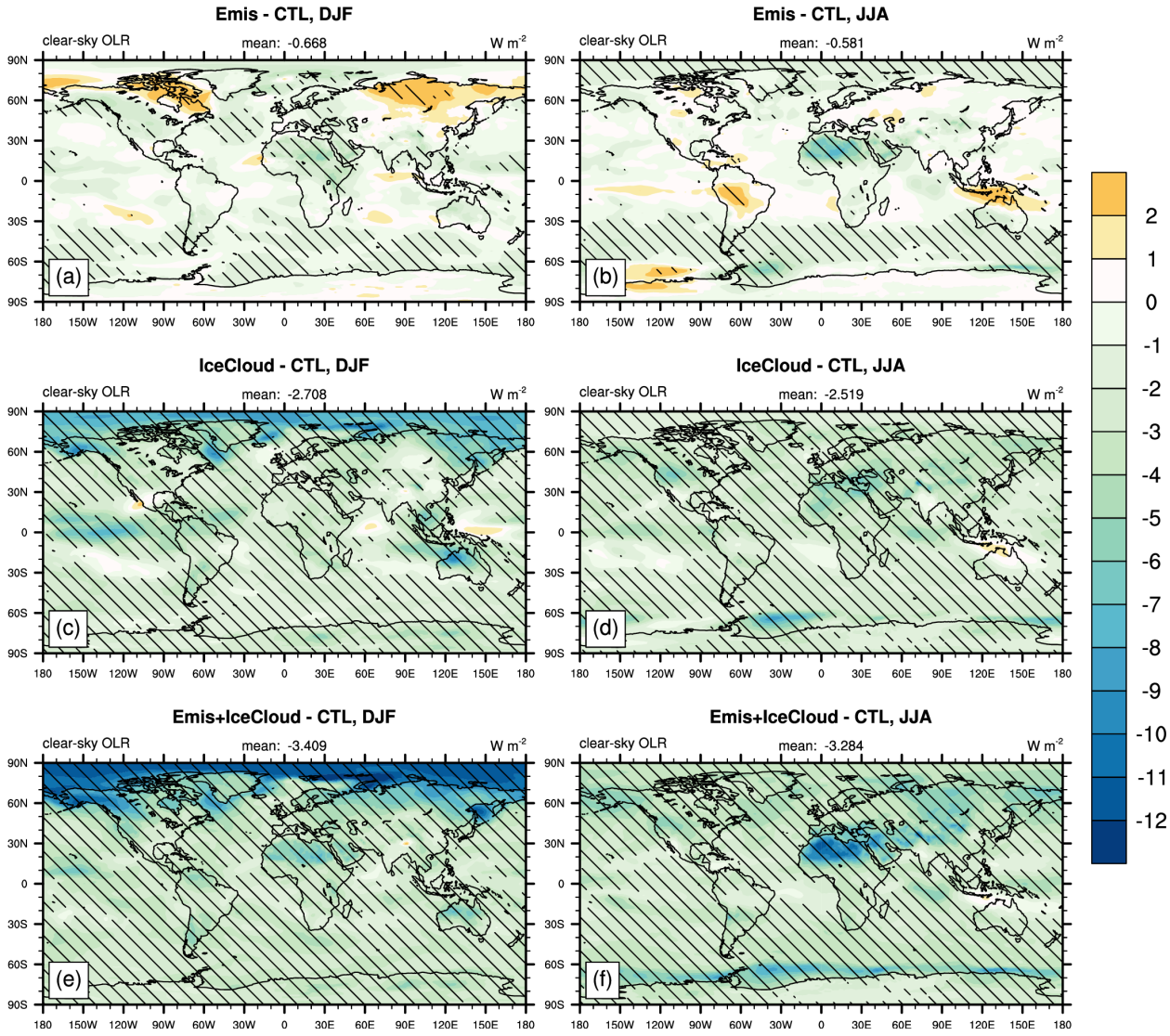

Fig. 5.7. Same as Fig. 5.1 but for clear-sky outgoing LW radiation.

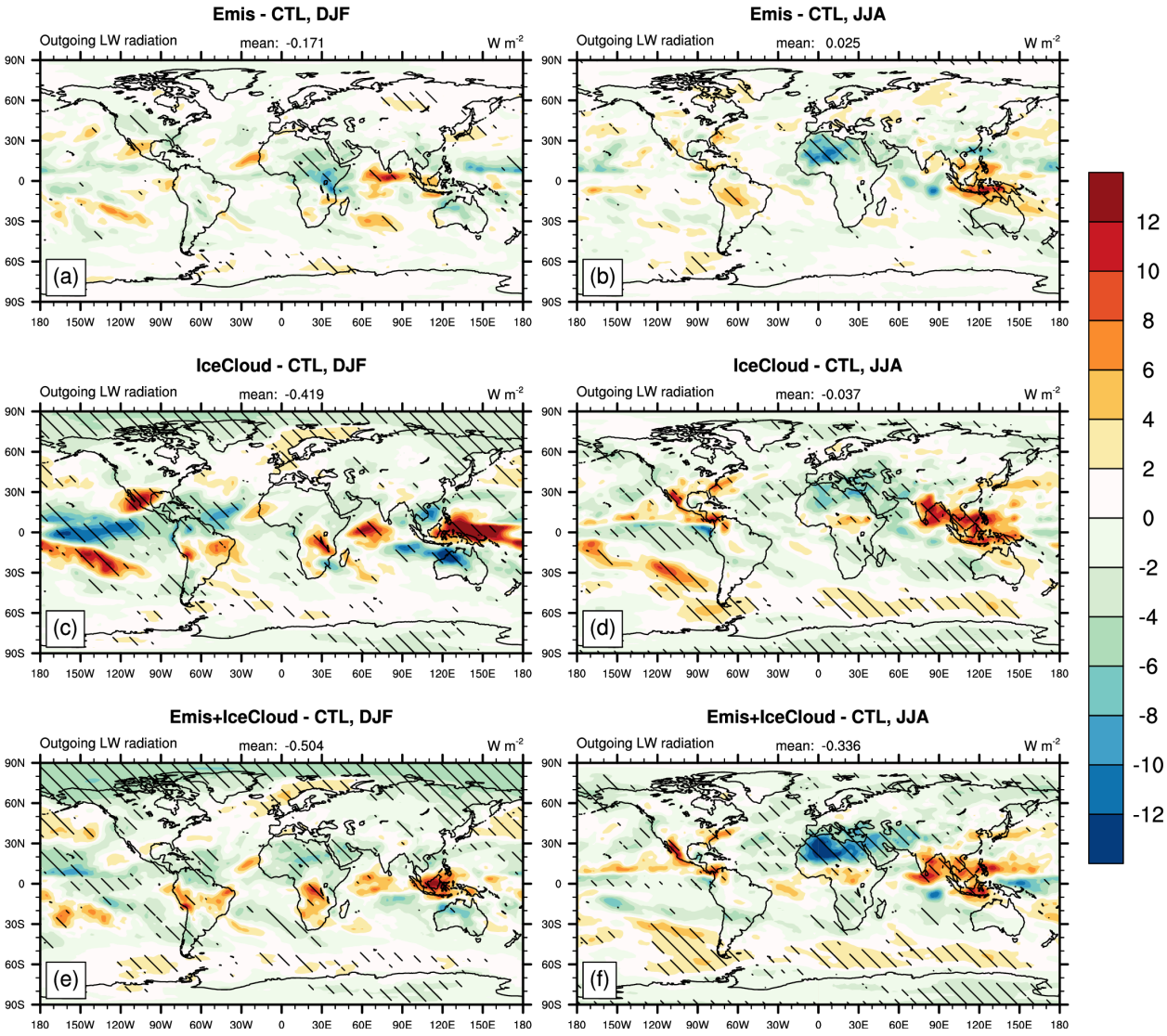

Fig. 5.8. Same as Fig. 5.1 but for all-sky outgoing LW radiation.

Similar to the changes in the all-sky OLR, the changes in net downward SW flux at the TOA (FSNTOA) are small when surface emissivity and ice cloud treatments are included, and many changes are not statically significant (Fig. 5.9). Compared to the CTL run, the changes of annual- and global-mean FSNTOA are 0.06 Wm^{-2} for the Emis run, -1.25 Wm^{-2} for the IceCloud run, and -1.22 Wm^{-2} for the Emis+IceCloud run, respectively. The small changes in the SW and LW fluxes at the TOA suggest that the mean climate does not drift when the surface emissivity and new ice cloud treatments

are included. This also suggests that the E3SM can keep the current setting of the tunable parameters to reach energy equilibrium when the surface emissivity and the new ice cloud treatments are included.

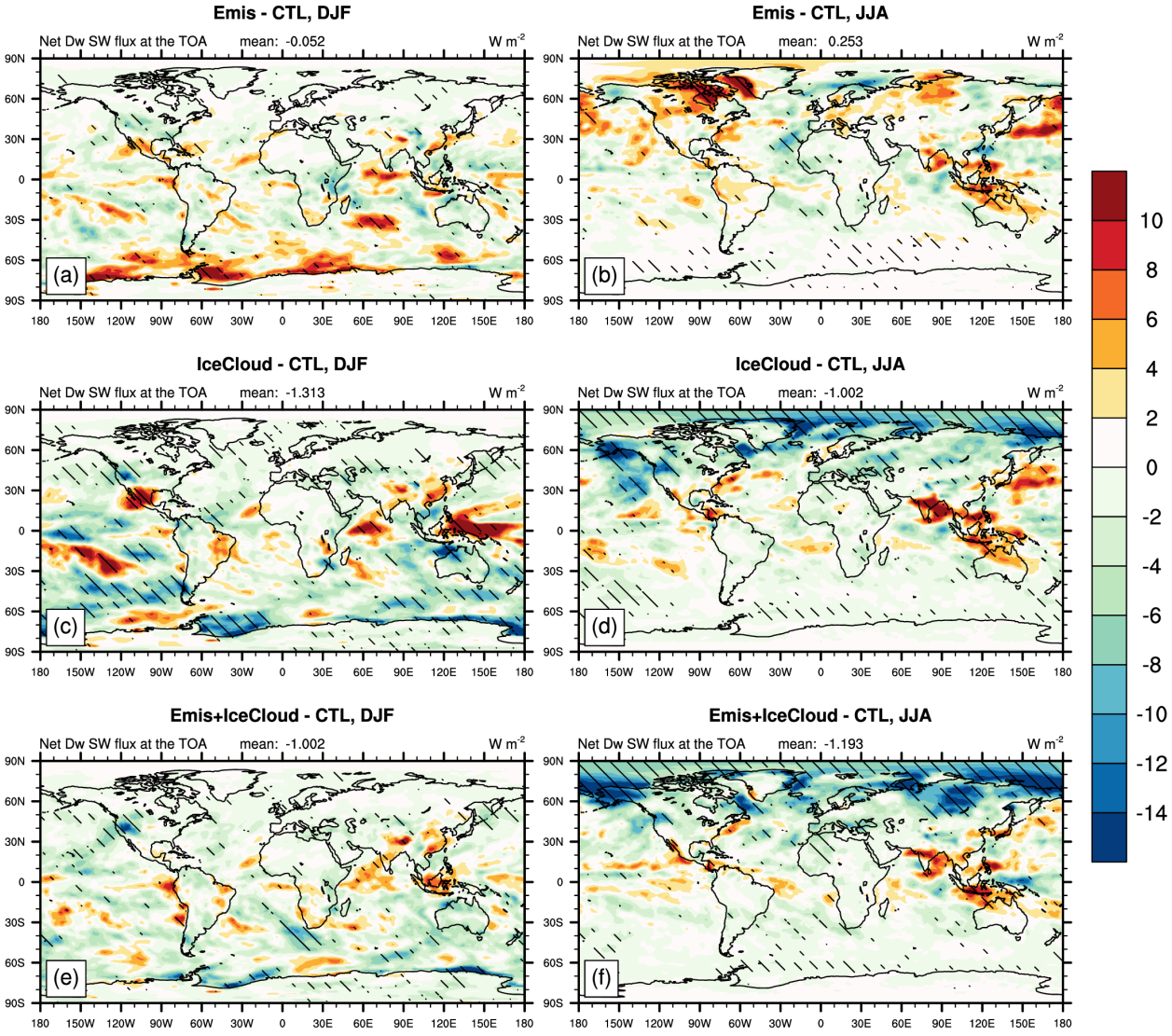

Fig. 5.9. Same as Fig. 5.1 but for net downward SW flux at the TOA.

Lastly, we examine the changes of total precipitation, as shown in Fig. 5.10. Although the inclusions of surface emissivity and ice cloud treatments induce some regional changes in total precipitation, many of these changes are not statistically

significant. The global-averaged change of total precipitation rate is less than 0.03 mm/day. This reveals that the inclusions of surface emissivity and ice cloud treatments have minimal impacts on precipitation.

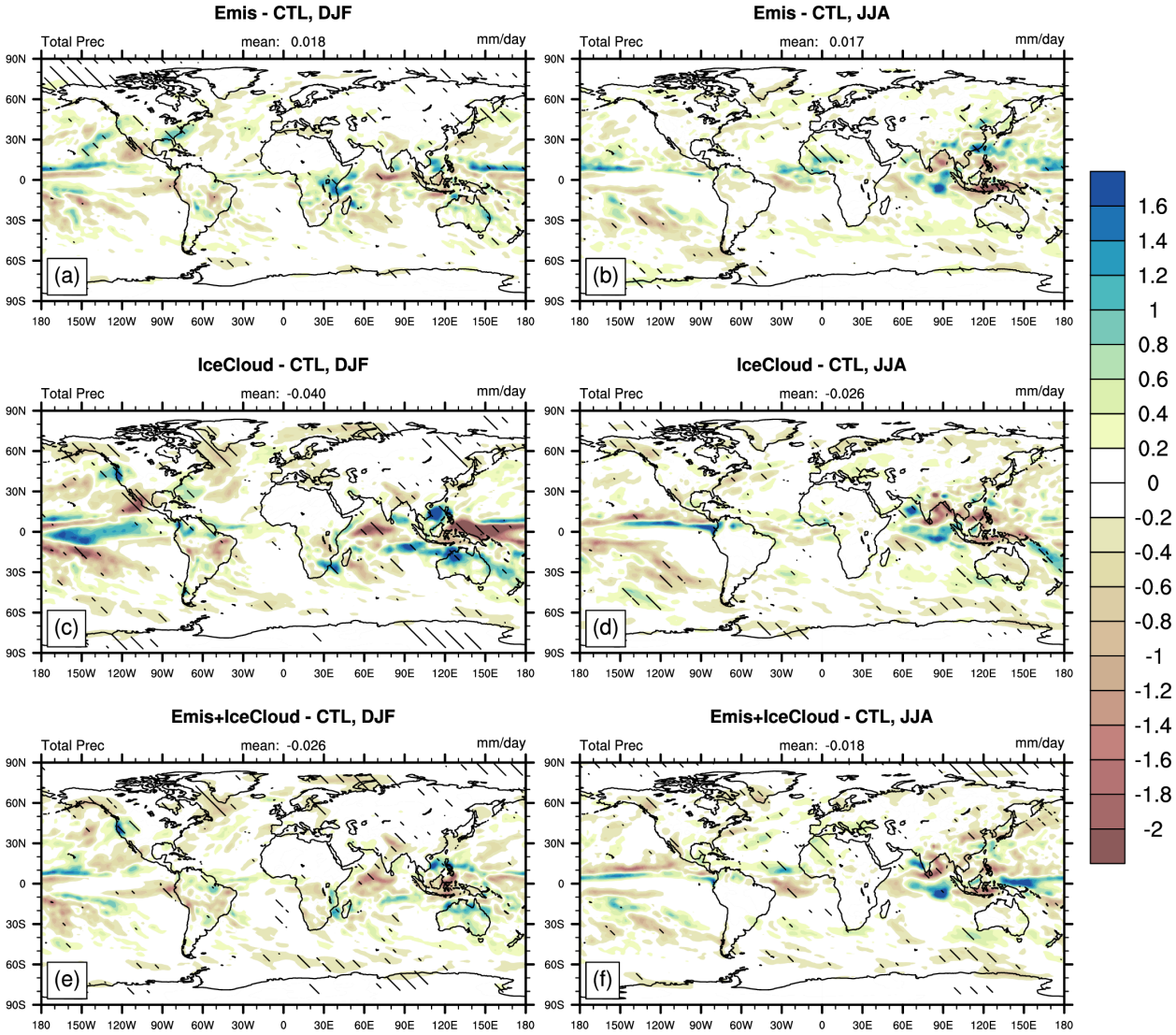

Fig. 5.10. Same as Fig. 5.1 but for total precipitation rate.

5.4 Conclusion

In order to better predict the climate trends relevant to the energy sector and to advance the understanding of the Earth's climate system, the U.S. DOE has funded the E3SM project. The E3SM particularly aims to address issues related to Water cycle and Cryosphere, both of which are strongly connected to the high-latitude regions. In the high-latitudes, LW radiation processes play an important role, but the E3SM, among other Earth system models, still assume the surface as blackbody or graybody and non-scattering clouds in its LW radiation schemes. These assumptions can be questionable in the high-latitudes, as demonstrated in Chapters 3 and 4 as well as recent studies. This suggests a need to implement realistic surface spectral emissivity and cloud LW scattering into the E3SM, and examines the impacts on the simulated climate, which are the foci of this chapter.

Compared to the standard E3SM historically fully-coupled simulations, the inclusion of surface spectral emissivity leads to an increase in the SAT in the high-latitude regions, especially during the winter. These results are consistent with those using CESM with a slab-ocean model (Chapter 4), indicating the robustness of the surface emissivity effects on the high-latitude regions. The inclusion of the new ice cloud treatments, namely, a two/four-stream LW radiation solver that can handle LW scattering calculation and the MC6 ice cloud LW optical scheme, decreases the SAT in the high-latitude regions compared to the standard E3SM, mainly because the MC6 has smaller extinction coefficients than the default ice cloud LW radiation scheme in the standard E3SM, and thus smaller ice cloud greenhouse effect. Compared with the observed SAT in the Arctic DJF, the inclusion of the new ice cloud treatments largely

reduces the prominent warm SAT biases in the standard E3SM from 6-8 K to 2-4 K with minimal impacts on other regions such as the tropics and mid-latitudes. This result highlights the importance of ice cloud LW optical schemes in the high-latitudes.

References

Bader, D., Collins, W., Jacob, R., Jones, P., Rasch, P., Taylor, M., et al. (2014). Accelerated Climate Modeling for Energy. U. S. Department of Energy. Retrieved from https://climatemodeling.science.energy.gov/sites/default/files/publications/acme-project-strategy-plan.pdf

Bracegirdle, T. J., and G. J. Marshall, 2012: The reliability of antarctic tropospheric pressure and temperature in the latest global reanalyses. J. Clim., 25, 7138–7146, doi:10.1175/JCLI-D-11-00685.1.

Dee, D. P., and Coauthors, 2011: The ERA-Interim reanalysis: configuration and performance of the data assimilation system. Q. J. R. Meteorol. Soc., 137, 553–597, doi:10.1002/qj.828.

Eyring, V., S. Bony, G. A. Meehl, C. A. Senior, B. Stevens, R. J. Stouffer, and K. E. Taylor, 2016: Overview of the Coupled Model Intercomparison Project Phase 6 (CMIP6) experimental design and organization. Geosci. Model Dev., 9, 1937–1958, doi:10.5194/gmd-9-1937-2016.

Feldman, D. R., W. D. Collins, R. Pincus, X. L. Huang, and X. Chen, 2014: Far-infrared surface emissivity and climate. Proc. Natl. Acad. Sci. U. S. A., 111, 16297–16302, doi:10.1073/pnas.1413640111.

Golaz, J. C., and Coauthors, 2019: The DOE E3SM Coupled Model Version 1: Overview and Evaluation at Standard Resolution. J. Adv. Model. Earth Syst., doi:10.1029/2018MS001603.

Huang, X. L., X. H. Chen, D. K. Zhou, and X. Liu, 2016: An Observationally Based Global Band-by-Band Surface Emissivity Dataset for Climate and Weather Simulations. J. Atmos. Sci., 73, 3541–3555, doi:10.1175/JAS-D-15-0355.1.

Huang, X. L., X. H. Chen, M. Flanner, P. Yang, D. R. Feldman, and C. Kuo, 2018: Improved Representation of Surface Spectral Emissivity in a Global Climate Model and Its Impact on Simulated Climate. J. Clim., 31, 3711–3727, doi:10.1175/JCLI-D-17-0125.1.

Hurrell, J. W., and Coauthors, 2013: The Community Earth System Model: A Framework for Collaborative Research. Bull. Am. Meteorol. Soc., 94, 1339–1360, doi:10.1175/BAMS-D-12-00121.1.

Kuo, C.-P., P. Yang, X. Huang, Y.-H. Chen, and G. Liu, 2020: Assessing the accuracy and efficiency of longwave radiative transfer models involving scattering effect with cloud optical property parameterizations. J. Quant. Spectrosc. Radiat. Transf., 240, 106683, doi:10.1016/j.jqsrt.2019.106683.

Li, H., M. S. Wigmosta, H. Wu, M. Huang, Y. Ke, A. M. Coleman, and L. R. Leung, 2013: A physically based runoff routing model for land surface and earth system models. J. Hydrometeorol., 14, 808–828, doi:10.1175/JHM-D-12-015.1.

Li, H. Y., L. R. Leung, A. Getirana, M. Huang, H. Wu, Y. Xu, J. Guo, and N. Voisin, 2015: Evaluating global streamflow simulations by a physically based routing model coupled with the community land model. J. Hydrometeorol., 16, 948–971, doi:10.1175/JHM-D-14-0079.1.

Oleson, K. W., and Coauthors, 2013: Technical description of version 4.5 of the Community Land Model (CLM) (Tech. Rep. NCAR/TN-503+STR). Boulder, Colorado, USA: National Center for Atmospheric Research

Onogi, K., and Coauthors, 2007: The JRA-25 reanalysis. J. Meteorol. Soc. Japan, 85, 369–432, doi:10.2151/jmsj.85.369.

Neale, R. B., Gettelman, A., Park, S., Conley, A. J., Kinnison, D., Marsh, D., et al. (2012). Description of the NCAR Community Atmosphere Model (CAM 5.0), tech. Note NCAR/TN-486+STR, Natl. Cent. For Atmos (pp. 2009–038451).

Petersen, M. R., and Coauthors, 2019: An Evaluation of the Ocean and Sea Ice Climate of E3SM Using MPAS and Interannual CORE-II Forcing. J. Adv. Model. Earth Syst., doi:10.1029/2018MS001373.

Rasch, P. J., and Coauthors, 2019: An Overview of the Atmospheric Component of the Energy Exascale Earth System Model. J. Adv. Model. Earth Syst., 11, 2377–2411, doi:10.1029/2019ms001629.

Ringler, T. D., J. Thuburn, J. B. Klemp, and W. C. Skamarock, 2010: A unified approach to energy conservation and potential vorticity dynamics for arbitrarily-structured C-grids. J. Comput. Phys., 229, 3065–3090, doi:10.1016/j.jcp.2009.12.007.

U.S. Department of Energy (2013). U.S. energy sector vulnerabilities to climate change and extreme weather (Tech. Rep. DOE/PI-0013): U.S. Department of Energy. https://www.energy.gov/sites/prod/files/2013/07/f2/20130710-Energy-Sector-Vulnerabilities-Report.pdf.

Xie, S., and Coauthors, 2018: Understanding Cloud and Convective Characteristics in Version 1 of the E3SM Atmosphere Model. J. Adv. Model. Earth Syst., 10, 2618–2644, doi:10.1029/2018MS001350.

Chapter 6

Conclusion

6.1 Overview

Longwave (LW) radiation plays a critical role in the Earth's climate system. It carries out energy from the earth-atmosphere system to space, thereby balancing the net incoming solar radiation at the top of the atmosphere over the entire globe at a sufficient long-term average. It also redistributes energy within the atmosphere and between the atmosphere and the surface. Due to its importance, a correct and faithful representation of the LW radiative processes in climate models is crucial for understanding the Earth's climate system and projecting future climate. Because climate model simulations are computationally expensive, approximations have to be made in the LW radiation calculations in order to make the simulations affordable and practical. Two such common approximations are blackbody surface and non-scattering clouds. This dissertation, along with other recent studies, demonstrates the impact of surface spectral emissivity and ice cloud LW scattering on the simulated climate, echoing the needs to re-examine these approximations, improve current treatments, and conduct more studies afterward. Major findings from each chapter are summarized in Section 6.1 and then future work directions are elaborated in Section 6.2.

6.2 Chapter summaries

Chapter 2 quantifies the impact of the inclusion of realistic surface spectral emissivity in the Sahara and Sahel on the simulated local climate and beyond. The surface emissivity in these regions can be as low as 0.6–0.7 over the infrared window band while close to unity in other spectral bands, but such spectral dependence has been ignored in current climate models. To investigate this issue, realistic surface spectral emissivity over the Sahara and Sahel is incorporated into the Community Earth System Model (CESM), while the treatments of the rest of the globe remain unchanged (i.e. blackbody surface). Both the modified and standard CESM are then used to carry out 35-year simulations and the outputs from the last 30 years are analyzed. Compared to the standard CESM with blackbody surface approximation, the modified CESM has warmer surface air temperature, and a warmer and wetter planetary boundary layer over the Sahara and Sahel. The modified CESM thus favors more convection in these regions and has more convective rainfall, especially in the Sahara. The moisture convergence induced by such inclusion of surface spectral emissivity also contributes to the differences in simulated precipitation in the Sahel and the region south to it. This chapter also shows that if a climate model does not take the spectral surface emissivity into account over desert area, it will have a different band-by-band partition for the surface upward LW flux as well as the OLR, with excessive flux from the window band.

Chapter 3 investigates the ice cloud LW scattering effect on the polar climate. A dominant majority of climate models, as of today, still assume non-scattering clouds in their LW radiation scheme. The traditional rationale is that, compared to strong LW absorptions by cloud and greenhouse gases, cloud LW scattering is negligible. This

traditional rationale is supported by offline radiative transfer calculations and also by climate simulations with prescribed sea surface temperatures (SSTs) and sea ice. However, this rationale is not valid for simulated polar climate. The polar regions have much less water vapor than the extra-polar regions, implying that cloud LW scattering is non-negligible anymore. The cloud LW scattering can increase the downward LW radiation at the surface, leading to an increase of surface temperature and, consequently, further warms and moistens the atmosphere. The aforementioned responses clearly exhibit in the Arctic using the CESM simulations with a slab-ocean model, in which the SSTs are allowed to change. The scattering effect increases the Arctic winter surface air temperature by 0.8-1.8K. However, the scattering effect becomes much weaker when the SSTs and sea ice are prescribed, in which the surface temperature only increases around 0.1 K in the Arctic winter. Similar contrasts between the slab-ocean and prescribed-SST runs are also seen in the Antarctic, though the contrasts are smaller than those in the Arctic, mainly because the majority of the Antarctic is covered by land, in which the surface is coupled with the atmosphere in both the slab-ocean and prescribed-SST simulations. We also show that the scattering effect of the far-IR band largely contributes to the total scattering effect in the polar regions. This chapter demonstrates the importance of cloud LW scattering in the polar regions and highlights these scattering effects are notable only when the surface is coupled with the atmosphere.

Chapter 4 quantifies the combined effect of surface emissivity and ice cloud LW scattering on the high-latitude regions and the relative contribution of each effect. Previous studies have reported that these two effects can increase the surface air

temperature in the high-latitude regions, but the combined effect and the relative contributions from each have not been quantified. When the surface is not blackbody and clouds can scatter LW radiation, multiple reflection of LW radiation between the surface and clouds can occur and retain more energy in the Earth system than the case of blackbody surface and non-scattering clouds. Using CESM simulations, we show that, in the high-latitude regions, the combined effect induces further warming at the surface than the individual effect does, and this combined effect is roughly the sum of the individual effects, indicating that the surface emissivity and cloud scattering effects to a large extent are linearly additive. We also examine the changes of sea ice fraction, low cloud, and shortwave fluxes at the Southern Ocean in response to these effects. We have found that these effects increase the surface temperature and reduces the sea ice fraction, especially near the edge of sea ice extent in the Southern Ocean. The reduction in sea ice exposes the ocean underneath, providing more water vapor to the atmosphere and leads to increases in low cloud fraction. The increases in low cloud fraction block shortwave radiation and reduce the downward shortwave flux at the surface. The net downward shortwave flux, however, increases at the surface due to the reduction in sea ice coverage, which means the shorwave energy absorbed by the surface is increased when the surface emissivity and cloud scattering effects are included.

Chapter 5 describes the implementations of surface spectral emissivity and a set of new ice cloud LW treatments into the Exascale Earth System Model (E3SM). The implementation of ice cloud treatments includes a two/four-stream LW radiation solver, the MC6 ice cloud LW optical scheme, and enabling the ice cloud LW scattering effect.

These implementations are similar to what we have done for the CESM, which has been described in Chapters 2-4. The impacts of these implementations are examined using E3SM fully-coupled simulations. The surface emissivity effects largely resemble those in the CESM, indicating the robustness of the surface emissivity effects. The implementation of the new ice cloud treatments decreases the surface air temperature in the high-latitude regions compared to the standard E3SM, mainly because the MC6 ice cloud LW optical scheme has smaller extinction coefficients than the counterpart of the standard E3SM, and thus smaller ice cloud greenhouse effect. The combined effect of the surface emissivity and the new ice cloud treatments largely resembles those with the ice cloud treatments alone, indicating that the impact of ice cloud treatments outweighs the impact of surface emissivity treatment. Compared with the observation, the implementation of the new ice cloud treatments considerably reduces the prominent warm surface air temperature biases in the Arctic winter of the standard E3SM from 6-8 K to 2-4 K. The changes of surface air temperature are minimal in other regions such as the tropics and mid-latitudes, largely owing to the large amount of water vapor in these regions, in which the role of ice clouds in LW radiation is small. This result highlights the importance of ice cloud LW optical schemes in the polar climate simulations.

6.3 Future work

This dissertation addresses a few questions related to surface spectral emissivity and cloud LW scattering in the climate simulations. Many further questions remain unanswered and worth addressing. The modified version of the CESM and E3SM developed in this dissertation provide ideal tools for addressing these questions. Here I list some topics that, in my opinion, are worth pursuing. By pursuing these questions,

we can have a better understanding of the LW radiation processes in the atmosphere and of the LW radiative coupling between the surface and the atmosphere, advancing our knowledge of the Earth's climate system.

6.3.1 Future research questions related to surface emissivity

Most climate models assume constant graybody emissivity in the surface models (i.e., land, ocean, and sea ice) while assuming blackbody in the atmospheric model, which can cause spectral inconsistency across different model components. In this dissertation and other studies, surface spectral emissivity is implemented into the LW radiation scheme of the atmospheric model, instead of the surface models. This does not resolve the spectral inconsistency across model components. I suggest that the surface models should be implemented the surface spectral emissivity, same as those in the atmospheric model. In this way, the LW radiative coupling between the atmosphere and the surface becomes more consistent and more realistic.

When surface models include surface spectral emissivity, this can open up new research themes. For instance, because surface emissivity depends on surface type, the changes in surface type due to land use or due to the increases of greenhouse gases can change the surface emissivity. How do these changes in surface emissivity affect the atmospheric characteristics, which in turn affect the processes that caused the surface type changes? Answering these questions can advance the understanding of the LW radiative coupling between the surface and the atmosphere, and the surface-atmosphere interactions in general.

6.3.2 Future research questions related to cloud LW scattering

This dissertation points out the importance of the cloud LW scattering effects on the polar surface energy budget and surface temperature, and these effects are notable only when the surface is coupled with the atmosphere in climate simulations. These can foster subsequent research on the polar regions. For example, how does the cloud LW scattering influence the characteristics of polar clouds, such as cloud phase, lifetime, and seasonal cycle? How does the scattering influence the local circulations in the polar regions? Furthermore, since the cloud LW scattering effect induces larger warming in the polar regions than in the tropics, this can change the meridional temperature gradient. These changes in the temperature gradient can influence the atmospheric circulation and other atmospheric phenomena, such as Hadley circulation and extrapolar cyclones. Quantifying the impacts of cloud scattering on the large-scale atmospheric circulations would be interesting research topics.

In addition to studying the cloud scattering effects on the global scale and climate features, these effects can also be studied at the regional scale and weather features. The European Centre for Medium-Range Weather Forecasts (ECMWF) plans to implement the cloud LW scattering effects into their weather operation model (Hogan 2018). It would be interesting to see how the cloud scattering effect influences the weather forecast.

6.3.3 Future research questions related to paleoclimate

Climate proxy records show that there were many cold and warm episodes occurring in the history of our planet, such as the cold Snowball Earth that occurred at

least twice during 500-800 million years ago, the warm Early Eocene between 54 and 48 million years ago, and the cold Last Glacial Maximum between 24 and 18 thousands of years ago. Climate models have been used to simulate these paleoclimatic episodes with reconfigurations of the surface conditions, Earth orbital parameters, solar forcing, and other factors (e.g. Poulsen and Jacob 2004; Zhu et al. 2019). In addition to these reconfigurations, a correct representation of physical processes in climate models is necessary to reasonably simulate the past climate and understand the delicate interplay and feedbacks among different physical processes. This dissertation concludes that surface spectral emissivity and cloud LW scattering play important roles in the simulated polar climate, where the atmosphere is cold and dry. This conclusion is also applicable when climate models are used to simulate cold and dry atmospheric conditions, such as those during the Snowball Earth and the Last Glacial Maximum periods. Besides, the desert surface emissivity in the LW window band is considerably different from that of forests and shrub land. This implies that whenever there is a large-scale desertification or reversed event in the geological history, the corresponding changes in surface spectral emissivity could influence the local and regional climate, and possibly the global climate. All these aforementioned considerations strongly warrant the inclusion of surface emissivity and cloud LW scattering into the paleoclimate modeling studies.

References

Hogan, R. J., and A. Bozzo, 2018: A Flexible and Efficient Radiation Scheme for the ECMWF Model. J. Adv. Model. Earth Syst., 10, 1990–2008, doi:10.1029/2018MS001364.

Poulsen, C. J., and R. L. Jacob, 2004: Factors that inhibit snowball Earth simulation. Paleoceanography, 19, n/a-n/a, doi:10.1029/2004PA001056.

Zhu, J., C. J. Poulsen, and J. E. Tierney, 2019: Simulation of Eocene extreme warmth and high climate sensitivity through cloud feedbacks. Sci. Adv., 5, eaax1874, doi:10.1126/sciadv.aax1874.